UNIVERSITÀ DEGLI STUDI DI MILANO

DEPARTMENT OF PHYSICS

PHD SCHOOL IN PHYSICS, ASTROPHYSICS AND APPLIED PHYSICS
CICLE XXXIV

Structure, dynamics and phase transitions of biological matter

Disciplinary Scientific Sector FIS/03

Director of the School: Prof. Matteo PARIS

Supervisor of the Thesis: Prof. Stefano ZAPPERI

PhD Thesis of:
Linda RAVAZZANO

A. Y. 2021-2022

Commission of the final examination:

External Members:
Prof. Giampaolo Mistura
Prof. Paolo Biscari

Internal Member:
Prof. Stefano Zapperi

Final examination:

13 April 2022

Università degli Studi di Milano, Dipartimento di Fisica, Milano, Italy

MIUR subjects:

FIS/03

Contents

List of Figures

List of Tables

Introduction

Motivation

Biological systems astonish us for their variety and richness. They show a degree of complexity that usually overcomes what can be found in systems that have been so far the standard object of classical physics investigation. To have an intuitive idea, let us think to the complexity of bacterial colonies or even of a single eukaryotic cell, with all its molecular mechanisms, with respect to ideal gas particles, confined in a box at a fixed temperature and pressure. Classical physics has been revolutionized by the idea proposed by Ludwig Boltzmann in the 19th century of linking the macroscopic properties of a system composed of several particles with the microscopic configurations of the individual particles. This approach suggests that even in complex biological systems it could be possible to connect emergent behaviours with parameters describing local properties. Furthermore, it has been observed that in many biological systems, physical and even mechanical aspects are of crucial importance. Just to give some examples, let us think of the ability of stem cells differentiating in muscle, bone or other types of cells according to the rigidity (clearly a physical property) of the environment [51]. Let us consider the fact that cancer cells have peculiar physical characteristics, since they are softer than normal ones [73]. Moreover, cells can tune their trajectories and movements (physically their dynamics) as a finding strategy to look for nutrients in the surrounding environment [59]. The awareness of the centrality of physical and mechanical interactions in many biological processes, has opened the way to a multidisciplinary approach in dealing with complex biological issues, such as the study of cancer formation and progression [53]. In this field some interesting attempts of describing tumours with mathematical models that take into account cell properties have been made [26]. A soft-matter physics approach can be attempted for biological systems such as groups of algae, cells confined in narrow channels or protein complexes such as nuclear pores on the nuclear envelope of eukaryotic cells. The main idea underlying this Thesis is to investigate the properties of biological matter, gaining insight on its dynamics and structure and looking for phase transitions. To reach this goal, we will describe complex biological systems with simplified mathematical models, that take into account peculiar properties, such as the ability of living matter to self-sustain its motion, or specific particle interactions. The advantage of such an approach lies in the ability of describing a complex biological system with only few key parameters, such as particle mobility or inter-particle adhesion. Those models could be used to implement computer simulations and to study *in silico* phenomena such as phase transitions, collective migration or spatial organization, as a function of parameters changes. When proposing a model, some approximations and

assumptions should always been made. This is the most difficult and delicate part of this modelling process, that requires carefully taking into account our biological knowledge of the problem. With proper attention, this multidisciplinary approach can deepen our understanding of complex biological systems. On the other side, this approach can expand our knowledge of physics, since it forces us to deal with non equilibrium systems, lacking a complete theoretical description of their dynamics and thermodynamics.

Thesis structure

The present Thesis consists of two Parts, for a total of five Chapters. Part I spans from Chapter 1 to Chapter 3 and deals with different biological systems that can be described using models of interacting active matter, focusing on phase transitions and invasion properties. Part II is composed of Chapters 4 and 5 and addresses the study of nuclear pores spatial distribution on the nuclear membrane, in a soft matter perspective.
Chapter 2 has already appeared as refereed publication in a scientific journal; Chapter 5 has been submitted to a peer reviewed scientific journal and is under revision. Some minor variations have been made in the presentation of previously published results, to maintain consistency of style and content structure throughout the manuscript.

Chapter 1: Active matter systems and phase transitions We set the stage by introducing active matter and its role in describing systems of biological interest. We explain a single particle model widely used to describe active matter: Active Brownian Particles (ABP). Then we deal with phase transitions in active matter, discussing the state of the art and focusing, in particular, on the jammed-unjammed phase transition.

Chapter 2: Unjamming of Active Rotators From a statistical physics point of view, one of the most interesting features of active particles assemblies is the richness of dynamical phases they can undergo when varying internal parameters, such as density, adhesion strength or self-propulsion. Most theoretical studies of active matter consider self-propelled particles driven by active forces. The observation of the motion of *Chlamydomonas reinhardtii* algae, in which the active particles have not only the ability of self-propel, but also to self-rotate, suggests, however, that active torques may also play an important and yet unexplored role. Inspired by this experimental example, we build a model for interacting active matter based on ABPs and we simulate the dynamics of a system of interacting active 2D disks endowed with active torques and self-propulsive forces. This work has been published as an article in *Soft Matter* ([82]), on which the Chapter is based.

Chapter 3: Active matter invasion in narrow channels In this chapter, we apply the single particle model for interacting active matter developed in Chapter 2 to study the invasion properties of bulk of jammed active matter in the vicinity of a narrow open channel. Our aim is to characterize how few parameters such as self-propulsion strength and inter-particle adhesion can influence the way active particles invade. In this case, the rotation of particles is not explicitly imposed by applying an active torque, but it can emerge as a consequence of the particle-particle interaction. This work is currently in preparation for submission to a scientific journal

Chapter 4: Nuclear Pores In this chapter, we introduce nuclear pores, vast protein assemblies inserted in the nuclear envelope of eukaryotic cells that act as main

gates for communication between nucleus and cytoplasm. We specify their structure and functions and describe the state of the art about their spatial distribution on the nuclear envelope.

Chapter 5: Spatial organization of nuclear pores in *Xenopus laevis* oocytes Nuclear pores have been extensively studied to determine their structure and composition, yet their spatial organization and geometric arrangement on the nuclear surface are still poorly understood. Here, we analyse super-resolution images of the surface of *Xenopus laevis* oocyte nuclei during development, and characterize the arrangement of nuclear pores using tools commonly employed to study the atomic structural and topological features of soft matter. To interpret the experimental results, we hypothesize an effective interaction among nuclear pores and implemented it in extensive numerical simulations of octagonal clusters mimicking typical pore shapes. This work has been submitted as an article in *Soft Matter* ([81]), on which the Chapter is based.

Part I
Active Matter

CHAPTER 1

Active matter systems and phase transitions

1.1 Introduction

One of the aims of this thesis is to investigate the dynamics and phase transitions of biological matter, using tools and techniques typical of soft matter matter physics. A particularly interesting question is to determine collective and emergent properties of a system composed by biological units, starting from an appropriate mathematical model of the motion of a single particle. An approach that is reminiscent of an atomistic description. To reach this goal, it is crucial to consider a fundamental characteristics that is common in most biological systems: the ability of the units composing the system of converting biochemical energy into motion. This is an intrinsic characteristics of living systems: cells use nutrients as fuel to sustain their activity and movement, algae perform photosynthesis to obtain the energy necessary to move using their flagella, animals feed themselves and transform food in energy necessary to swim, to fly, to crawl or to walk. This ability of converting stored or ambient energy into systematic movement, is what defines active matter: a system composed of self-driven units. The detailed study of those systems, together with the attempts of theoretically model self-propelled particles, gave rise to active matter as an entire new field in soft matter physics. This field has strong interdisciplinary connection with biology, materials science and engineering for what concerns the experimental part [70]. One of the most commonly used model to describe self-propelled particles was proposed by Vicsek et al. [104], to study swarm behaviour of animals in 1995. In the Vicsek model, particles tend to align with the average direction of motion of their neighbours. That work stimulated a growing interest in the peculiar properties of active matter systems [66],[80], also inspired from the observation of natural phenomena such as the movements of flocks of birds [14], schools of fishes or cell populations [70]. The field was pushed forward by new technological achievements that allowed the production of active colloids [112], Janus particles [105] [45], artificial microswimmers [21] and also experimental systems of self-propelled particles at the mesoscale, such as vibrated polar disks [24] or small robots [22].

The reason for the great interest shown by physicists in active matter relies on the fact that those systems do not respect thermodynamic equlibrium because of the continuous injection of energy in the system, becoming excelent case studies for out of equilibrium systems. Due to this far from equilibrium nature and to their intrinsic complexity, active matter systems display a variety of collective properties, emergent phenomena and large-scale pattern formation [66],[80]. Notable examples are the emergence of vortices when active particle assemblies found themselves in confined geometries [7], the formation of clusters [58] and active cristals [6], and phase transitions that differ from the ones typical of passive particles, as we will see in the following.

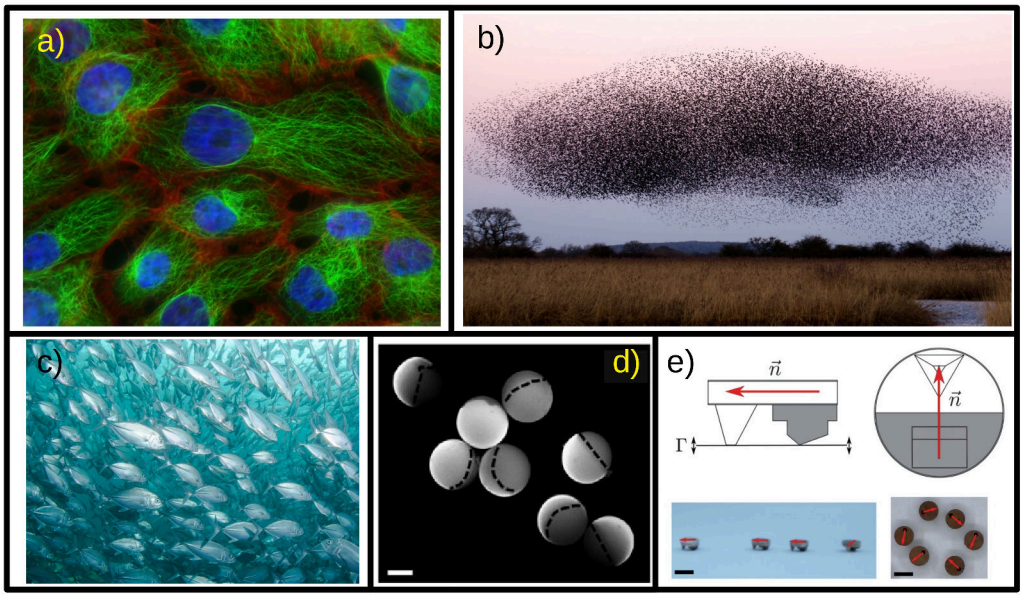

Figure 1.1: Examples of active matter systems (a) Fluorescence image of human breast cancer cells; (b) a flock of birds; (c) a school of fishes; (d) A common type of artificial microswimmers: Janus colloids. In the picture a Scanning Electron Microscopy image spherical silica beads half coated by a platinum layer. Dashed lines show the Janus boundaries. In this case the platinum layer transforms the chemical fuel H_2O_2 added in the environment in which Janus particles moves into water and oxygen, giving rise to a self phoretic propulsion of the colloids. Scale bar is $1\mu m$. (e) A way to obtain systems of active particles at the mesoscale is using vibrated polar disks. The white part of the particle is made of copper-berylium, while the grey part is made of nitrile. The design gives the disks a built-in polarity. When vibrated, the disks self-propelled. Scale bar is $4mm$. Panel (d) is an adaptation from Xiaolu Wang et al. [105], panel (d) is an adaptation from Julien Deseigne et al. [24] Copyright 2012 with permission of The Royal Society of Chemistry.

1.2 Active Brownian Particles

Among the different models used to describe the motion of active particles, we focus on a basic and effective model that will represent the starting point for our study: Active Brownian Particles (ABPs). The Brownian motion of passive particles is driven by equilibrium thermal fluctuations, due to random collisions with the surrounding fluid molecules. The ABPs model extends the Brownian motion to include the ability of a particle to self propel. Self-propelled Brownian particles exhibit an interplay between random fluctuations and active swimming driving them into a far-from-equilibrium state [6]. When dealing with cells, bacteria and microswimmers the assumption of overdamped dynamics is valid, since they usually perform their motion at small Reynolds numbers [6]. In this case, inertial forces are much smaller than the viscous ones and therefore can be neglected in the equations of motion. With this assumption, the equation of motion (e.o.m.) for an ABP in 2D, moving in free space becomes:

$$\frac{d\boldsymbol{x}(t)}{dt} = V\frac{\boldsymbol{v}(t)}{|\boldsymbol{v}|} + \sqrt{2D_T}\boldsymbol{\xi}_(t) \tag{1.1}$$

$$\frac{d\varphi}{dt} = \sqrt{2D_R}\xi_\varphi(t) \tag{1.2}$$

where D_T and D_R represent the translational and rotational diffusion coefficients. In 2D $\boldsymbol{\xi}(t) = (\xi_x(t), \xi_y(t))$. The terms $\xi_x(t)$, $\xi_y(t)$ and $\xi_\varphi(t)$ describe independent white noise stochastic processes with $\langle\xi(t)\rangle = 0$ and $\langle\xi(t')\xi(t")\rangle \propto \delta(t' - t")$. The ABP tends to move in the direction in which it was already moving (see the term $V\frac{\boldsymbol{v}(t)}{|\boldsymbol{v}|}$, in which the direction is given by the unitary vector of the velocity i.e. $\frac{\boldsymbol{v}(t)}{|\boldsymbol{v}|}$) until rotational diffusion changes the direction of motion. The intensity of the self propulsion is described by the term V. In Figure 1.2, the trajectories of some simulated ABPs are shown for different values of the self-propulsion intensity V. This simple mathematical model is able to describe the motion of active particles of biological interest. Liang Li et al., investigating the optimal search strategies of eukaryotic cells, observed that the unicellular amoeba *Dictyostelium discoideum* perfoms trajectories compatible with persistent random walks. This allows the cells to cover more territory in a given number of steps than they would do if they were following simple random walk [59].

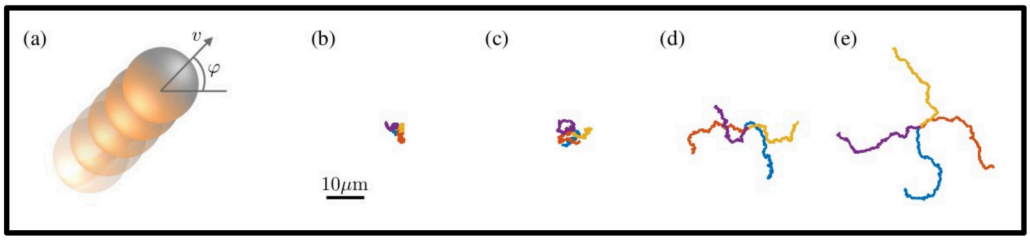

Figure 1.2: Active Brownian Particles (a) Example of an active Brownian particle in 2D. The vector **v** indicates the particle velocity while the angle φ defines particle orientation; in (b), (c), (d) and (e) the simulated 10s long trajectories of four ABPs starting from the same point are shown for different values of the self-propulsion: $V = 0\frac{\mu m}{s}$ so simple Brownian particles, $V = 1\frac{\mu m}{s}$, $V = 2\frac{\mu m}{s}$ and $V = 3\frac{\mu m}{s}$ respectively. With increasing values of v, the active particles move over longer distances before their direction of motion is randomized. The whole figure comes from the review of Clemens Bechinger et al. [6], is reprinted with permission, Copyright 2016 by The American Physical Society.

This model can be easily extended to describe also chiral active matter, in which the particle orientation φ also rotates with angular velocity ω. For ABPs in 2D the term ω should be added to Eq. 1.2, and the sign of ω indicates the particle chirality (clockwise or counterclockwise)[6]. The reasons behind the choice of considering chiral active particles and a more detailed model to describe them, will be illustrated in Chapter 2.

1.3 Phase transitions in active matter

Once that the equations of motion for a single ABP have been defined, the goal is to study what happens to systems composed by multiple active particles, that can interact among themselves. As already mentioned before, in active matter systems, their far from equilibrium nature and the complexity due to multiple interactions give rise to a variety of emergent phenomena. In particular, we will focus on phase transitions in active matter and on their onset as a function of ABPs parameters, highlighting similarities and differences with phase transitions in ordinary matter.

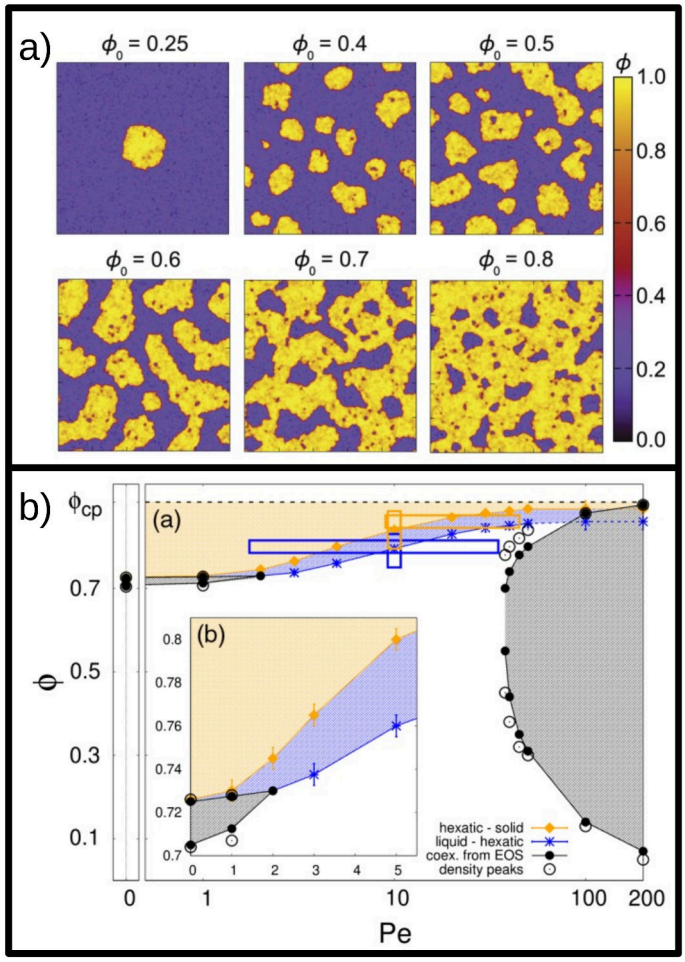

Figure 1.3: Phase transitions in active matter (a) Snapshots of N$\approx 7 \times 10^5$ simulated ABPs at different packing fractions ϕ_0. The colorbar represents the density field. Motility induced phase separation is clearly visible, with dense regions colored in yellow and diluted regions colored in violet. (b) Phase diagram of ABPs, depending on activity (Peclet number Pe) and packing fraction ϕ. In the inset, an enlargement over the low Pe-high ϕ regime highlights the connection with 2D melting. In the black area there is coexistence, in the blue hexatic order and the orange one is an active solid phase. Panel (a) is an adaptation from Joakim Stenhammar et al. [96]. Panel (b) is reproduced from Pasquale Digregorio et al [25] with permission, Copyright 2018 by the American Physical Society.

One of the first researchers to study phase transitions in active matter was Vicsek. He considered a system of self-propelled particles driven with a constant absolute velocity. Those active particles feel an aligning interaction and, at each time step, tend to assume the average direction of motion of the particles in their neighbourhood. Furthermore, random noise is added to the system. He observed that at high density active particles undergo a kinetic phase transition, from random movement when the noise is high to ordered motion on a macroscopic scale (flocking). In the flocking state, when the noise is small, all the particles move in the same spontaneously selected direction[104]. Later on,

it has been observed that self-propulsion itself can induce phase separation in active matter systems. Considering self-propelled disks without alignment rule, with only steric interactions among them, it has been observed that above a certain packing fraction ϕ_c the systems separates into dense and diluted phases, exhibiting giant number fluctuations [34]. This behavior is reminescent of what happens in liquid-gas transitions [86], even if for active matter this behaviour is driven by density and particle motility, rather than temperature. In 2D, as phase separation occurs, domains characterized by different densities of active particles are formed. The system evolves from a phase of isolated dense droplets in a dilute background, when the overall density is low, via an almost bicontinuous phase at intermediate packing fractions, to a phase exhibiting dilute droplets in a dense background at higher densities [96] (see Figure 1.3(a)). Very interestingly, this behavior has been observed not only in simulations but also in experiments involving colloids. In particular this is the case of carbon-coated Janus particles able to self-propel thanks to diffusiophoresis. Even in systems where the density is high, the suspension undergoes a phase separation into large clusters and a dilute gas phase. Furthermore, it has been reported that the mean cluster size increases linearly as a function of the self-propulsion strenght [11]. More recently, Pasquale Digregorio et al. obtained the complete phase diagram of ABP with no alignment interaction in 2D, spanning broad ranges of activity and density. The activity has been quantified by the dimensionless Péclet number Pe, which compares the times needed for diffusive and active motion along a certain distance [110]) while the density has been measured in terms of packing fraction ϕ (see Figure 1.3(b)). At very low activity the melting behavior follows what already found for passive hard disks [46]: a two step process, in which increasing ϕ the transition from liquid to solid passes trough an intermediate hexatic phase, characterized by quasi-long-range orientational order and short-range positional one. Moving along the phase diagram they found, increasing ϕ at low Pe, a coexistence region between active liquid and hexatic phases. Afterwards, going up in density, a fully active hexatic phase is observed, even for higher value of self-propulsion. When the packing fraction is even higher, an active solid phase emerges, for all the values of Pe. Noticeably, the authors observed that the self-propulsion destabilizes the ordered phases, shifting the transition lines at higher ϕ when Pe increases. For high activity, they retrieve a motility induced phase separation (MIPS), in which dilute phase regions cohexist with high density regions that can either be liquid, hexatic or even solid[25]. Examples of phase coexistence between regions with hexatic order and regions in the liquid or gas phase, have been observed also in active purely repulsive dumbbells systems [20].

1.3.1 Jamming

Among all the phase transitions that can occur in a condensed matter system, we focus our attention in particular on the jamming-unjamming transition. When a system jams, it undergoes a transition from a flowing fluid-like state, to a rigid solid-like one. Despite this important change in the dynamics, the internal structure of the system remains disordered both in solid as well as in fluid phase, remarking a fundamental difference with the well known crystallization process [63]. In our everyday experience, we meet a variety of systems that jam. Examples include granular materials flowing through a hopper, that at some point stop flowing due to jamming; or vacuum-packed rice, that due to the close packing of rice grains behaves like a solid, but once we open it (and the rice density decreases) behaves like a fluid. Inspired by the observation of several granular materials, M.E.Cates et al in 1998 suggest that those jammed systems constitute a new class of fragile materials, that resemble solids but have completely different mechanical

properties and an intrinsic disordered nature. No crystalline structure is present, and particles are driven into a jammed state by compressive stress. When jammed, the disordered system is caught in a small region of phase space with no possibility of escape. For Cates et al., what distinguish jammed systems from conventional solids, was that applying even a small stress in a certain direction, the system unjams and particles start to flow. In particular this happens if the direction of the applied stress does not coincide with the direction of the stress that previously caused jamming in the system [13]. But that was only a part of the story. In the same year, Andrea J. Liu and Sidney R. Nagel extended the idea of jammed systems, to include also microscopic systems with attractive interactions, which unjam as the temperature raises. They had in mind supercooled liquids, for which the viscosity increases rapidly, below the freezing point. For this reason, the supercooled liquid can fall out of equilibrium into a disordered glassy state, where it only explores a small part of phase space, just as in the case of a jammed granular material [62].

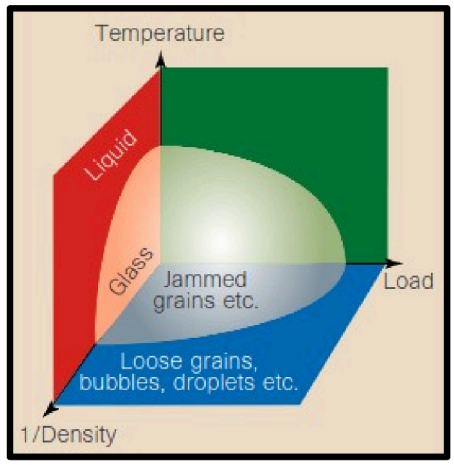

Figure 1.4: A qualitative phase diagram for jamming The jammed region, near the origin, is enclosed by the depicted surface. The line in the temperature-load plane is speculative, and indicates how the yield stress might vary for jammed systems in which there is thermal motion. The figure comes from Andrea J. Liu and Sidney Nagel [62], reproduced with permission of Macmillan Magazines Ltd. Copyright 1998

A new phase diagram has been proposed to unify those behaviors (see Figure 1.4), with interesting physical implications. Looking at the diagram, we observe that jamming occurs only when the density is high enough. Furthermore, there are several ways of unjamming a system, either by raising temperature (so as to increase thermal fluctiations) or by applying a stress. The behavior of particles close to the jamming point was further investigated, to better understand the nature of this phase transition. O'Hern et al. observed systems of repulsively interacting particles at zero temperature and zero applied stress. They found that at low density, the system is not jammed and each particle can move without impediment from its neighbors. Then, increasing the packing fraction, there is a jamming threshold ϕ_J at which particles can no longer avoid each other, and the bulk and shear moduli simultaneously become nonzero, clearly remarking the occurence of a phase transition [74]. We focus our attention on this peculiar phase transition because it has been observed to occur, not only in granular and simulated glassy systems, but also in active matter systems of biological interest, like groups of cells[88].

The study on human bronchial epithelial cells (HBECs) derived from non-asthmatic and asthmatic donors, to get insight on the mechanical basis of this disease, carried out by Jin-Ah Park et al.[76] is, in this respect, emblematic. The authors found that increasing the pressure on a layer of HBECs, applying a compressive stress mimicking bronchospasm (as it happens in asthma), causes a phase transition in the cells layers, that move from a solid-like jammed phase to a fluid-like unjammed phase. After the response to the stress, the authors hypothesize that the bronchial cells can explore various possible configurations while in the flowing phase, and then resettle into an adaptive quiescent, jammed, solid-like state, effecting a sort of self-repair in that remodelled state. Interestingly, they observed that the onset of this 'quiescent' jamming transition is delayed in patients affected by asthma, revealing a difference in physical properties between cells coming from healthy and ill patients. In a recent paper by Oleksandr Chepizhko et al., the authors studied the collective invasion of human cancer cells (HeLa cells). They found that boundary conditions (in this case the free space due to a wound opened in a cells layer) can cause a transition from a jammed to an unjammed flowing state, where cells can collectively migrate [17]. In Chapter 2 we will investigate the jamming-unjamming transition in a system of active rotators and in Chapter 3, inspired also by wound healing experiments, we will study the invasion properties of a system ABPs in a jammed phase.

CHAPTER 2

Unjamming of Active Rotators

2.1 Introduction

Studies on active matter systems typically consider self-propelled particles, for which the activity is modeled as a force that, at each step, pushes the single particle in the direction of its previous motion, sustaining a translational movement of the particle, as showed in Chapter 1 for ABPs. However, observing some natural examples of active matter, such as bacteria [56] and spermatozoa [106] swimming near surfaces, it is possible to notice that, beside translational motion, they are able to perform circular trajectories. Those are not the only cases in which rotational motion plays a key role in biological active particles motion. In our study, we were inspired by an alga, often used as model system, called *Chlamydomonas reinhardtii*: a micron-sized unicellular alga that moves thanks to two flagella (see Figure 2.1.a). Experimental observation of *Chlamydomonas reinhardtii* have shown that those organisms not only self-propel to perform translational motion in space, but they also have the ability to sustain a rotational motion around their centre, so to self-rotate.

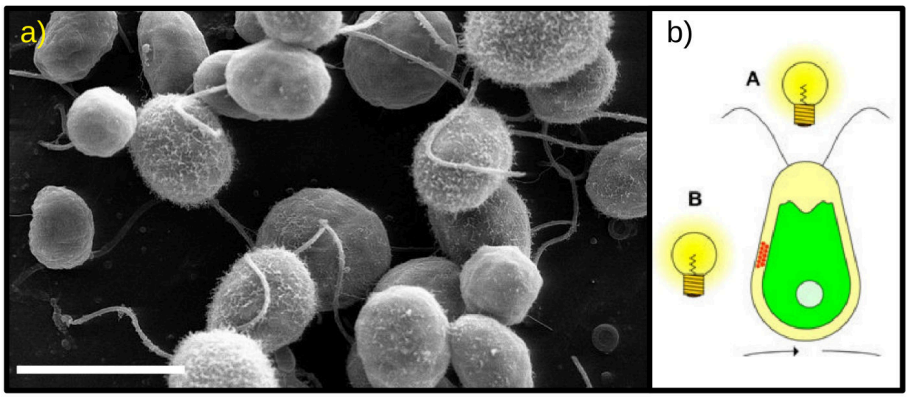

Figure 2.1: Chlamydomonas reinhardtii (a) Scanning electron microscope image showing an example of the unicellular algae *Chlamydomonas reinhardtii*. The flagella they use to swim are clearly visible. Scalebar is 10 μm. Courtesy of the Dartmouth Electron Microscope Facility. (b) Scheme of a *Chlamydomonas reinhardtii* alga where the eyespot sensitive to light is colored in red. Since the eyespot is localized near the cell equator, the alga tend to rotate around its center trying to span the surrounding envinroment with the eyespot. Panel (b) is an adaptation from William Guilford et al. [39].

This peculiar behavior is due to the morphology of this alga, that has an 'eyespot' sensible to light located near the cell equator. Rotating around its own axis, the alga allows the eyespot to better scan the surrounding envinroment, looking for light needed to perform photosyntesis [18]. As a starting point, we have performed some observations of the behavior of *Clamydhomonas rheinardtii*; the analysis of videos obtained from experiments on algae, including PIV analysis of algae velocities, will be showed in the following paragraphs. Interestingly, we observed both single algae rotation and the formation of rotating clusters, in analogy to what observed for model systems of active rotating particles in 2D passive media [2]. Starting from this natural evidence, we decided to study a system composed by 2D disks with the ability to self-rotate, to extensively study the role of self-rotation in active matter systems. This is similar, in some ways, to what is considered in the studies about chiral active fluids, in which the single particles are spinning with a defined chirality, and for this reason show peculiar physical characteristics. Those include an odd (or Hall) viscosity due to breaking both parity and time-reversal symmetries [4] and the emergence of active turbulence behaviour [50]. However, our aim is to investigate the phase transitions that such system of active rotators can undergo. In particular, we focus on a specific kind of phase transition: the jammed-unjammed one. This transition, described in more detail in Chapter 1, is similar to a glassy transition, but driven by density, not by temperature. Increasing the density, the system goes from an unjammed liquid-like phase to a jammed solid-like state, characterized by limited mobility and slow relaxation [62]. Since this kind of transition has been observed to take place also in systems of living cells and to have a role in biological processes (such as inside the epithelial tissues of patients affected by asthma [76] or in the migration of cancer cells in wound healing experiments [17]), with our work we want to determine if and how self-rotation influences the jamming-unjamming transition.
To reach this goal, we simulated a system of interacting bidimensional active disks and we modelled self-rotation as an active torque applied at each particle. With our model, we performed extensive molecular dynamics simulations using LAMMPS (`http://lammps.sandia.gov`.) [100], to characterize the role of self-rotation on the jamming-unjamming phase transition of a system of bidimensional disks. The description of the method, the results and their discussion are the objects of the following paragraphs.

2.2 Materials and Methods

2.2.1 Experiments

Thanks to the multidisciplinary of the Center for Complexity and Biosystems, it was possible to compare the results, obtained with our 2D model of interacting active discs, with the quantitative observations made on the algae *Chlamydomonas reinhardtii*. The following section details the procedure used to obtain the experimental images and to analyse them.

C. reinhardtii culture growth and exposure to stress conditions

C. reinhardtii cells were growth in TAP medium (Invitrogen) as batch cultures until they reached $1 - 2 \times 10^6 cells/ml$ (corresponding to mid-exponential phase of growth). The cells were cultured under continuous cool-white fluorescent lamps ($\simeq 100 \mu molphotons/m^2 s$) within a $110 rpm$ shaking incubator, at $25°C$. For palmelloid analysis, $5ml$ of cells was spun at $1100g/5min/25°C$ and resuspended in $20ml$ of TAP medium containing $150mM$ NaCl or in fresh TAP growth medium (control condition) for 6 hrs. 200 μl of cultured

cells for each experimental condition were seeded in a 96 well and time-lapse imaged immediately. For study of motility at different densities, 200 μl of cultured cells ($2 \cdot 10^6 cells/ml$ and $10^6 cells/ml$ respectively) were let sediment on the bottom of a 96 well before imaging. Images were acquired with DMi8 (Leica), using bright field objective at 20x at $0.5 - 6$ frames per second. Experiments have been performed by the Oncolab group at the Center for Complexity and Biosystems.

Image segmentation

Image segmentation is done using standard Matlab functions for the image processing. First, the image is thresholded using the `edge` function in two steps: the automatic threshold is identified, and then lowered to achieve better edge detection. The detected edges are dilated using the `imdilate` function. Then, the closed areas are filled with the `infill` function, to remove black spots inside detected algae. Finally, `beaware` open is used to remove small noise. The result is a mask that selects only regions occupied by algae.

Particle image velocimetry (PIV)

The measurements of the velocity and vorticity fields were done using PIVlab app for Matlab [99]. The method is based on the comparison of the intensity fields of two consequent photographs of algae. The difference in the intensity is converted into velocity field measured in $px/frame$ and then converted to $\mu m/h$ [16]. To avoid spurious noise PIV was applied after image segmentation only on the regions occupied by algae. PIV analysis has been performed by our collaborator Oleksandr Chepizhko at University of Innsbruck.

Cell tracking

The tracking and motion analysis of algae in 2D is performed using Trackpy: a particle-tracking toolkit written in Python, available at `https://zenodo.org/record/3492186`. The original implementation of the tracking algorithm is reported in the work of J.C. Crocker and D.G. Grier [19]. The first step of the tracking procedure consists in the location of the algae in each image to extract their coordinates. For this purpose we set the function `locate`, performing a band pass and a threshold, with the following parameters: diameter=17, minmass=10^5, separation=5, invert=True. The function `annotate` allows the direct visualization of the detected particles. Afterwards, the algorithm links the coordinates in time to extract the trajectories (function `link` with parameters: search range=3, memory=5). The drift motion is then computed and subtracted away (using the `compute_drift` function) and the final trajectories are obtained. The trajectories are analysed with the `msd` function to compute the ensemble mean square displacement (MSD) of all the algae. The cell tracking procedure has been performed in our group by Silvia Bonfanti.

2.2.2 Simulations

Model for interacting 2D active disks

We performed Molecular Dynamics simulations of a system made of active self-rotating particles using LAMMPS (Large-scale Atomic/Molecular Massively Parallel Simulator)[100].

We build our model such as each particle (described as a 2D disk) has the following physical properties:

- it is an active particle and it has the ability to both self propel, to move in a straight direction, and to self-rotate around its center
- it is moving on a viscous medium, performing a Brownian motion
- it interacts with the nearest neighbor other particles via a granular potential (Hertzian potential) to which we add an adhesion term (Derjaguin-Muller-Toporov Model[23]). This is done to take into account the adhesion properties of cells.

The equations of motion describing the center of mass position $\boldsymbol{x}_i(t)$ and the rotational angle $\theta_i(t)$ of the two dimensional disk *i* at time *t* are given by:

$$\frac{d^2\boldsymbol{x}_i(t)}{dt} = \frac{1}{m}[\boldsymbol{\Gamma}_i(t) + \boldsymbol{\chi}_i(t) + \boldsymbol{\Phi}_i(t) + \sum_{n.n.} \boldsymbol{\Psi}^n_{ij}(t) + \sum_{n.n.} \boldsymbol{\Lambda}_{ij}(t)] \tag{2.1}$$

$$\frac{d^2\theta_i(t)}{dt} = \frac{1}{I_z}[\Upsilon_i(t) + \Theta_i(t) + \tau^i_z(t) - \sum_{n.n.} (\boldsymbol{R}_i \times \boldsymbol{\Psi}^t_{ij}(t))_z] \tag{2.2}$$

Here the sums are over the nearest neighbour (n.n.) disks and $\boldsymbol{R}_i$ is a vector normal to the disk surface and of amplitude equal to the disk radius. It should be noticed that we have considered in our system particles with two different radii in order to avoid crystallization. The quantities in Eq. 2.1 and 2.2 are dimensionless because units are set to Lennard-Jones units in LAMMPS. It is, however, always possible to convert them to real units, by setting the disk radius to the typical algae radius. Since the particle is moving in a viscous environment, the term $\boldsymbol{\Gamma}_i(t)$ takes into account the friction due to the surrounding medium. Its value is:

$$\boldsymbol{\Gamma}_i(t) = -\frac{m}{\beta}\boldsymbol{v}(t) \tag{2.3}$$

As we can see, this term is proportional to the linear velocity $\boldsymbol{v}(t)$ of the particle and to the particle mass m. The input parameter β is inversely proportional to the fluid viscosity. Since cells moving in a medium are usually in an overdamped regime, we set $\beta = 0.1$ so that Brownian dynamics can effectively be considered as an overdamped Langevin dynamics.
Friction enters also in the rotational motion of our $2D$ disks, since we have a friction term proportional to the angular velocity and to the moment of inertia I of the disks, given by:

$$\Upsilon_i(t) = -\frac{10}{3}\frac{I}{\beta}\omega(t) \tag{2.4}$$

Next, we consider in equation 2.1 and 2.2 a term representing random noise, described by $\boldsymbol{\chi}_i(t)$ and $\Theta_i(t)$. From the fluctuation/dissipation theorem, the magnitude of $\boldsymbol{\chi}_i(t)$ is proportional to $\sqrt{\frac{K_b T m}{dt\beta}}$, where K_b is the Boltzmann constant, T is the temperature, m is the mass of the particle, dt is the timestep, and β is the damping factor. In the case of $\Theta_i(t)$, the mass in the previous equation is substituted by the moment of inertia I. The random noise is uncorrelated with $\langle\xi(t)\rangle = 0$ and $\langle\xi(t')\xi(t")\rangle \propto \delta(t' - t")$.
Since our aim is to describe active particles, we include in 2.1 and 2.2 terms taking into account the ability of the particle to self sustain its motion. The term $\boldsymbol{\Phi}_i(t)$ takes into

account the ability of the cell to self-propel. The biological mechanisms that allow the cell to move, like cytoskeleton rearrangements, are simply modelled as a force with a constant modulus, pointing in the direction in which the particle was already moving, considering a characteristic time until the particle can change direction:

$$\boldsymbol{\Phi}_i(t) = V\frac{\boldsymbol{v}(t)}{|\boldsymbol{v}|} \tag{2.5}$$

The term $\tau_z^i(t)$ takes into account the self rotation of the particle, adding a constant torque along the $\widehat{\boldsymbol{z}}$ direction at each time step for each particle. At the beginning of the simulation, particles are endowed with an initial angular velocity, either clockwise or counterclockwise. The torque term initially follows the direction of rotation, so that a particle that moves clockwise at the beginning, continues to rotate in that direction under the self rotation effect. Of course, changes of rotation direction (i.e. from clockwise to counterclockwise) can arise due to interaction among particles. In order to study the effect of rotation on the collective properties of our system, we performed simulations for different values of the active torque τ_z.
In the overdamped limit, Eq. 2.1 and 2.2 without the interaction terms can be reconducted to the Active Brownian Particle model described in Chapt. 1. Then we have to consider the interaction terms, calculated for the nearest neighbour particles. The term $\boldsymbol{\Psi}_{ij}(t)$ describes contact interactions between the particles, according to the Hertzian model [8] [94]. In particular the form of the force is:

$$\begin{aligned}\boldsymbol{\Psi}_{ij}(t) =&\sqrt{\delta}\sqrt{\frac{R_iR_j}{R_i+R_j}}[(k_n\delta\widehat{\boldsymbol{n}}_{ij} - m_{eff}\gamma_n\boldsymbol{v}_n)+\\ &-(k_t\boldsymbol{\Delta s_t} + m_{eff}\gamma_t\boldsymbol{v}_t)]\end{aligned} \tag{2.6}$$

where R_i and R_j are the radii of the interacting disks. In our simulations, disks have two different radii $R_1 = 1.96$ and $R_2 = 1.4$, to avoid crystallization. The force is divided in two components: the force that is normal to the contact surface between the two particles and the one that is tangential. The normal force has two terms, a contact force and a damping force. Here δ is the overlap distance between two particles, k_n is the elastic constant for the normal contact, $\widehat{\boldsymbol{n}}_{ij}$ is the unit vector along the line connecting the centres of the two interacting disks, γ_n is the viscoelastic damping constant for normal contact and $\boldsymbol{v}_n$ is the normal component of the relative velocity of the two particles. This component of the force enters in 2.1, influencing the equation of motion of the center of mass of the disk.
The tangential force also has two terms: a shear force and a damping force. The shear force contains an "history" effect, that accounts for the tangential displacement between the particles for the duration of the time they are in contact. Here k_t is the elastic constant for tangential contact and $\boldsymbol{\Delta s_t}$ is the tangential displacement vector between two particles. In the tangential damping force, the term γ_t is the viscoelastic damping constant for tangential contact and $\boldsymbol{v}_t$ is the tangential component of the relative velocity of the two particles. This tangential component of the Hertzian interaction enters in the rotational part of the e.o.m, via the torque $-\boldsymbol{R}_i \times \boldsymbol{\Psi}_{ij}^t(t)$.

Then, to study the role of adhesion between particles, typical of many biological systems, a term taking into account the adhesion is inserted in 2.1. This is done using the Derjaguin-Muller-Toporov model [23] [5], where the adhesive force has the form $\boldsymbol{\Lambda}_{ij}(t) = -\frac{A_{cc}R_{ij}\widehat{\boldsymbol{n}}_{ij}}{6\epsilon^2}$, where A_{cc} is the Hamaker constant that takes into account the coefficient of the particle-particle pair interaction, $R_{ij} = \frac{R_iR_j}{R_i+R_j}$ is the effective radius

of the two touching particles and ϵ is the least possible spacing between the contact surfaces. In particular, the adhesion force is calculated in the LAMMPS code *pair-dmt* distinguishing between two cases. If the distance among the centres of two disks is bigger than the sum of the radii $r > R_1 + R_2$, the adhesion force takes the form $\mathbf{\Lambda}_{ij}(t) = -\frac{A_{cc} R_{ij} \widehat{\boldsymbol{n}}_{ij}}{6[r-(R_i+R_j)+\epsilon]^2}$; otherwise the adhesion force becomes $\mathbf{\Lambda}_{ij}(t) = -\frac{A_{cc} R_{ij} \widehat{\boldsymbol{n}}_{ij}}{6\epsilon^2}$.
The adhesion is simply represented by a spring force, when two particles overlap. In the following we studied the role of adhesion, performing simulations with different values of the Hamaker constant A_{cc}.
Integrating the Equations 2.1 and 2.2, it is possible to update positions and velocities of the particles at each time step of our simulation.

Parameters used for the simulations

We used 1000 2D disks, 500 with radius $R_1 = 1.96$ and 500 with radius $R_2 = 1.4$. The density of the disk is set to $d = 0.46$ (so mass $m = d \cdot \pi R^2$). We used a time step of 0.0001 in LJ units and run the simulations for 10^6 steps, covering 100 time units. The temperature is constant during the integration of the equation of motion and equal to $T = 1$. The parameters used to define the interaction potentials are listed in Tab. 2.1, together with all the other parameters used in the simulations. All the quantities are dimensionless since units are set to Lennard-Jones units in LAMMPS.

Table 2.1: Parameters used for the simulations

Parameter	Value	Comments
radius R_1	1.96	
radius R_2	1.4	
d (density)	0.46	$mass = d \cdot \pi R^2$
neighbor bin	0.2	
k_n	400000	$k_t = \frac{2}{7} k_n$
γ_n	100	$\gamma_t = \frac{1}{2} \gamma_n$
x_μ	0.5	static yield criterion
c_{DMT} R_1 and R_1	5.88	cutoff of the DMT potential (center to center)
c_{DMT} R_1 and R_2	5.04	cutoff of the DMT potential (center to center)
c_{DMT} R_2 and R_2	4.2	cutoff of the DMT potential (center to center)
A_{cc}	from 39.5 to 39500	Hamaker constant
σ	1.0	interatomic distance
timestep	0.0001	
number of steps	10^6	
V	0.0	self propulsion amplitude
τ_z	from 0 to ± 10000	self rotation
$T_{start} = T_{stop}$	1.0	same temperature of the initial configuration
β	0.1	

The values illustrated in Table 2.1 have been chosen to properly show different behaviours of the system of interacting active particles, spanning the adhesion and self-rotation strength parameters. For a better comparison with experimental results, it is possible to convert the above unitless LJ parameters into physical quantities defining reference values for mass, distance and energy. Typical values for mass and size of the

cells we want to describe with our active matter model can be easily obtained from literature and experimental data, and used as conversion factors. Yet the difficult part is to set a typical energy scale in an out-of-equilibrium system where friction is also present. From the experimental side, data on typical interaction energies for *Chlamydomonas reinhardtii* are not available and, more in general, quantitative data on cells interaction energies are fairly rare. The value of the Hertzian constant k_n have been chosen to describe quite rigid objects and to follow the suggestions of LAMMPS example code for granular particles.

2.3 Results

2.3.1 Active rotators in the diluted limit

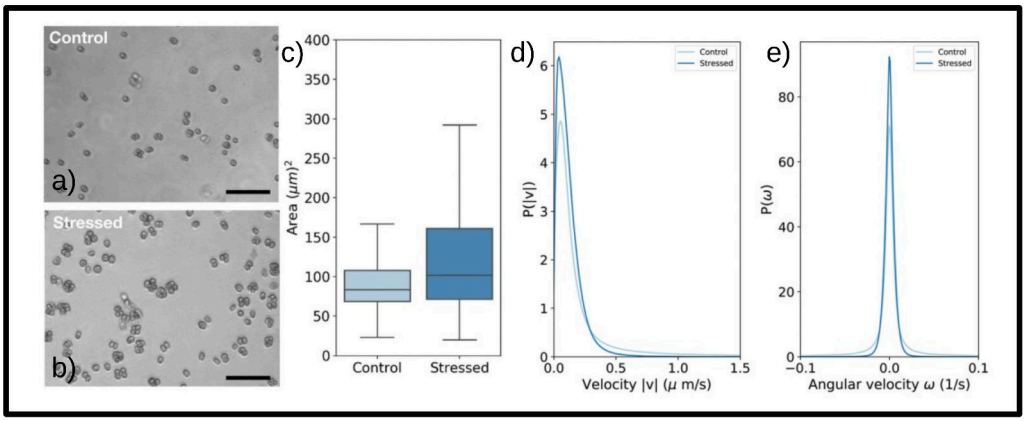

Figure 2.2: Chlamydomonas reinhardtii in the low density regime and their response to stress Typical snapshots of *C. reinhardtii* suspensions (scale bars 50 mm) at low density with (b) and without (a) the stress induced by the presence of NaCl are shown together with a boxplot of cluster areas (c), the distribution of the absolute value of the linear velocities $P(|v|)$ (d) and the distribution of the angular velocities $P(\omega)$ (e).

To quantify self-rotation in *C. reinhardtii*, we first consider the diluted limit, shown in Fig. 2.2, and perform a PIV analysis to reconstruct the probability distributions for linear and angular velocities (also reported in Fig. 2.2.d and 2.2.e). The plots show that the distributions of the absolute value of the linear velocities follows a Rayleigh-like distribution, while the angular velocity distribution has a Gaussian-like behaviour. When algae are stressed by adding 150 mM NaCl added to the medium, we observe the formation of rotating clusters because these algae tend to aggregate in response to stress. The probability distributions obtained under stress indicate that aggregation leads to a decrease of velocity and angular velocity fluctuations. To explain these experimental observations and gain insight on those systems of active rotators, we perform simulations in LAMMPS, using the model described in the model section.

We consider a low density system with a packing fraction $\phi = \frac{V_{particles}}{V_{TOT}} = 0.14$ and active torque $\tau_z = 10$. When adhesion is switched off ($A_{cc} = 0$), the active particles do not form clusters and rotate mostly individually (see Fig. 2.3.b). When adhesion is present, however, particles aggregate into clusters as shown in Fig. 2.3.a and 2.3.b (obtained for $A_{cc} = 3950$). From the simulations, we also extracted the probability distributions for

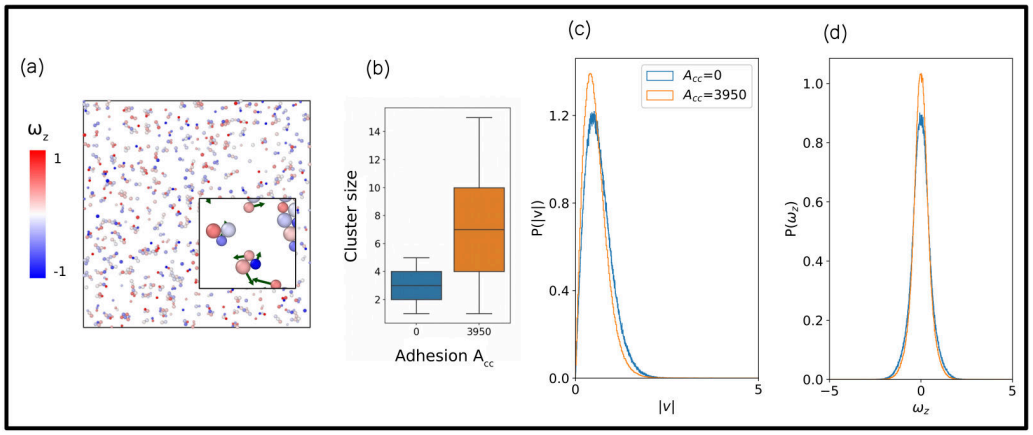

Figure 2.3: Active rotators in the low density regime (a) Snapshots of the simulations at low density $\phi = 0.14$ in presence of active torque ($\tau_z = 10$) with adhesion ($A_{cc} = 3950$). Particles are coloured according to their angular velocity ω_z . The formation of clusters is clearly visible. In the inset a zoom of a portion of the simulated box is shown, together with the velocity vectors of the particles. In particular it is easy to see a system of three collectively rotating particles. We also show a boxplot of cluster sizes (b) and the distributions of velocities (c) and angular velocities (d) with and without adhesion. All the quantities are dimensionless as explained in Section 2.2.2

the linear and angular velocities of the particles, in the cases with and without adhesion (see Fig. 2.3.c and 2.3.d). The distributions obtained from the model are very similar to those observed in experiments (see Fig. 2.2), suggesting that our model can capture some important features of those biological system.

2.3.2 Active rotators in the dense regime

After comparing model and experiments in the dilute regime, we investigate how the self-rotation of the disks can affect the phase behaviour of a dense system of interacting rotators. We first analyse, with PIV, the motion of *C. reinhardtii* at higher densities. We find that increasing the density, the algae became more motile, since the linear velocity peak is shifted toward higher values and the variance of the angular velocity distribution increases (compare the distributions in Fig. 2.2 and Fig. 2.4). Visual inspection of the velocity and vorticity maps obtained by PIV shows that algae rotate and tend to form rotating clusters and vortex like behaviour (see Fig. 2.4).

The experimental observation that the density increase leads to higher mobility can not easily be explained by the model. If we only increase the density, keeping all the other parameters constant, the mobility progressively decreases until the system jams. This is the typical behaviour expected for inactive jamming phenomena [62]. In this active system, however, a possible explanation is that algae respond to crowding by increasing their active torque. We therefore study numerically the effect of self-rotation in a dense system of active rotators. To improve the statistics, our numerical results are averaged over ten initial configurations, initially placed into a jammed phase. To this end, we create a simulation box with 1000 disks in random positions (500 with radius $R_1 = 1.96$ and 500 with radius $R_2 = 1.4$, corresponding to a binary mixture with diameter ratio of 1.4, as in previous studies on jamming of a 2D disk packing [71],[74]). We then performed subsequent steps of box reduction and energy minimization, monitor-

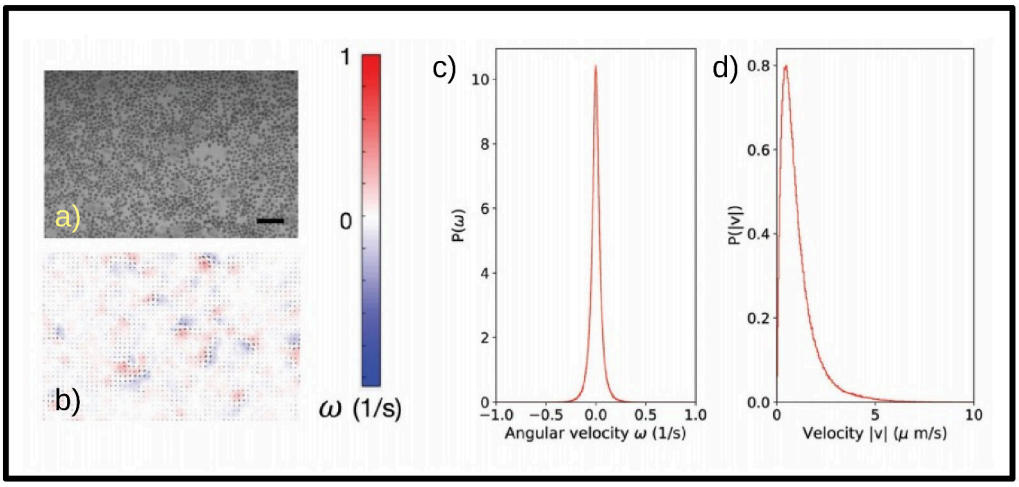

Figure 2.4: Chlamydomonas reinhardtii in the high density regime (a) Typical snapshot of a *C. reinhardtii* suspension at high density (scale bars 100 mm); (b) corresponding map of angular velocities obtained by PIV. Vortex-like behaviour is visible. In (c) we report the plot of the probability distribution of the angular velocity $P(\omega)$ and in (d) the plot of the absolute value of the linear velocity $P(|v|)$.

ing the behaviour of the pressure of the system as a function of the packing fraction ϕ. It is already known from previous studies on random packing of frictionless particles that ϕ at which the pressure becomes non zero is the same as the jamming threshold, when also the static shear modulus becomes non-zero [71]. This can be understood by thinking that when the packing fraction is small, particles do not touch and the internal pressure is zero. Increasing the particle density via box reduction, the system reaches a state in which the particles touch and are blocked into a rigid structure. At this point, further increase of the packing fraction will lead to a pressure increase. Hence, pressure is a good indicator of the jamming point.

In our case, we observe that the pressure is zero until $\phi \backsimeq 0.78$ and increasing rapidly for larger values of ϕ. To ensure that the system is in the jammed state, we chose initial configurations with $\phi = 0.87$. Previous work on packing and jamming of 2D bidisperse hard disks at $T = 0$ shows that the value for random close packing ϕ_{RCP} (maximum density with- out crystallization) is $\phi = 0.84$ [74]. Here, we are considering friction so that jamming is reached at a density lower than ϕ_{RCP} . Furthermore, we are considering a system that is not at zero temperature. Thus, as suggested by the jamming diagram proposed by Liu e Nagel [62], the jamming transition is expected to occur at a higher density. These facts justify the value we found for the onset of jamming. Recent observations found that the critical value of the density at which the jamming transition takes place can depend also on the conditions in which the system has been prepared and varies also within the same material [52], making it hard to find a well defined value of the packing fraction for the onset of jamming. Furthermore, we have to consider that our 2D disks are not hard: their 'hardness' is controlled by the k_n coefficient in the Hertzian potential. Thus, they can overlap and elastically deform, reaching higher values of packing fractions. We perform MD simulations starting from the initial jammed configurations and increasing the value of the active torque τ_z. When self-propulsion is switched off ($V = 0$) together with the adhesion term ($A_{cc} = 0$), we noticed that, at low active

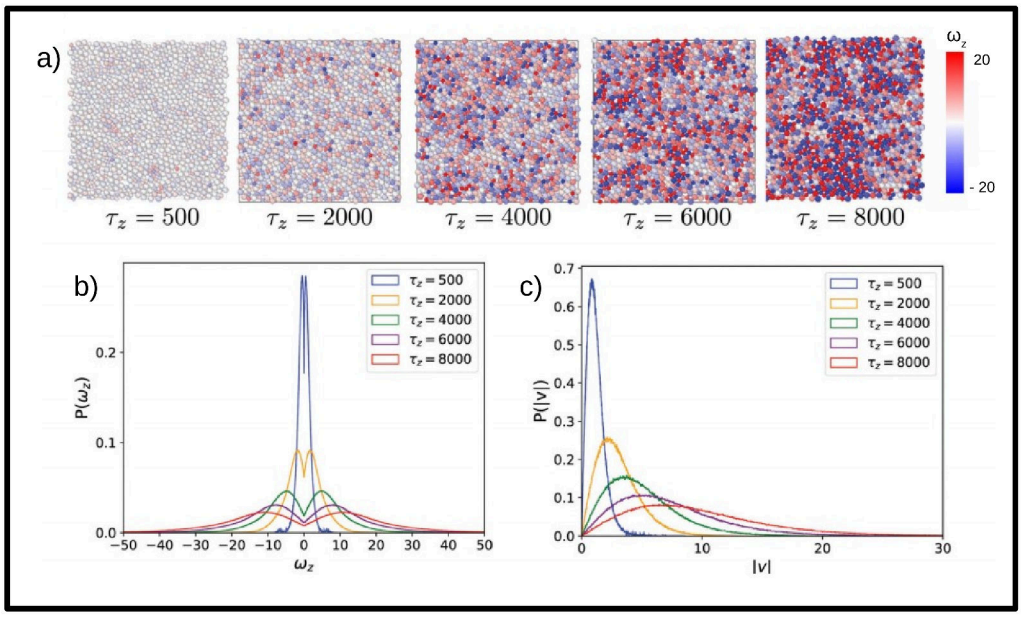

Figure 2.5: Rotators in the high density regime (a) Typical snapshots of the system of active rotators at high density for different values of the active torque. Below we show the corresponding plots of the distributions of angular velocities $P(\omega_z)$ (b) and of the linear velocities $P(|v|)$. All the quantities are dimensionless as explained in Section 2.2.2

torques, the system stays in a jammed phase, characterized by a very low mobility of the active disks. Above a critical value of the active torque, the system switches to a flowing, unjammed phase, characterized by a high mobility of the disks. Fig. 2.5.a reports typical snapshots of the simulations for different values of the active torque, highlighting the internal rotations of the disks. We then analysed the probability distribution of linear and angular velocities and, as shown in Fig. 2.5.b and Fig. 2.5.c , we observe that disks increase their velocities in response to the active torque. The distribution of the linear velocities is qualitatively similar to the experimentally measured one (Fig. 2.4.d), while the distribution of angular velocity displays two peaks, reflecting the constant active torque used in the simulations. The active torque in algae is likely not constant, explaining the difference between simulations and experiments.

2.3.3 Rotational induced unjamming transition

To gain insight on the mobilization of the jammed active disks, we studied individual trajectories of the disks, computing their mean square displacement (MSD). We first consider the experimental data and perform tracking of individual algae. Fig. 2.6.a reports an example of the recorded trajectories which displays a diffusive behaviour, as show in Fig. 2.6.b.

We then perform a similar analysis on the simulations, and in Fig. 2.6.c, we show that in the jammed phase trajectories are localized (see inset of Fig. 2.6.c), while for higher values of the active torque they spread. The mean square displacement is close to zero for low torques, while it grows linearly for larger values of the self-rotation (Fig. 2.6.d and 2.6.e). From a linear fit of the long time region of the MSD, we also extracted an effective

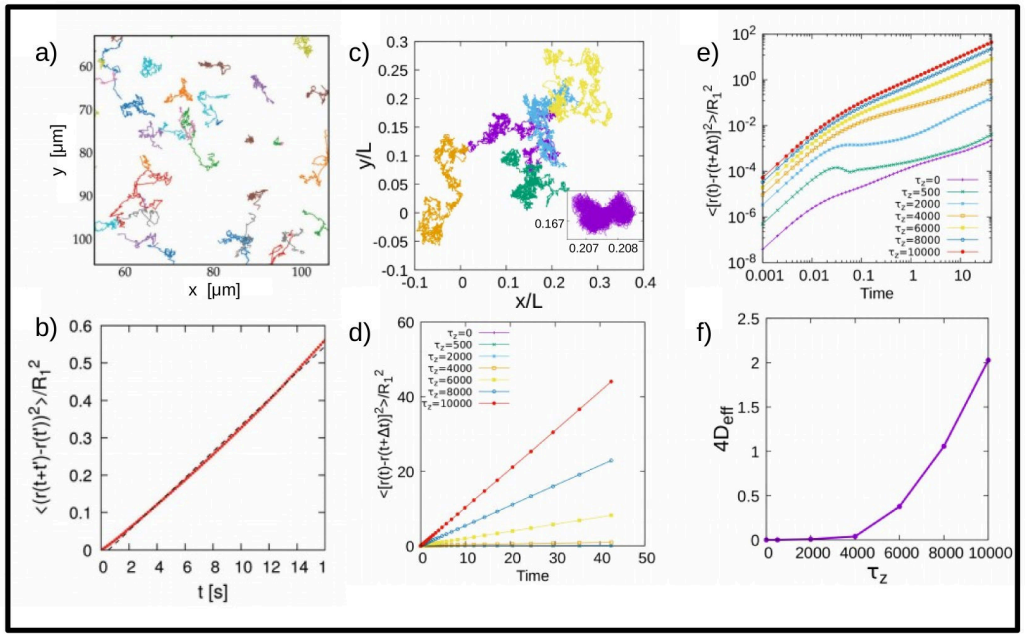

Figure 2.6: Rotational unjamming (a) Trajectories of randomly selected algae for experimental conditions similar to those reported in Fig. 2.4.a. (b) Mean-square displacement of the experimental trajectories, showing diffusive behaviour. (c) Selected trajectories obtained in simulations for the system in the jammed phase ($\tau_z = 500$ in the inset) and in the system in the unjammed phase ($\tau_z = 8000$, main plot). In both plots, the coordinates are rescaled using the length of the simulation box L. (d) The time evolution of the mean-square displacement averaged over all the disks belonging to the system of active rotators is shown for different values of the active torque, showing a clear increase for increasing values of the disks self rotation. (e) The same plot as in (d) is reported also in logarithmic scale. (f) The diffusion coefficient, obtained from a linear fit of the long time region of the mean square displacement is plotted. The increase after a critical value of the active torque τ_z is associated to a crossover from a jammed/solid-like phase to an unjammed/flowing phase of the system. All the quantities in panels (c),(d),(e) and (f) are dimensionless as explained in Section 2.2.2.

diffusion coefficient, that clearly shows a sharp increase at ($\tau_z = 4000$), suggesting a crossover towards a flowing state (Fig. 2.6.f). Since we have seen that the self-rotation can lead from a jammed to an unjammed state, it is interesting to investigate the role of adhesion. This is present in many cellular systems, including *C. reinhardtii* where it could be triggered by stress. As discussed in the Model section, adhesion is modelled using the Derjaguin– Muller–Toporov model; the parameter used to tune the intensity of the adhesion force in the simulations is the Hamaker constant A_{cc} .

We performed simulation with $\tau_z = 6000$, so starting in the unjammed phase and switching on the adhesion term. Analysing the mean square displacement and, as before, the effective diffusion coefficient, it emerges that increasing the adhesion strength the system remains unjammed until a critical value ($A_{cc} \sim 1500$–2000) at which diffusion is strongly reduced, unveiling a transition to a jammed phase (Fig. 2.7).

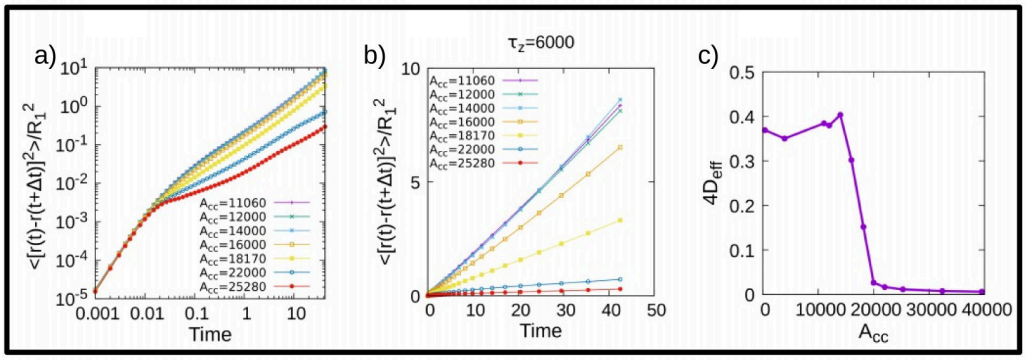

Figure 2.7: The role of adhesion The mean square displacement of the system in the unjammed phase ($\tau_z = 6000$) and high density ($\phi = 0.87$) is shown for different values of the Hamaker constant A_{cc} , that defines the intensity of the adhesive potential among the particles. Results are reported in (a) logarithmic and (b) linear plots. Increasing the strength of the adhesion, the mean square displacement decreases. (c) The effective diffusion coefficient averaged on all the disks is extracted from the linear fit of the mean square displacement. Here the crossover from the unjammed to the jammed phase is clearly visible as the diffusion coefficient rapidly drops to zero for large adhesion strengths. All the quantities are dimensionless as explained in Section 2.2.2.

2.3.4 Self-rotation and self-propulsion

We next consider the interplay between self-propulsion and self-rotation, exploring the behaviour of the system in terms of two parameters τ_z , the active torque and V, the self-propulsion. We consider a system of disks placed at the jamming density ($\phi = 0.87$) without adhesion. We scan the parameter space and record the trajectories of disks. We then compute the mean-square displacement and estimate the effective diffusion constant D_{eff} for each case. Fig. 2.8.a reports the variation of the effective diffusion constant as a function of the active torque, in presence of a relatively weak self-propulsion ($V = 25$). The curve shows that increasing self- rotation leads to a rapid reduction of diffusion. Further increase in the self-rotation, however, induces an increase in the diffusion. This non-monotonic behaviour is due to the fact that, in absence of self- rotation, self-propulsion leads to coherent directed motion. We have checked that this coherent motion is not an artefact of periodic boundary conditions, but persists also for closed boundary conditions. Self-rotation breaks the coherence of the self-propelled motion, inducing jamming. Rotational-induced unjamming is then observed for higher values of the active torque. In absence of self-rotation, unjamming is driven by self-propulsion (see Fig. 2.8.b), as already observed in many active particle models. All the numerical simulations can then be summarized into a qualitative phase-diagram, reported in Fig. 2.9, where we plot the effective diffusion constant as a function of V and τ_z .

2.4 Discussion and Conclusions

Our work was inspired by the observation of a natural example of active rotators like *C. reinhardtii*. Quantification by image segmentation and PIV analysis shows that this kind of algae can not only self-rotate [18], but also aggregate forming collectively rotating clusters. The formation of these aggregates is observed both in high density limit, and at low density in presence of a stress agent, such as NaCl. Starting from these simple

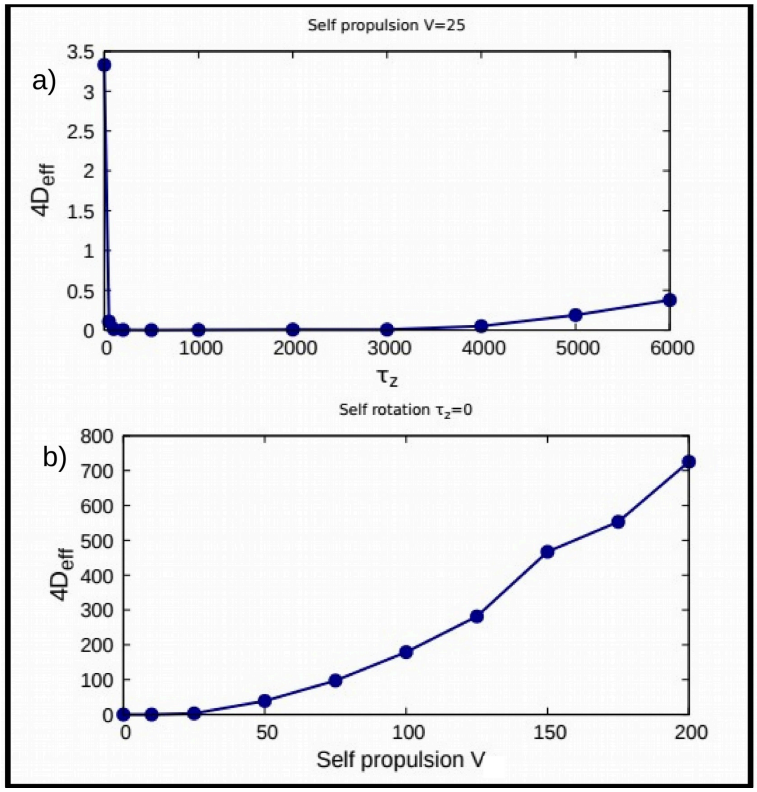

Figure 2.8: Effective diffusion coefficient (a) Effective diffusion constant D_{eff} as a function of the active torque τ_z at constant self-propulsion $V = 25$. (b) D_{eff} as a function of the self-propulsion V with no self-rotation ($\tau_z = 0$). All the quantities are dimensionless as explained in Section 2.2.2.

observations, we built and simulate a model of 2D active disks, that have the ability to self-rotate and interact with each other. We found that in the low density limit ($\phi = 0.14$) and in presence of an adhesion term among the disks, the active rotators tend to aggregate and form rotating clusters, in analogy with what is observed in algae. Similar rotating clusters were observed in confined cellular assemblies in vitro [92] and in glandular tissues [98], as well as in previous simulations of a model of self-propelled particles [57]. In particular, we saw that the adhesion term plays a crucial role in the formation of clusters, suggesting that a form of attraction should also be present in the case of *C. reinhardtii*. A possible explanation could rely on the inclusion of hydrodynamic interactions among particles (not considered in our model), that could induce effective short ranged interactions among algae. Nevertheless, this effective attractive interaction can origin from multiple biological and physical aspects of the complex system of algae in a suspension, and the investigation of its nature is beyond the scope of this study. An interesting feature of the clusters is that they rotate collectively, but also show internal particle rotations that are not always synchronized with the global rotation of the cluster. A similar behaviour is observed in *C. reinhardtii* and also in previous studies on 2D active spinners embedded in passive colloidal monolayers [2]. In the latter case, the presence of a passive monolayer that behaves elastically as a solid-like material, induces an attractive interaction between the active rotating particles, which results in aggrega-

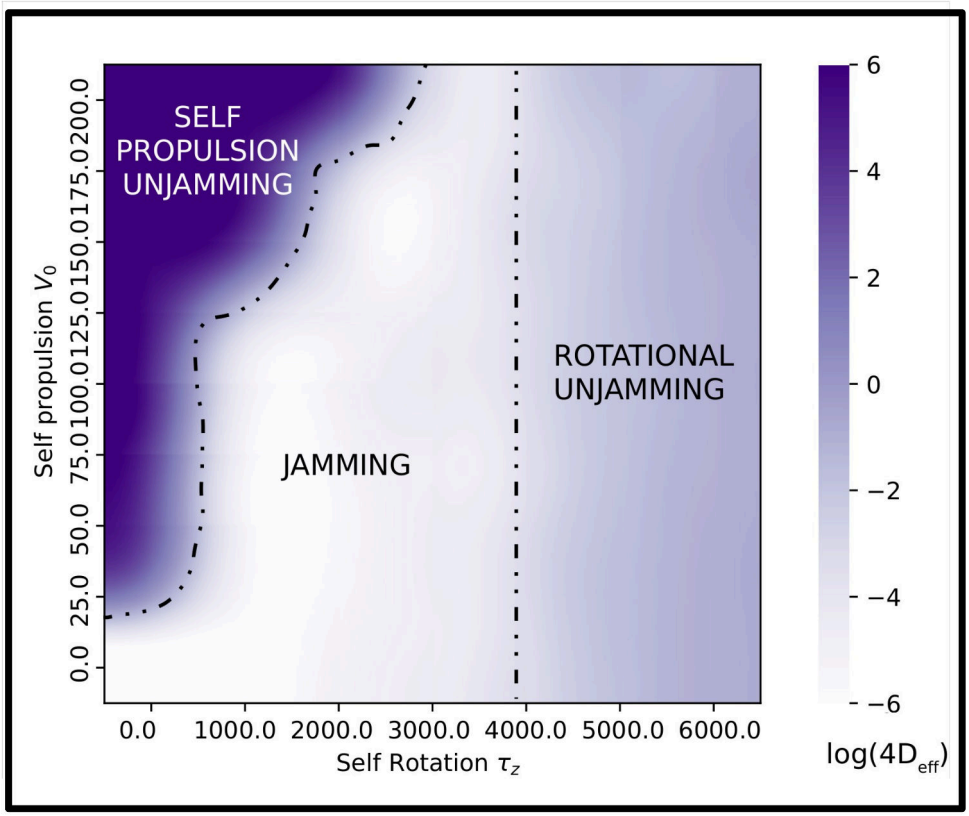

Figure 2.9: Phase diagram for active rotators A qualitative phase diagram can be obtained by plotting $\log D_{eff}$ as a function of V and τ_z. Notice the peculiar role of the self-rotation that can both induce jamming and unjamming, depending on the presence of self-propulsion. The color plot is obtained by interpolating the estimated values of $\log D_{eff}$. All the quantities are dimensionless as explained in Section 2.2.2.

tion of spinners [2]. We also mention here another related experiment, where an active granular material composed of spinning disks is confined within a circular area [107]. The authors revealed an interesting transition in the collective circulation of the spinning disks [107]. Furthermore, we studied with our simulations the role of self-rotation in a jammed system. We observed that self- rotation alone can lead to a crossover, from a jammed solid-like state to an unjammed, flowing phase. In the past, the role of active forces has been investigated, studying both 2D soft disks and active dumbell systems with different packing fraction and Péclet number [20]. The phase diagram of 2D soft disks exhibits a liquid phase with giant number fluctuations at low packing fraction ϕ and high self- propulsion V and a jammed phase at high ϕ and low V [42]. These studies, however, did not consider self-rotations as we did. We also studied the effect of adhesion and investigated its role when combined to the self-rotation of the disks. We revealed how adhesion can act in the opposite direction with respect to self-rotation, promoting jamming. Increasing the adhesion strength, we can move the system from a flowing unjammed phase to a jammed one. It would be interesting to observe a similar phase transition in experiments controlling self-rotation and adhesion, for instance

in chiral active fluids made of super-paramagnetic particles in a magnetic field [2]. A better characterization of the key features of this jamming- unjamming transition in active particles systems could be very useful to deeper understand biological processes in which the involved cells have the ability to self-rotate, both at a single particle level or as collective rotation. For example, experiments involving epithelial cells confined in narrow channels showed the formation of vorticity, suggesting a possible role for rotations in collective cell migration [103]. Another context in which the mechanical properties of tissues gain a peculiar interest is in the study of cancer cells, and in particular in the formation of metastasis. It has been observed that cancer cells are softer than non-cancerous ones [73], divide more often than healthy cells and, as in the case of the epithelial-to mesenchymal transition (EMT), they decrease the cell–cell adhesion, potentially allowing for rotational motion. All those features contribute to fluidize a confluent tissue of cancer cells, favouring the unjamming transition and so the formation of diffusing groups of cells (for a review see ref. [54]). Hence, our theoretical study of a model system of active rotators reveals how self-rotation of the active particles is a parameter that can control the jamming–unjamming transition, besides already well studied mechanisms such as self-propulsion [42] or density. This could hopefully help in better understanding physical aspects of cancer cell invasion [53].

CHAPTER 3

Active matter invasion in narrow channels

3.1 Introduction

Having investigated the role of self-rotation and adhesion in active matter systems at the jammed-unjammed transition (see Chapter 2), we want to move a step further. In particular we want to study what happens when interacting active particles are in the vicinity of a narrow channel, to understand if and how they invade it. This work, again, is inspired by the observation of biological phenomena: cells filling a void left by a wound during an healing process, or cancer cells that detach from a solid tumour and invade small blood vessels forming metastasis. Because of this close connection with well studied, but not yet fully understood biological issues, and because of the growing interest of physicists in active matter that has emerged in last years, the topic of active matter invasion has been the subject of some recent computational and theoretical works. In 2019 Felix Kempf et al. [48] studied active matter invasion, using a continuum model that describes a two-phase system consisting of an isotropic fluid phase and an active nematic phase. Such description of active matter accounts for hydrodynamics, orientational effects, and growth. The latter plays a role in biological systems such as cell monolayers or bacterial colonies. Using this approach, they simulate active matter invading capillaries and, interestingly, they observed that particle activity controls not only how deep active matter penetrates in the narrow channel, but also how the invasion takes place. They found three different regimes. When the activity is low the interface between active matter and isotropic fluid in the channel is flat and advances steadily in the channel. At intermediate activity the surface starts to deform and, for high activity, clusters of active material detach from the main body of the active phase and protrude deeper in the channel [48]. Another recent work by Adam Wysocki et al. showed that active matter can rise in thin tubes or invade a porous matrix against gravity, in analogy with classical capillarity in attractive fluids [108]. This fact is non trivial, since capillarity usually emerges as a consequence of attractive interactions between liquid particles and a wall or among liquid particles themselves. In the study, nevertheless, they used a lattice model of scalar active matter (Active Lattice Gas) with only repulsive interactions. The observation of a capillary behaviour is explained with the active particles slowing down due to the collisions, responsible also for wall accumulation, that acts as an effective attraction [108]. Nevertheless, those results, obtained solving hydrodynamic equations, do not consider individual particles and therefore it is not possible to study phenomena acting at the single particle level. This is the case of the investigation of the role of specific inter-particles potential in interacting active matter systems. In 2021 Debarati Sarkar et al. [90] showed, using a model of ABPs with attraction (simulated using a Lennard-Jones potential with a wider attractive basin), the coexistence of a bulk of active particles in the liquid phase with vacuum outside (no active particles detaching), in analogy to what is observed in

monolayered cell colonies. They derived an interesting phase diagram depending on particle activity and attractive interaction, showing a variety of behaviours from jamming to fluid-vacuum cohexistence, from cluster detachment to MIPS [90]. Inspired by those recent works, we apply our single particle model for interacting active particles described in Chapter 2 to study the invasion properties of active particles when they are in contact with a narrow channel in 2D. The aim is to characterize how few parameters such as self-propulsion strength and inter-particle adhesion can influence the way active particles invade. To do this, we run MD simulations starting from jammed configurations and spanning the parameters space. In contrast to what previously done for rotators, in this case the rotation of particles is not due to an active torque but it emerges as a consequence of the particle-particle interaction. This choice is motivated by experiments on living cells in confined environments, such as epithelial cell sheets under geometrical constraints that force cells in channel of different width [103] or Madin-Darby canine kidney (MDCK) cells confined in circular micropatterns [92]. In both cases, the formation of vortexes and collective cell rotation arise from the interaction with the environment and from cell-cell interaction. For this reason, we do not consider active rotation. With those assumptions, we obtain a qualitative phase diagram that describes different invasion behaviour for active matter (such as cluster formation or full-channel invasion) according to the values of two key parameters: the self-propulsion strength of the active particles and the intensity of the adhesion force acting among them.

3.2 Materials and Methods

3.2.1 Simulations

We perform Molecular Dynamics simulations of a system made of interacting self-propelled particles that invade a region of space characterized by the presence of a narrow channel using LAMMPS (Large-scale Atomic/Molecular Massively Parallel Simulator)[100]. In the following paragraph, we describe the model and the detailed procedures used for the simulations.

Modelling active particles

To study the invasion properties of active particles, we used the model for 2D active disks extensively described in Chapter 2. The model is based on the well studied ABPs model, to which we added two interaction terms: a contact interaction based on the Hertzian model [8], that includes friction , and an adhesion term based on the Derjaguin-Muller-Toporov model [23] [5] acting like a spring when two particles overlap. The only difference to the model described in Chapter 2 is that the self-rotation term is not included in the model, namely no active torque is injected in the system. This means that particles can rotate due to interaction with their neighbours, but they are not forced to continuously rotate. The equation of motion describing the center of mass position $\boldsymbol{x}_i(t)$ of the two dimensional disk i at time t is the same of Eq. 2.1, while the equation for the rotational angle $\theta_i(t)$ is equal to Eq. 2.2, where the term $\tau_z^i(t)$ is deleted. All the quantities are dimensionless because units are set to Lennard-Jones units in LAMMPS. Integrating the Equations of motion it is possible to update positions and velocities of the particles at each time step of our simulation.

Obtaining initial configurations

Our focus is on the role that an open channel can exert in particular on a jammed systems of active particles, inspired by wound healing experiments [17] and by biological processes such as metastasis detaching from a solid tumour and invading a blood vessel. For this reason, we want to start our simulations from initial configurations in the jammed phase. To reach this goal we started from a random distribution of 1000 bidisperse particles (500 with radius $R_1 = 1.96$ and 500 with radius $R_2 = 1.4$ in LJ units) in a square box with size $L = 300$, and then we iteratively performed 10^4 steps of continuous box reduction followed by $5 \cdot 10^4$ steps of energy minimization until the system reaches a packing fraction of $\phi = 0.87$. This value (as explained in detail in Chapter 2) has been chosen monitoring the value of the pressure and ensures that the system is in a jammed phase. The initial configurations obtained in this way have a size $L = 102$. To improve the statistics, we built 10 different initial configurations obtained starting from different random positions of the particles.

Building the channel

Once that we have our different initial jammed configurations, we double the length of our simulation box to obtain a rectangle of size $L \times 2L$. The new region of space obtained in this way is filled with particles of radius $R = 1.4$ in a square lattice with Lennard-Jones reduced density 0.15. But the space added to the simulation box is not entirely filled with particles, a narrow channel of width d is left free.

The particles that constitute the channel sides have the same mass and radius of the invading particles, but they are excluded from the systems dynamics via the LAMMPS command `fix freeze`, that zeroes out the forces and torques on the selected granular particles. Furthermore, the channel particles interact with the invading active particles via an Hertzian potential with the same parameters used for the inter-particle interaction (for detailed values see Tab. 2.1 in Chapter 2). The adhesive term, instead, is not present in the interaction with the channel walls. Finally, to complete the simulation setup, we close the box boundaries so that the active particles cannot escape. Two fixed particles have been placed in the low right and low left corners, to avoid particle escaping from the box corners. The close boundaries interact with the active particles always via an Hertzian potential. In this way, the invading active particles that reach the end of the channel are repelled by the fixed box boundary. We performed preliminary tests with different channel widths, in particular $d = 6$, $d = 12$ and $d = 16$. When not specified, the results described in the following paragraphs have been obtained for $d = 12$, that allows the simultaneous passage of 3 to 4 particles.

Parameters used for the simulations

For the simulations we used 2D disks of radius $R_1 = 1.96$ and $R_2 = 1.4$ and density of the disk $d = 0.46$ (for which the mass is $m = d \cdot \pi R^2$). The parameters used for the Hertzian potential and for the DMT adhesion are the same already described in Tab. 2.1 Chapter 2. The temperature is constant during the integration of the equation of motion and equal to $T = 1$. The time step is of 0.0001 in LJ units. Since we are interested in the study of the invasion process, the idea was to set the simulations time so that complete channel invasion can be observed. Nevertheless, since we are varying as a parameter the particle self-propulsion strength V, we should expect that more active particles reach the end of the channel sooner respect to slowest ones. For this reason, we run simulations

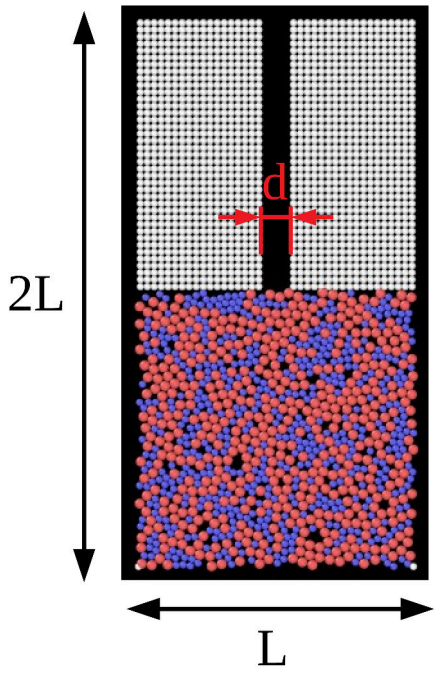

Figure 3.1: Scheme of the simulated channel Snapshot obtained with Ovito [97] of the simulation box. The jammed active particles are showed in blue and red and the channel of width d is clearly visible.

for $3 \cdot 10^7$ steps (covering 1000 time units) in the high self-propulsion regime and for $3 \cdot 10^8$ steps (covering 10000 time units) in the low self-propulsion regime.

3.3 Results

3.3.1 Qualitative results

We performed simulations for different values of particle self-propulsion V and adhesion strength A_{cc} and observed using OVITO [97] what happens in the channel region. These qualitative results are illustrated in the following paragraph.

Different kind of invasion

From the observation of invasion snapshots, we notice that not all the invasion processes looked the same. It is clear from Figure 3.2 that two different behaviours appears: invasion performed by single particles (resembling the invasion of a fluid) and cluster invasion, in which groups of active particles detach from the bulk and flow in the channel. As expected, the formation of invading clusters is due to higher values of the particle-particle adhesion strength A_{cc}. The snapshot in the left panel of Figure 3.2 is obtained for $A_{cc} = 3$ while the one on the right panel that displays cluster formation is obtained for $A_{cc} = 1000$. This fact will be taken into account in the interpretation of the quantitative results obtained in the following paragraphs.

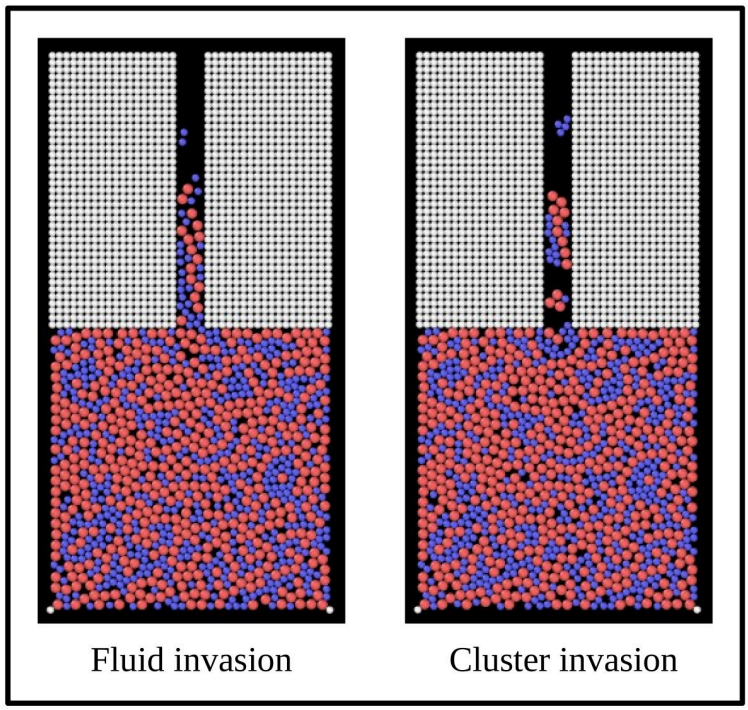

Figure 3.2: Examples of different invasions Snapshots at $t = 10$ time units obtained for particle self-propulsion $V = 300$ and adhesion $A_{cc} = 3$ (left) and $A_{cc} = 1000$ (right) respectively. It can be observed as an higher value of adhesion promotes the formation of clusters that detach from the jammed bulk of active particles and invade the channel.

The role of rotation

An interesting issue to be considered is the role that particle rotation plays in the invasion process. As already mentioned in the Material and Methods section, no active torque, namely no self-rotation is added to our active particles. Nevertheless they can acquire non zero angular velocity through interaction with neighbours. To underline particle rotation, we coloured the simulated active particles according to their angular velocity along the $\widehat{\boldsymbol{z}}$ direction (our 2D system lies on the xy plane). The majority of particles show low angular velocity, and often the presence of rotation is localized and transient, associated with local rearrangements. Interestingly, we notice that the particles located close to the channel opening just before the beginning of the invasion process display significant angular velocity, rotating much more than the active particles in the bulk. This fact can be appreciated in Figure 3.3, for different values of inter-particle adhesion. Those particles, due to the presence of an opening, are able to move more than the particles in the bulk, that are in a dynamically arrested state because of the high density of surrounding neighbours. It is interesting to underline that the rotational degrees of freedom in a system of interacting frictional active particles play a role in fluidizing the system, allowing the onset of channel invasion.

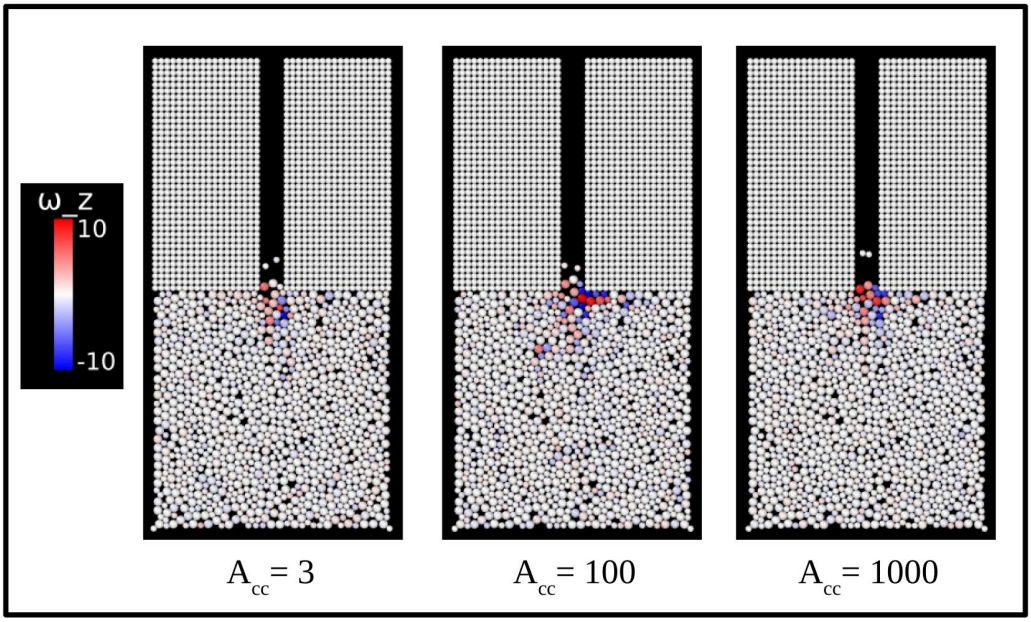

Figure 3.3: Pre-invasion snapshots Snapshots obtained for self-propulsion $V = 150$ and adhesion strength $A_{cc} = 3$, $A_{cc} = 100$ and $A_{cc} = 1000$ respectively. The time at which the snapshots have been acquired is different for each of the three cases and it precedes the beginning of channel invasion, with particles that detach from the bulk. Particles coloured in blue rotates clockwise while particles coloured in red rotates counter-clockwise.

3.3.2 Analysis of the invasion curves

To study in detail and in a more quantitative way the invasion behaviour of our active particles system, we scanned the parameters space with simulations at different self-propulsion V and adhesion A_{cc} and computed proper invasion curves for each case. Inside the channel of length L, we set a threshold corresponding to $L/4$; if a particle exceeds this threshold it is counted as an invading particle. The choice of setting a threshold for channel invasion was made to avoid counting particles that move to the beginning of the channel opening only as a consequence of small rearrangements of the initial configurations. The invasion curves are obtained plotting the number of invading particles present in the channel at each timestep of the simulation. In Figures 3.4 and 3.5 examples of such curves are showed. More in detail, in Figure 3.4, the growing part of the curve is associated with a channel invasion reminiscent of a fluid invasion; the equilibrium is reached when the channel is completely filled. Even more interestingly, in Figure 3.5 the first part of the curve, characterized by discrete oscillations, is associated with the presence of invading clusters of active particles. It is thus clear how the inspection of those invasion curves allows us to understand the invasion process.

We computed the invasion curves for each set of parameters ($V = \{1.5, 15, 150, 300, 450\}$ and $A_{cc} = \{0.0, 3, 30, 100, 300, 600, 1000, 1300, 1500, 2000, 3000, 5000, 7000, 9000, 11000\}$) and for each initial configuration. Then we averaged the invasion curves over the 10 different initial configurations, to reduce the influence of the initial particles positions on the invasion process. It has to be noticed that a different number of timesteps have been employed in simulations with different values of self propulsion, since faster par-

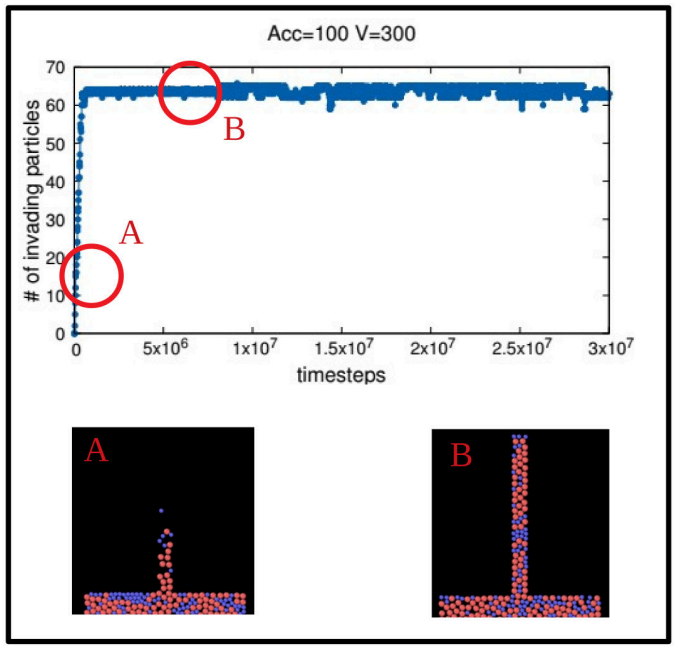

Figure 3.4: Example of invasion curve Invasion curve for self-propulsion $V = 300$ and adhesion $A_{cc} = 100$. The invasion curve shows a rapid growth toward an equilibrium value. The snapshot in A shows what happens at the beginning of the invasion curve: the active particles are invading the channel and their number consequently increases with time. In snapshot B the equilibrium condition is illustrated: the channel is completely filled and the number of invading particles remains constant.

ticles fill the channel faster than slower ones. For simplicity, we divided the simulations in two categories, low velocity ones ($V = \{1.5, 15\}$) that we run for $3 \cdot 10^8$ timesteps and high velocity ones ($V = \{150, 300, 450\}$), that we run for $3 \cdot 10^7$ timesteps. Those selected times do not guarantee the reaching of equilibrium in all the considered cases, since, especially for high adhesion, the channel is far from being completely filled. Yet in those time scales the invasion behaviour driven by particle activity, rather than simple diffusive behaviour, can emerge in a clear way. In Figure 3.6, the averaged invasion curves in the high velocity regime ($V = 150$) are showed for different values of the adhesion. When the adhesion is low, the invasion is dominated by single particles that flow in the channel like a liquid, until they completely fill it (equilibrium condition reached at long times when # of invading particles ≈ 67). When the adhesion increases (here from $A_{cc} = 1000$ onward), the curve starts to become more jagged, showing discrete oscillations due to the formation of clusters of invading particles. In this condition, the channel is not completely filled. Increasing the adhesion, the number of invading particles decreases because detaching from the jammed bulk becomes more difficult. When the adhesion is too high, no particle can detach and invasion does not occur.

In Figure 3.7, instead, the averaged invasion curves in the low velocity regime ($V = 1.5$) are showed. Here, the self-propulsion is not enough to significantly promote full channel invasion. When the adhesion is low, only few particles detach from the bulk and then migrate in the channel mainly guided by the thermal fluctuations of the Brownian motion. Very soon, when the adhesion becomes $A_{cc} = 100$, the invasion completely

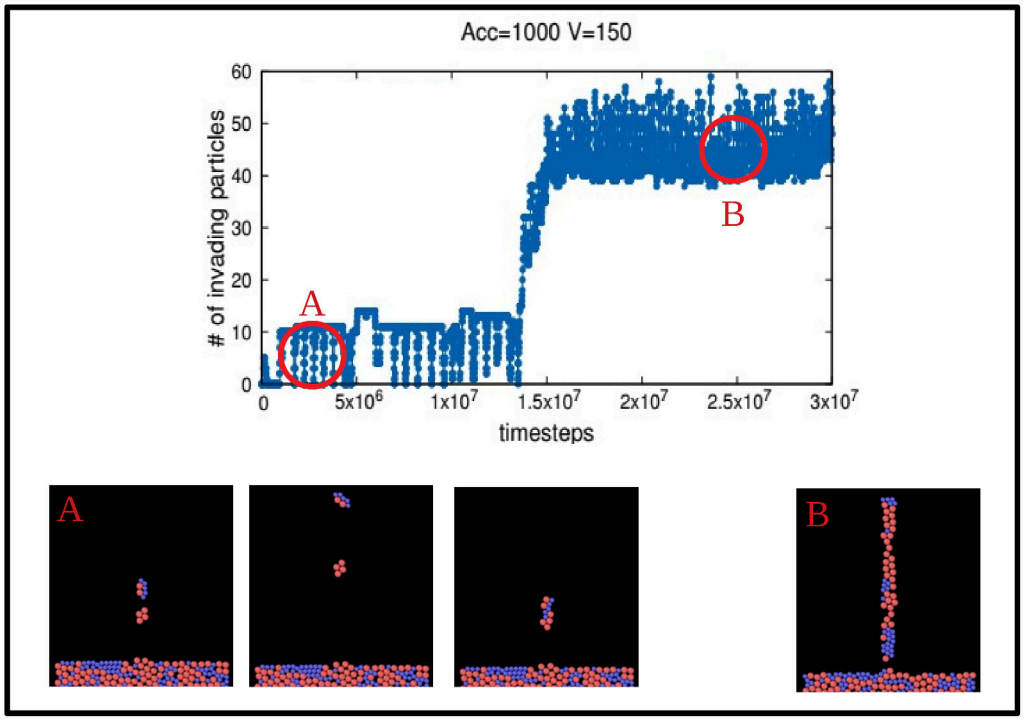

Figure 3.5: Example of invasion curve Invasion curve for self-propulsion $V = 150$ and adhesion $A_{cc} = 1000$. Looking at the curve, it oscillates around a small number of invading particles for nearly half of the time, then it grows up to higher values. Looking at the snapshots in A it is possible to understand what happens in the first part of the invasion curve: some small clusters detached from the bulk and are oscillating up and down in the channel (the end of the channel is closed, so particles bounce back). This is why the curve is so jagged. In snapshot B instead it is clear what happens in the long time region of the invasion curve: the channel is almost completely filled by a huge group of particles aggregated by the high inter-particle adhesion.

stops. Weakly active particles do not manage to unjamm the region near the channel opening, when significant adhesion is present.

To deepen our understanding of the role of adhesion in the invasion process, it is useful to show in the same plot averaged invasion curves for the same self-propulsion velocity and different adhesion, as we did in Figure 3.8. Looking at the low velocity regime (see Figure 3.8.a), the most interesting feature is that the curve for $A_{cc} = 3$ reaches higher values in term of number of invading particles with respect to the curve for $A_{cc} = 0$. This means that a small, but not null, adhesion among the particles promotes the invasion. The same trend can be observed also for particles with higher motility, see Figure 3.8.b. Also in the high velocity regime the curve for $A_{cc} = 3$ reaches the saturation (corresponding to full channel filling) sooner than the curve for $A_{cc} = 0.0$, suggesting that a small adhesion helps the invasion process. In the low velocity regime, further increase of the adhesion stops the invasion (see Fig. 3.8.a). For $V = 150$, instead, the scenario is more complicated: increasing the adhesion leads to full channel invasion at different times, sometimes earlier, sometimes later. Only for really high value of adhesion ($A_{cc} = 1000$ and $A_{cc} = 1300$) the invasion curve clearly change its shape, not reaching the complete channel fill (see Fig. 3.8.b). It has to been noticed that for the comparison

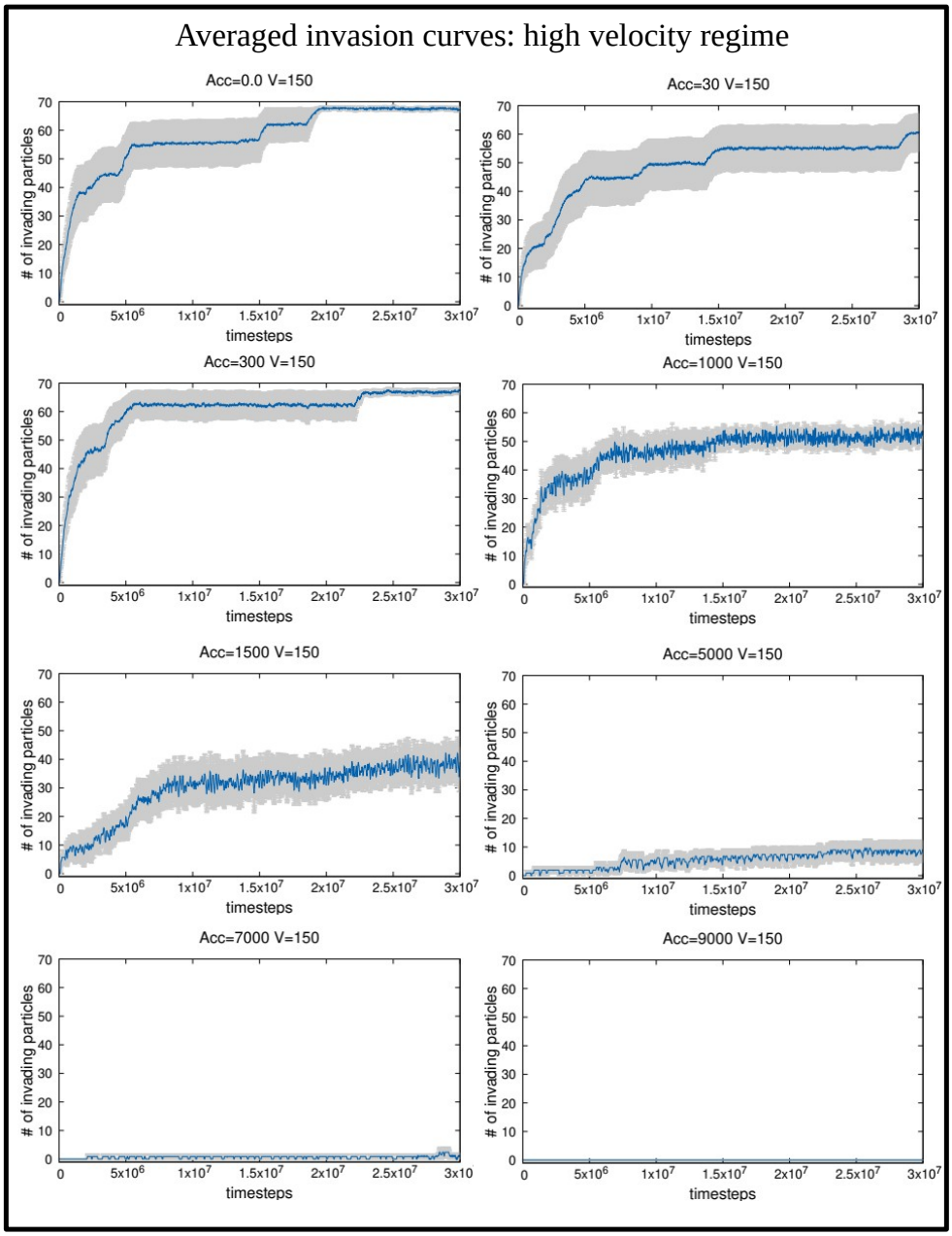

Figure 3.6: Averaged invasion curves in the high velocity regime Invasion curves for $V = 150$ and different values of adhesion. The blue line represents the invasion curve averaged over the 10 different initial configurations. Grey shadows represent the standard error.

plots in Fig. 3.8 we applied a Jackknife resampling procedure to estimate the standard error on the averaged invasion curves. This technique allowed us to estimate the error

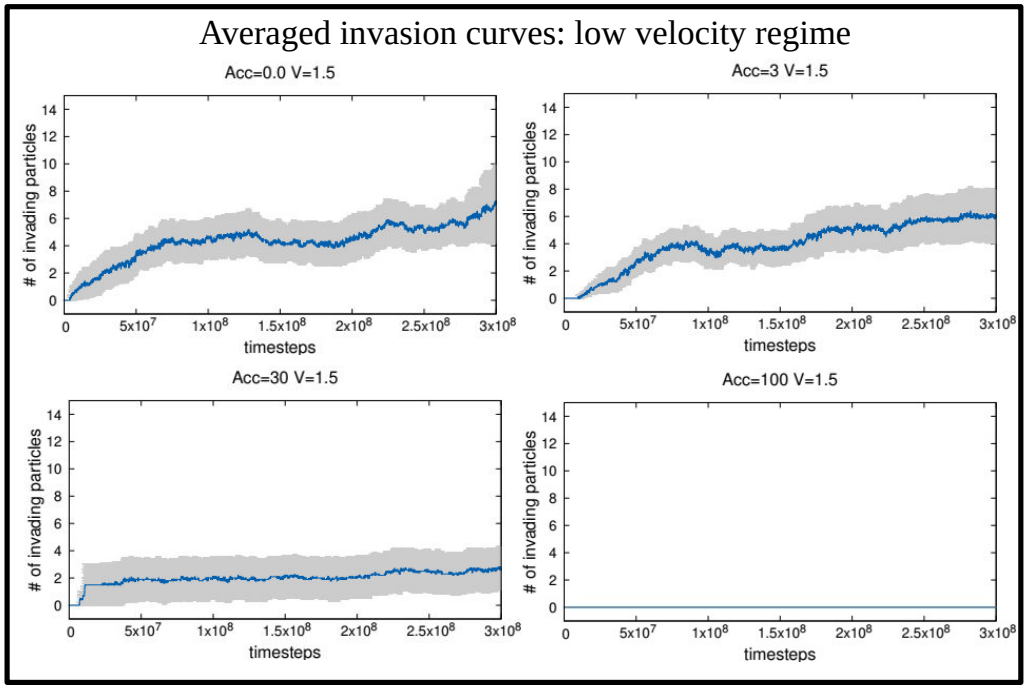

Figure 3.7: Averaged invasion curves in the low velocity regime Invasion curves for $V = 1.5$ and different values of adhesion. The blue line represents the invasion curve averaged over the 10 different initial configurations. Grey shadows represents the standard error.

on the averaged curves using the values of the averages obtained leaving out an initial configuration at a time from the 10 we considered. Jackknife analysis have been performed using the python function `astropy.stats.jackknife` [3] and the obtained standard errors are represented as shadows in Fig. 3.8.

Phase diagram for invading active matter

We used the invasion curves to characterize the different ways in which active particles can invade the narrow channel. The aim is to build a diagram that defines the invasion properties according to the two key parameters we are considering: particle activity V and inter-particle adhesion A_{cc}. We performed a fit of the invasion curves with the following non linear function:

$$f(t) = \alpha \cdot [1 - \exp(-\frac{t}{\tau})] \tag{3.1}$$

For $t \to +\infty$ the function converges to the parameter α, that represents the number of particles in the channel at the end of the simulations. When the saturation is reached, it represents the number of particles that completely fill the channel. The parameter τ describes the characteristic time of the channel invasion process. A large value of τ means that the active particles need a long time to invade the channel, while a low value of τ indicates high effectiveness of the invasion process. In this way, the quantity

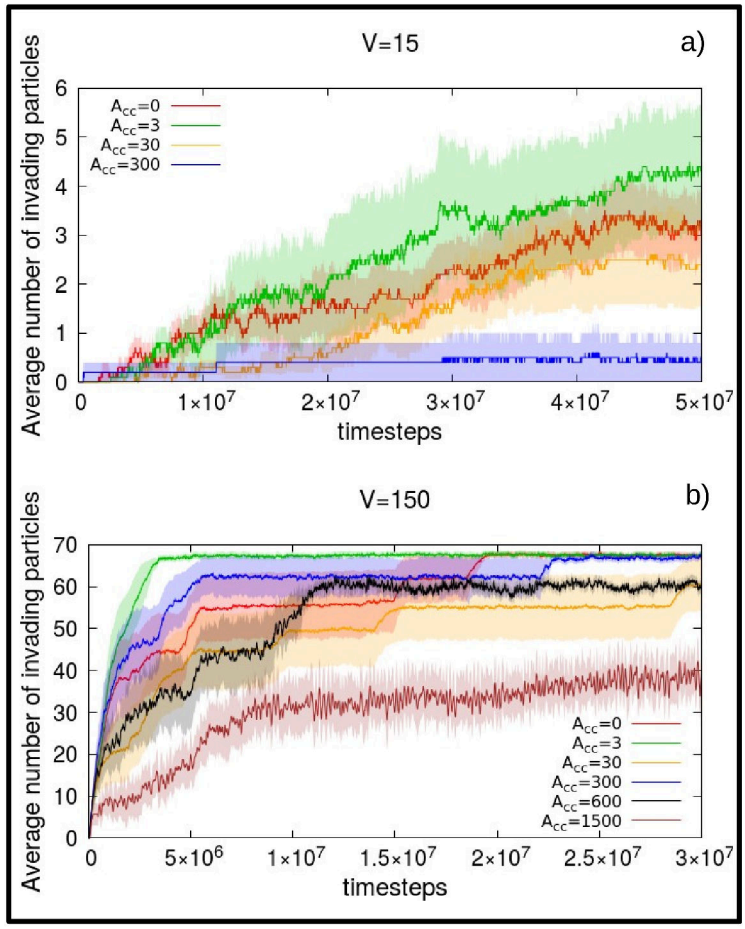

Figure 3.8: Averaged invasion curves for same self-propulsion and different adhesion (a) Invasion curves averaged on 10 initial configurations for self-propulsion $V = 15$ and different values of adhesion A_{cc}. It should be noted that the curve for $A_{cc} = 3$ (green) at a certain point overlaps the curve for $A_{cc} = 0.0$ (red), suggesting that a small but non null adhesion promotes the invasion. Then further increasing the adhesion the invasion curves goes to zero. The anomalous behaviour of the curve for $A_{cc} = 300$ could be due to statistical fluctuations. (b)Invasion curves averaged on 10 initial configurations for self-propulsion $V = 150$ and different values of adhesion A_{cc}. Again the invasion is promoted by a small but non null adhesion, in facts the curve for $A_{cc} = 3$ (green) reaches the equilibrium very fast, much before the curve for $A_{cc} = 0.0$ (red). From $A_{cc} = 600$ onwards the invasion curves start to be jagged, showing evidence of cluster formation and do not reach any more the full channel condition. Both in (a) and (b) the shadows represent the standard error computed with a Jackknife resampling procedure applied on the 10 different initial configurations.

$R = \frac{1}{\tau}$ defines the invasion rate (measured in $[time^{-1}]$ units) for the active particles in the channel. In Figure 3.9, we plotted the quantity R obtained from the fits of the invasion curves as a function of the adhesion A_{cc} for different values of the self-propulsion V. The curves for $V = 150$, $V = 300$ and $V = 450$ clearly show a decrease associated with the increase of the adhesion, meaning that in this context, inter-particle cohesion hinders

invasion. Nevertheless, an exception to this trend is found in the low adhesion limit. Here the peaks of the curves are not in correspondence to $A_{cc} = 0$, but they are found for low but non null adhesion. This means that, in our system of interacting active particles, a small inter-particle adhesion favours the invasion process with respect to no adhesion at all. The curves for $V = 1.5$ and $V = 15$ show a different behaviour: they are very close to zero, meaning that the invasion rate is almost null. In this low velocity limit, an extremely long time is needed for channel invasion, since the process is dominated by thermal fluctuations and the probability of a particle detaching from the bulk and performing invasion is low.

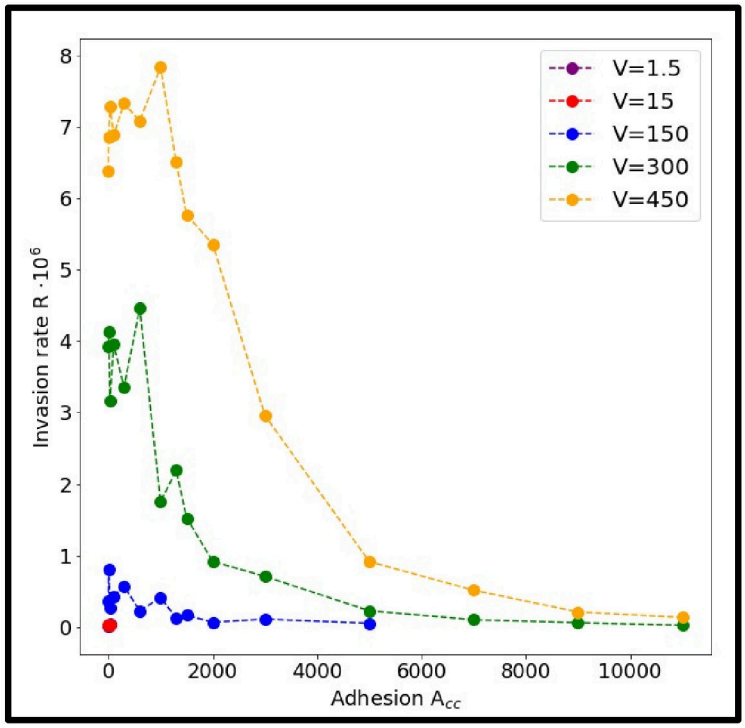

Figure 3.9: Plot of invasion rate as a function of the adhesion strength Curves of the invasion rate R as a function of the inter-particle adhesion A_{cc} for different values of the self-propulsion V.

Putting together the information coming from the fits, we build a phase diagram that has on the x axis the self-propulsion V, on the y axis the adhesion A_{cc} and in which the regions of space are coloured according to the values of the invasion rate R. The result is illustrated in Figure 3.10, where the axis and the colorbar are in logarithmic scale. For low adhesion and low activity of the invading particles, the invasion rate is close to zero, and no invasion occurs (light blue region). Instead, for high self-propulsion V the invasion rate is high for a huge range of adhesion values (dark blue region). In this region, that we named of fluid invasion, particles flow in the channel like a fluid, completely filling the channel in relatively short times. An intermediate region in terms of invasion rate appears (blue region) for high values of adhesion, when the motility is high or even for low adhesion for intermediate values of the particle activity. In this region, as we can show from the analysis of the invasion curves shapes (jagged or not) and from the ob-

servation of particles configurations, the invasion is dominated by clusters of invading active particles.

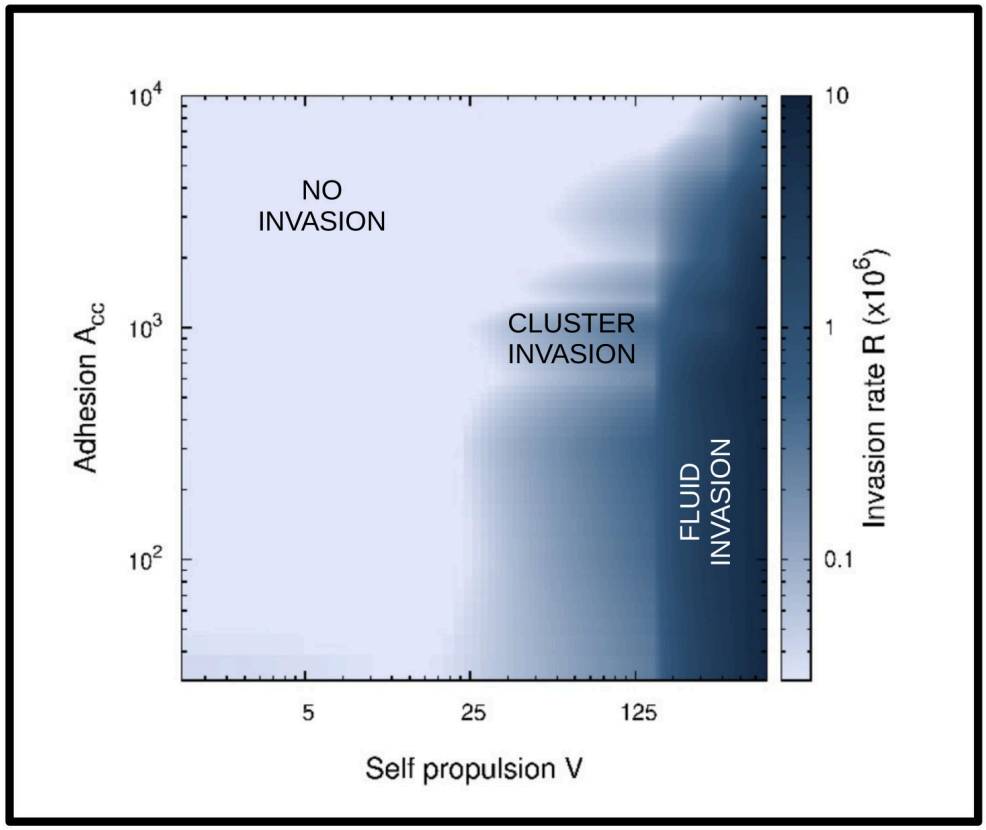

Figure 3.10: Qualitative phase diagram for invading active particles A qualitative phase diagram can be obtained by plotting the invasion rate R as a function of self-propulsion V and adhesion A_{cc}. Two region are clearly visible: one in which practically no invasion occurs (light blue) and one in which active particles invade the channel like a fluid (dark blue). An additional intermediate region dominated by cluster invasion appears in blue. The color plot is obtained by interpolating the values of R. Axis and colorbar are in logarithmic scale.

3.4 Discussion and Conclusions

Applying our model, based on ABPs, to the study of interacting active matter invading narrow channels, we can investigate the role of single particle properties in determining the invasion behaviour. In particular, we hypothesized an Hertzian interaction that includes friction among active particles and a specific adhesion term (described via the DMT model). We reported different invasion modes, according to adhesion strength and particle self-propulsion. Previous work using a continuous hydrodynamic model to describe growing active matter, found three different invasion modes progressively increasing particles activity: mode I, characterized by a flat interface between invading

active matter and the isotropic fluid that fills the channel, mode II, with an S-shaped interface and mode III, where clusters of active matter detach from the bulk, overcoming surface tension, and migrate in the channel. Interestingly, the authors reported that clusters penetrate deeper in the channel, even if they have no influence on the total amount of active material that invades the capillary [48]. Our system has some substantial differences with the previous model:

- we are explicitly adding an adhesion term;
- we start our simulations from a jammed phase;
- we are not accounting for growth (the number of particles is kept constant).

Keeping in mind those differences, we also observed three different invasion behaviours:

- no invasion, when particles activity is too low to unjam the system and particles are mainly driven by thermal fluctuations, or when adhesion is very high and prevents particles to detach from the bulk;
- fluid invasion, when the self-propulsion is high and adhesion is low;
- cluster invasion, when the adhesion is quite high and groups of particles detach from the jammed bulk.

Those regimes could be appreciated both from the direct observation of the invasion curves (see Fig. 3.6,Fig. 3.7 and Fig. 3.8) and from the phase diagram in Fig. 3.10, built using the penetration rate R and inspired by results obtained for attractive ABPs in free space [90]. The formation of clusters of invading particles is of particular interest for the connection with biological problems. In tumours, the metastatic process starts from group of cancer cells that detach from the primary site. In this context, it has been observed that changes in proliferation and cell death which increase the rate at which cells migrate, promote tumour growth [29]. The fact that we could define different invasion modes by controlling just two parameters, the particles self-propulsion and the inter-particle adhesion, could be extremely interesting when comparing with experiments. Previous experiments on cancer cells, performed in vivo and in vitro, revealed that jamming-unjamming transitions between jammed solid, active fluid and active nematic phases (described by measuring fluctuations in the velocity and vorticity) could be tuned by controlling the density and the adhesion[43]. Furthermore, cells that perform the epithelial–mesenchymal transition (EMT) (going from polarized epithelial state (E), to mesenchymal (M) state in which they are able to migrate), can induce a jamming-unjamming phase transition through the reduction of cell–cell adhesion [55]. This fact suggests the key role of adhesion strength in determining the phase behaviour of a system of cells. Another interesting qualitative result we obtained from our simulations, is the high rotation of particles located near the channel just before the invasion start. This fact confirms the role of rotational degrees of freedom in unjamming the system [82]. A recent computational study that uses single particle model (Cellular Potts Model) for studying active matter invasion in a narrowing channel, revealed accumulation and reflux of cells near the channel bottleneck (particles moving backwards) [47]. This suggests that in this pre-channel regions, collective particles rotation could play a role and is favoured by the peculiar boundary conditions. The investigation of the role of rotation at the beginning of the invasion process deserve further quantitative analysis.

Part II
Nuclear Pores

CHAPTER 4

Nuclear Pores

4.1 What is a Nuclear Pore

In eukaryotic cells, genetic information is well protected inside the cell nucleus, divided by the outside cytoplasm by a lipid bilayer membrane called nuclear envelope (NE), the most prominent nuclear scaffold. This segregation has the great advantage of protecting the genome from external sources of damage. On the other hand, communications based on exchange of macro-molecules, such as messenger RNAs (mRNA) or transcriptomic factors, are of vital importance during all the cell life cycle, to control protein synthesis and instruct gene expression [49, 85]. Nuclear pore complexes (NPCs), vast protein assemblies embedded in the nuclear envelope, play this crucial role. NPCs control the bidirectional transport of proteins and ribonucleoparticles and act as unique gateways for molecular exchange between the cell nucleus and the cytoplasm [49], [35].

4.1.1 Structure

Since the discovery of nuclear pores in the 1950s, considerable effort has been devoted to determine and understand their rich and peculiar structure. In particular, much of our current understanding on this topic comes from microscopy studies of *Xenopus laevis* (a frog) oocyte NPCs, using a variety of electron microscopy techniques and sample preparations. The choiche of *Xenopus l.* oocytes as popular model system for experimental studies on NPCs, is due to practical reasons. Each oocyte has a very large nucleus (about $0.4mm$ in diameter), that is easy to isolate and manipulate manually. It contains a high density of NPCs($50NPC/\mu m^2$) and the dimensions of its NPCs (a diameter of $110nm$ and an height of $70nm$) are almost the same of human ones [49]. This allowed experimentalists to obtain good images and catch important features of NPCs with this technique [75]. More recently (from 2003 onwards), cryo–electron tomography (cryo-ET) and subtomogram averaging have been utilized to generate 3D reconstructions of intact NPCs in different species, deepening our understanding of their structure [61]. As can be seen in Figure 4.1 b), the NPCs appear at a first glance as small "holes" on the nuclear envelope, enclosed by a protein scaffold. It was already clear from early observations, that nuclear pores were modular assemblies, composed by discrete constituents arranged with octagonal symmetry around a central axis [102], [83]. Later on, those discrete elements have been identified with multiple copies of about 34 protein subunits (called nucleoporins), organized in a small number of biochemically defined subcomplexes that work as building blocks to create the huge structure of the NPC. Very interestingly, those building blocks are well conserved throughout eukaryotes, showing similar features in algae, yeast, vertebrates such as *Xenopus Laevis* up to human, underlying the evolutionary relevance of NPCs for the life as we know it. In more details, as can be observed

in the scheme of Figure 4.1 c), the characteristic shape of a nuclear pore consists of two superimposed rings of nucleoporins, with well defined eightfold symmetry, one placed on the outer face of the nuclear membrane and one on the inner face. Eight extended filaments depart from each ring spreading in the cytoplasm and in the nucleoplasm respectively. The center of the pore (a central channel with diameter $40nm$), instead, is filled with disordered filaments of phenylanine-glycine repeats(FG), forming the properly permeability barrier [49] [61]. In the following work, keeping temporarily aside all the complex biology of NPCs, we will focus on their peculiar geometrical shape, trying to investigate the physical implications of the eight-fold symmetry of those protein assemblies.

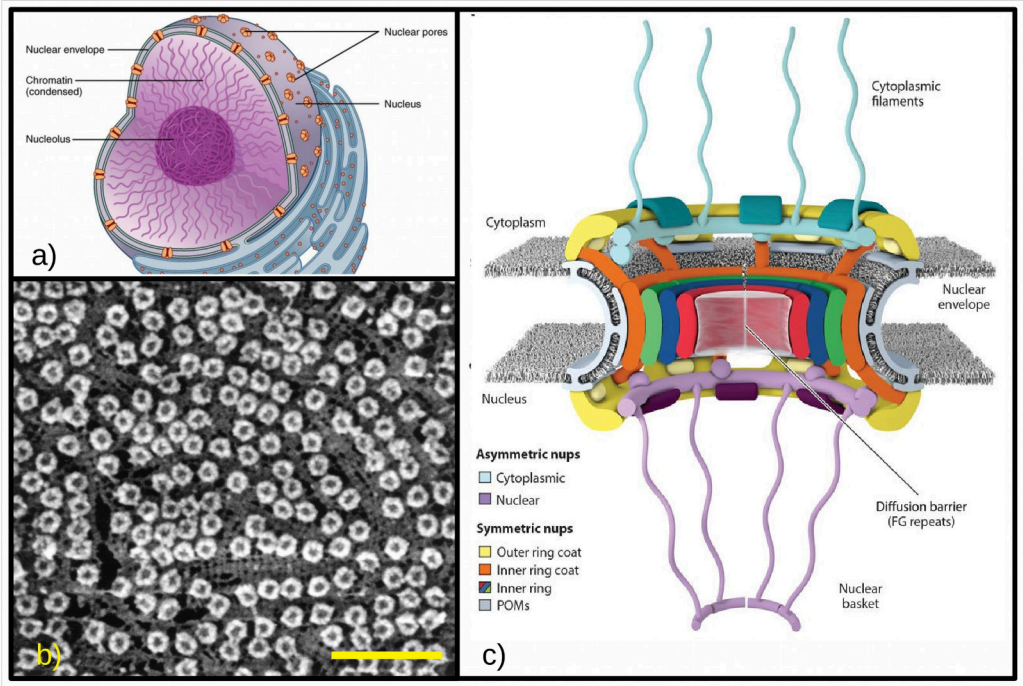

Figure 4.1: Schemes and images of NPCs location and structure (a) Scheme of the nucleus of an eukaryotic cell. The inner part containing the genetic material (chromatin is clearly visible) is divided from the outside cytoplasm by the nuclear envelope (NE); inserted on it, nuclear pores are clearly visible; (b) portions of experimental images of several nuclear pores in *Xenopus laevis* oocyte obtained using high-resolution field-emission scanning electron microscopy. Scalebar is $0.5\mu m$; (c) vertical section of a nuclear pore, illustrating in a schematic way its inner structure. Panel (b) is an adaptation from Hans Ris [85] Copyright 1997 with permission of Foundation for Advances in Medicine and Science, Inc. , panel (c) is an adaptation from Daniel H. Lin et al. [61] Copyright 2019 with permission of Annual Reviews;

4.1.2 Functions

Let us now focus on the function of NPCs and on their role in the cell life cicle. As already mentioned, they are the unique gateways for communication among the nucleus and the outside cytoplasm. Nevertheless, they are not simply open holes from which everything can pass. Evolution has tuned this refined protein machineries to allow the free

diffusion of ions and small molecule (below $5nm$), for which NPC represents a freely permeable barrier, and acts as a selective gate for import and export of macromolecules, from proteins to RNAs up to viruses (e.g. capsids of the hepatitis B virus have diameters of $36nm$), eventually mediated by specific transport receptors [75] [49]. Thanks to those mechanisms, a single NPC is able to manage an intense nucleo-cytoplasmatic traffic. Kinetic studies of protein translocation through the NPC have shown that the mass flow through a single NPC is $100MDa$ per second. During cell life, NPCs are crossed by a huge amount of matter crucial for biological processes [31]. Very interestingly, even more detailed experiments on cargo transport through NPCs, have not fully revealed the details of the passage of macromolecules through the FG repeats network of filaments present in the centre of the pores. To this purpose, some reviews suggest that more mechanistic transport models (based on Brownian motion) and computational procedures to study the nucleo-cytoplasmatic transport phenomenon at the relevant length/time scales, could help in deeply understanding it. Adopting more interdisciplinary approaches could open the way to collaborations between physicists and biologists on the topic of macromolecural passage through NPCs [31] [60]. Beside managing a huge traffic of molecules, NPCs themselves are dynamic structures. The scaffold nucleoporins that form the rings are indeed very stable in time, with little to no turnover throughout the life-span of post-mitotic differentiated cells [35], as revealed by photobleaching experiments. However, other nucleoporins of which NPCs are constituted, can rearrange and adapt to cell condition. Some examples of cell-type specific NPCs have already been observed, suggesting compositional rearrangement as a widespread mechanism for adapting the functions of NPCs toward cell type-specific constraints and context-dependent needs [72]. Compositional difference between NPCs whitin one single cell is also starting to emerge [64], suggesting a very rich scenario [49]. During the cell division process, NPCs have to disassemble at the onset of mitosis (even if most of their bulding blocks, the nucleoporins, remain assembled into stable subcomplexes), and to reassemble around the newly formed nuclei of the daughter cells from anaphase onwards, in a higly dynamical process [35]. Again, the details of pore genesis are far from being fully understood, leaving open fascinating questions. Going under the surface of nuclear envelope, down inside the nucleus, it can be observed that nuclear pores are not isolated structures, but they are bound to the nuclear lamina (a meshwork of filamentous proteins, the nuclear lamins, that acts as a structural scaffold for the nucleus) and physically interacts with DNA filaments packed in chromatin structures. For this reason NPCs are involved in the organization of the genome itself (dense heterochromatin is a prominent feature of the nuclear periphery, whereas regions of less-packed euchromatin underlie NPCs) and contribute to gene regulation, promoting for example the activation of certain genes in response to stimulus and the repression of other ones [10].

4.2 Spatial Organization of Nuclear Pores on the Nuclear Envelope

Despite great progress in understanding the structure of a single nuclear pore, little is known about how nuclear pores are distributed across the surface of the nuclear membrane (in an average human cell there are approximately 2000-3000 nuclear pores) and whether and how they might interact among each other. Interactions among pores are likely modulated by the the nuclear lamina, a filamentous protein network underlying the nuclear envelope, but how exactly the interaction occurs is still unclear. Maul et. al. in 1971 were the first who questioned the assumption that the distribution of nuclear pore complexes on the nuclear envelope is random. The authors observed rat kidney cells nuclei via electron microscopy and (as can be seen in Figure 4.2 a)) computed the

distances among the detected NPCs. With those data, they built an histogram with the measured inter-pores distances and compared the distribution they obtained with the ones for random distributed point and for hexagonally arranged points (see Figure 4.2 b). The NPCs spatial distributions seems to be a sort of combination of the two, with some maxima in good accord with the hexagonally arranged points. Even if the statistic was not rich, and the incertainities due to image acquisition not so small, they could adfirm that the distribution of nuclear pores on the NE is nonrandom [67]. Few years later, in 1980, the same authors revealed that highly proliferative cells, such as embryos or tumors, have an high density of nuclear pores on the nuclear membrane, while terminal differentiated cells have fewer, suggesting a link between number and distribution of pores and cell activity [68]. This link has been explored in another early study of the same years, focused on the changes in distribution of nuclear pores during spermatogenesis in rodents, following the evolution from spermatocytes to early spermatids. In particular, a clear change in nuclear pore spatial organization, from aggregation with hexagonal packing in pore rich areas coexisting with large pore-free areas in spermatocytes (see Figure 4.2 c)), to a random distribution (see Figure 4.2 d)) of pores in early spermatids has been observed [33].

A study focused instead on the end of the cell life (on mouse cell nuclei) has shown that, even during apoptosis (programmed cell death), the distribution of nuclear pores on the cell nucleus strongly changes. The NPCs become highly concentrated in small regions of the nuclear envelope, leaving the rest of the surface pore-free, as it can be appreciated in Figure 4.3 a). Those clusters of pores showed an hexagonal packing and were supposed to be correlated with diffuse chromatine areas[32]. More recently a further step in our understanding of the role of nuclear pore spatial organization came with the observations of large pore-free islands in HeLa S3 human cells (see Figure 4.3 $b.1$)). These islands disperse with cell-cycle progression and are enriched with the inner nuclear membrane proteins lamin A/C (see the immunofluorescence image on Figure 4.3 $b.2$) and emerin, but exclude lamin B. This fact reveals the importance of lamin A/C in regulating the pore distribution, suggesting that the dynamics of nuclear pores is regulated by the reorganization of inner nuclear structures [65].

In a recent paper, Sellés et al. performed super-resolution microscopy on Xenopus laevis oocytes, to observe the variation of nuclear pore distribution on the nuclear membrane during oocyte development from early stages (see Figure 4.3 $c.1$) and $c.2$)), where the transcriptional activity is very high, to later ones (see Figure 4.3 $c.3$)), where this activity is significantly lower. From a first analysis of those experimental observations they highlighted a decrease of the density of NPC during the development process, but their analysis was not limited to pores counting. To investigate the large-scale organization of the NPCs on the nuclear envelope, they decided to calculate the angles distribution function between the first two neighbors of a given NPC. In the early stages of development, they revealed a flat distribution, with no preferential angles suggesting a disordered structure. However, proceding with oocyte development, they observed two peaks in the angle distribution function (one at $90°$ and the other at $180°$), describing pores locally arranged in square lattice structures. Furthermore, they computed the angular and radial density function $P(d, \alpha)$, describing the probability to observe on a given envelope a NPC with two neighbors at a distance d and forming an angle α. For the early stages of oocyte development, they observed a map characteristic of a 2D compact and amorphous structure of nuclear pore complexes without any particular order. For the later stage, indeed, the radial density function they computed gave the image of a structure that could be described as a mixture of amorphous and square lattice domains. This study, beside reporting for the first time that the oocyte development impacts on the

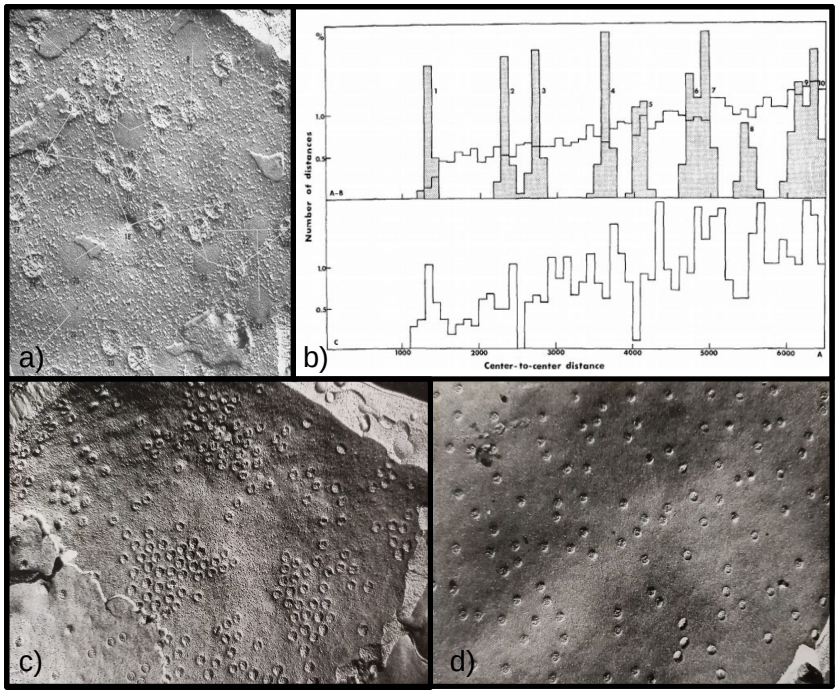

Figure 4.2: First attempts of analysis of NPCs spatial distribution in different cell conditions (a) Electron microscopy image of the outer nuclear envelope of a rat kidney cell nucleus; white lines represent some of the computed distances among nuclear pores; (b) Histogram of NPCs distances compared to other spatial distributions of points: A represents the distribution of random points, B (in grey) represents the histogram obtained from hexagonally arranged points; C is the histogram of the distances between pore centers computed for a rat kidney nuclear envelope (the number of pore-to-pore distances is expressed as a per cent of all distances calculated, class interval is 100 Å). It can be noticed that some of the peaks of the experimetal distribution are found in correspondance of the ones of the hexagonally arranged points, but the overall distribution of NPCs is way more complex, showing for example even a minor maximum at a distance compatible with the diagonal of squarely arranged pores. (c) Electron microscopy image of the nucleus of a gonocyte from the testis of a 5-day-old guinea-pig. Clusters of densely packed nuclear pores are clearly visible, separated by pore-free areas. (d) Electron microscopy image of Sertoli cell nuclei from adult guinea-pig testis. The pore complexes are numerous and apparently random in their distribution. Panel (a) and (b) are an adaptation from Gerd G. Maul et al. [67], panel (c) and (d) are from Don W. Fawcett et al. [33], Copyright 1979 with permission of Elsevier.

nuclear organization and the structure of NPCs, paves the way towards further investigations on how the structure of NPCs are linked with physiological activity and on the relation between the large scale organization of NPCs and the constituent of the nuclear envelope [93]. In the previous discussion, we have showed the state of the art for the observation of nuclear pores spatial distribution, with significative experimental results obtained in the biological field. The scope of this thesis and of the following work is to look at this problem from a different and interdisciplinary perspective, with the eyes of a soft matter physicist. In particular, in the following chapter, we will start our analysis from the experimental images of nuclear pores obtained by Sélles et al [93] and we

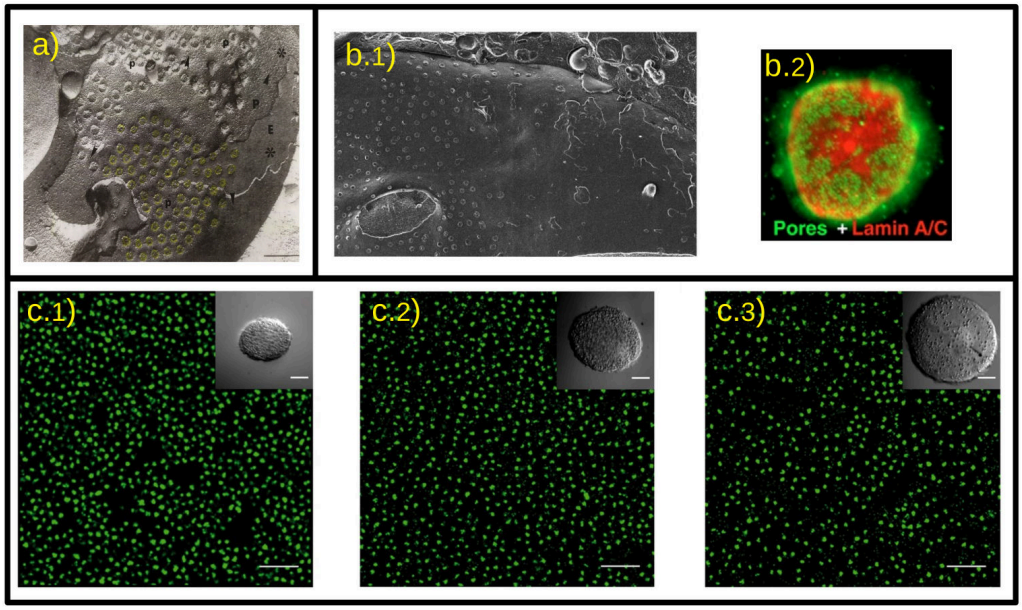

Figure 4.3: More recent images of NPCs spatial distribution in different cell conditions (a) Nuclear pores distribution in apoptotic HL60 human leukemia cells, observed by freeze-fracture electron microscopy. Pore-free areas appear separated from dense pore clusters (colored in yellow); (b.1) Scanning electron microscopy image of a nuclear surface of freeze-fractured HeLaS3 cells (human cancer cells) during the eraly G1 phase, the first phase of the cell cycle that takes place in eukaryotic cell division. During G1 phase, the cell synthesizes mRNA and proteins in preparation for subsequent steps leading to mitosis. Many nuclear pores are clearly visible with a large pore-free island. (b.2) Immunofluorescence image of G1 HeLaS3 cell nucleus shows an accumulation of the inner nuclear membrane protein lamin A/C in the pore-free islands. (c) Direct Stochastic Optical Reconstruction Microscopy (dSTORM) images of nuclear envelopes from *Xenopus laevis* oocytes at different stage of development (respectively at stage II for figure (c.1), stage IV for figure (c.2) and stage VI for figure (c.3)). The central channel of each pore (visualized as a green spot on the images) is labelled with the fluorescent protein $WGA - Alexa647$. Scale bar is $5\mu m$. In the insets, instead, stereomicroscope images of the whole oocyte respectively at stage II, IV and VI is represented with a scale bar of $50\mu m$. Panel (a) is an adaptation from Elisabetta Falcieri et al.[32] Copyright 1994 with permission of Chapman & Hall, panels (b.1) and (b.2) are an adaptation from Kazuhiro Maeshima et al. [65], panels (c.1),(c.2) and (c.3) are an adaptation from Julien Sellés et al. [93].

will use tools commonly employed to study atomic structural and topological features of ordinary matter, to deepen our understanding of the NPCs spatial distribution on the nuclear envelope.

CHAPTER 5

Spatial organization of nuclear pores in *Xenopus laevis* oocytes

5.1 Introduction

As seen in the previous chapter, the structure of nuclear pores has been the object of considerable investigation, with great effort spent in determining the pores composition, in terms of different protein complexes. In that direction, the experimental techniques such as electron microscopy (EM) and cryo-electron tomography (cryo-ET) have already been accompained by in silico studies involving all-atom and coarse-grained molecular dynamics simulations, aimed to characterize NPCs structure [37],[69],[77]. Nevertheless, the question of how nuclear pores are arranged on the nuclear surface is still less studied and the nature of the interactions among NPCs is still an unresolved issue. In these contexts, the experimental observations (showed in Chapter 4) have been so far the main and only way of investigation, since attempts of modelling NPCs spatial distribution and using computer simulations to deepen our understanding on it were missing. In this chapter we will try to fill that void. We will start our study from the analysis of super-resolution images of the surface of *Xenopus laevis* oocytes nuclei during development perfomed by Sellés et al. [93]. In details, we will characterize the arrangement of nuclear pores on the NE using tools typical of the physics of soft materials, such as the calculation of the radial distribution function (RDF), local order parameters and Voronoi tessellation. Then, to interpret the experimental results, we will consider the hypothesis of an effective interaction acting among the nuclear pores, to study if this can explain the spatial distribution of pores on the nuclear membrane. To this end, we will build a potential with octagonal symmetry (mimicking typical pore shapes) to model the interaction between nuclear pores and to perform extensive numerical simulations at different pore density. The simulated configurations we will obtain will represent a first attempt of studying in silico the nuclear pore complex globally, unveiling peculiarities and characteristics of the spatial distribution of NPCs.

5.2 Material and Methods

5.2.1 Experimental images

The first step of our work consists of an accurate analysis of recent experimental images, investigating the spatial distribution of nuclear pores on the nuclear envelope. We decided to analyze the super-resolution microscopy images of nuclear pores of *Xenopus laevis* oocytes, observed during their development by Selles et al. [93], and to keep them as experimental counterpart for comparison with our simulations. According to the stage

of development of the oocyte (previously defined for *Xenopus laevis* in a classic paper [27]), three groups of images have been identified: from the early Stage II, to an intermediate Stage IV, to a later Stage VI. A different number of samples was taken at each stage, specifically, 6 samples for Stage II and 11 samples for both Stage IV and Stage VI. The images are 2560×2560 pixels (px) wide, with 1 px corresponding to 0.01 μm. Portions of some experimental images are illustrated in Fig. 5.2a and b.

Tracking of Nuclear Pores

The main information we needed to extract from the experimental samples, were the spatial coordinates of each nuclear pores, to perform our statistical analysis of their distribution. To do so, we extracted the positions of the nuclear pores using Trackpy v0.4.2, a Python package for particle tracking in 2D, 3D, and higher dimensions [1]. In particular, we use the *trackpy.locate* routine to first discriminate the nuclear pores. The working principle is the following: i) preprocess the image performing a bandpass filter (i.e. performing a convolution with a Gaussian to remove short-wavelength noise and subtracting out long-wavelength variations by subtracting a running average, to retain features of intermediate scale), ii) applying a threshold over the color channels, and iii) locating all the peaks of brightness, each referring to the position of a pore [1],[19]. The parameters used for the tracking procedure are $diameter = 9$ px, $minmass$ (the minimum integrated brightness, working as a threshold value) value instead is chosen according to the samples. No threshold ($minmass = 0$) is used in the high density samples of Stage II, while higher values of this parameter are necessary to correctly detect pores in the more noisy experimental images of Stage IV and VI. From this tracking procedure, we extracted the 2D coordinates of the nuclear pores, on which our statistical analysis is based. The tracking procedure also allowed us to determine the density in terms of number of pores for nuclear envelope surface unit of the experimental samples: 34.9 ± 2.3 NPC/μm^2 for Stage II, 25.6 ± 2.3 NPC/μm^2 for Stage IV, 20.5 ± 1.7 NPC/μm^2 for Stage VI. Errors represent the standard deviation computed on the ensemble of samples for each developmental Stage. Those density values are a bit underestimated, compared to the ones computed by Sellès et al. (respectively 53.8 ± 0.9 NPC/μm^2 for Stage II, 46.2 ± 0.9 NPC/μm^2 for Stage IV, 36.7 ± 0.8 NPC/μm^2 for Stage VI) [93]. This is due to different techniques used for tracking procedure and to an intrinsic uncertainty connected with the experimental measures. Those were performed by optical super-resolution microscopy, that introduce some arbitrarily in identifying as pores some spot 'fragmented' due to small microscope displacement, affecting the overall counting.

5.2.2 Numerical Simulations

Once that we have determined the positions of the experimental nuclear pores, we wanted to move a step further, proposing a simple model that can help in the interpretation of the experimental results. To do so, we hypothesized an effective interaction acting among the nuclear pores and, starting from this assumption, we tested some simple potentials to describe the pore-pore interaction. Those potentials allowed us to perform extensive numerical simulations of systems composed by several interacting nuclear pores and to obtain in silico configurations of NPCs at different densities. In particular, by choosing how to model the interaction among nuclear pores, we took into account their peculiar octagonal shape. This characteristic was observed in early experimental studies [102],[83] and subsequently confirmed by structural studies on nucleoporins (a family of proteins that are the main components of the nuclear pore complex in eukary-

otic cells) and by recent advancements in experimental techniques, such as cross-linking mass spectrometry and cryo-electron tomography [61]. In the following paragraph, we elucidate the details of our simulation model based on simple potentials describing the pore-pore interaction.

Model Potentials for Nuclear Pores

To take into account the composite structure of each nuclear pore and its overall octagonal shape, we build a coarse-grain model of the pore, consisting of a central particle surrounded by eight particles located at the vertices of a regular octagon, of circumradius R. For simplicity, the so-modeled pore is treated as an undeformable rigid object. In Figure 5.1 b) a visualization of a single simulated pore in Ovito [97] is given. Following reference experimental data [28], [93], in all the simulations we have set $R = 67.5\,\text{nm}$. The overall interaction potential acting among the particles of two neighbouring pores is made up of three terms, each consisting in a Lennard-Jones (LJ) potential,

$$V(r_{ij}) = 4 \cdot \varepsilon \cdot \left(\left(\frac{\sigma}{r_{ij}} \right)^{12} - \left(\frac{\sigma}{r_{ij}} \right)^{6} \right) \quad , \qquad r_{ij} < r_{cut} \tag{5.1}$$

where $r_{ij} = |\mathbf{r}_i - \mathbf{r}_j|$ is the distance between particle i and particle j, and ε, σ, and r_{cut} are parameters that depend on the interaction term:

- **center-center interaction** – the central particle of a pore interacts repulsively with the central particle of a neighbouring pore. For this term we have set $\varepsilon_{cc} = 0.01$ pg·μm^2/μs^2, $\sigma_{cc} = 0.12$ μm, and the cutoff distance is set $r_{cc}^{cut} = 2^{\frac{1}{6}}\sigma_{cc}$ so to make the interaction purely repulsive. This term is necessary to prevent unphysical configurations such as the case of overlapping pores that were otherwise seldom encountered.

- **center-vertex interaction** – the central particle of a pore repulsively interacts with the vertex particle of a neighbouring pore. Again, this is introduced to avoid pores overlap and compenetration. LJ parameters for this term are $\varepsilon_{cv} = 0.01$ pg·μm^2/μs^2, $\sigma_{cv} = 0.08$ μm, $r_{cv}^{cut} = 2^{\frac{1}{6}}\sigma_{cv}$.

- **vertex-vertex interaction** – the vertex particle of a pore interacts with the vertex particle of a neighbouring pore. We first considered full LJ interaction (long range attractive, short range repulsive), but then the purely repulsive case was also investigated, trying to gain insight on the nature of pore-pore interaction. For the full LJ interaction we have set $\varepsilon_{vv} = 5{\cdot}10^{-4}$ pg·μm^2/μs^2, $\sigma_{vv} = 0.02$ μm, and the cutoff distance is set to $r_{vv}^{cut} = 2.5\sigma_{vv}$ so to include the attractive part. For the purely repulsive case, instead, we have set $r_{vv}^{cut} = 2^{\frac{1}{6}}\sigma_{vv}$. By construction, since the central particles are surrounded by vertex particles, in our model the overall pore-pore interaction is mostly driven by the present term.

In all the cases, the LJ potentials are shifted to zero out at the cutoff distance, in order to avoid any energy discontinuity. Fig. 5.1 c) reports the total interaction energy of an octagonal pore (centred at the origin) with one corner particle of a second pore,

as a function of the position of the latter, in the case of full LJ potential in the vertex-vertex term. The resulting potential energy surface (PES) shows a strongly repulsive core region (in blue) and trapping regions (in red) concentrated at the proximity of the eight corner sites. The same plot is shown in Fig. 5.1 d) for the purely repulsive vertex-vertex term; here the PES is completely repulsive (blue), with a well defined octagonal shape. For comparison, we also performed simulations assuming a simpler interaction among the pores: we tested a purely repulsive spherical potential, modelling the NPCs as circular, neglecting the eightfold symmetry. The spherical potential is a simple LJ with the following parameters: $\varepsilon = 5 \cdot 10^{-4}$ pg·μm^2/μs^2, $\sigma = 0.12$ μm, $r_{cut} = 2^{\frac{1}{6}}\sigma$. In the following, when not specified, the potential used in the simulated results is the one represented in Fig. 5.1 c), corresponding to full LJ for the vertex-vertex term (attractive corners).

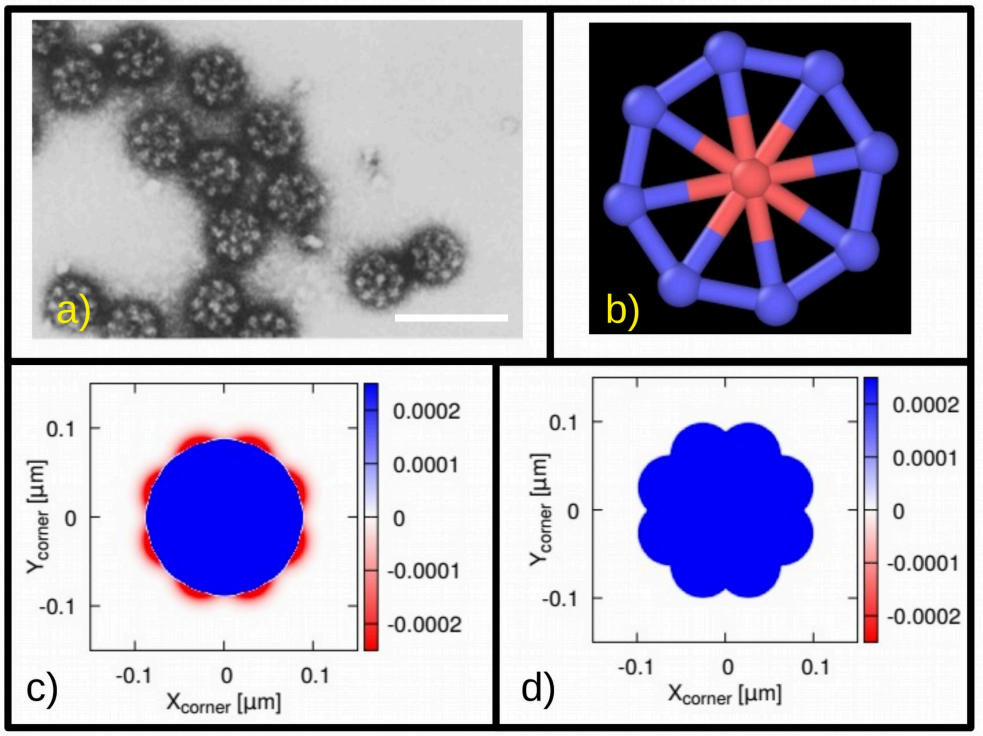

Figure 5.1: Details of the simulated nuclear pores (a) Detached pore complexes released onto the microscope grid from a nuclear envelope immersed in low salt medium containing 0.1% Triton $X-100$, from which the octagonal shape is clearly visible. Scalebar is 0.25 μm. Panel (a) is an adaptation from Unwin et al. [102]. (b) Visualization of a single simulated nuclear pore through Ovito [97]. (c) and (d) potential energy surfaces obtained from the modelled interaction between a pore and a corner of a neighbouring pore: blue areas mark strongly repulsive regions, while red areas mark trapping centres. The two images represent the full LJ potential case for the vertex-vertex interaction term (c) and the purely repulsive case (d), respectively.

Obtaining Configurations of Simulated Nuclear Pores

Simulations of nuclear pore assemblies were performed using LAMMPS[78], with a timestep $\Delta t = 10^{-5}$ μs. We started from initial configurations of 1000 randomly-positioned octagonal pores, confined in a periodic square box with side $L = 40\,\mu$m. To mimic the different experimental densities of nuclear pores observed during the oocyte development, the random configurations undergo alternatively 10^5 steps of continuous box compression at a constant temperature $T = \frac{2}{3}\frac{\epsilon_{corn}}{k_B}$, followed by a $2{\cdot}10^5$ steps annealing from the higher temperature $T = \frac{\epsilon_{corn}}{k_B}$, back to to $T = \frac{2}{3}\frac{\epsilon_{corn}}{k_B}$, to allow thermally-assisted rearrangements. Such procedure is iterated until the required density is obtained. A final energy minimization at $T = 0$ K in $2{\cdot}10^6$ steps is then performed. Following the above protocol, we obtained configurations with a density of 20, 26, 36, 46, and 53 NPC/μm^2. For each density value we obtained 10 different realizations, starting from different random initial positions, to permit proper statistical averaging. Examples of nuclear pore configurations obtained in silico are shown in Fig. 5.2c and d.

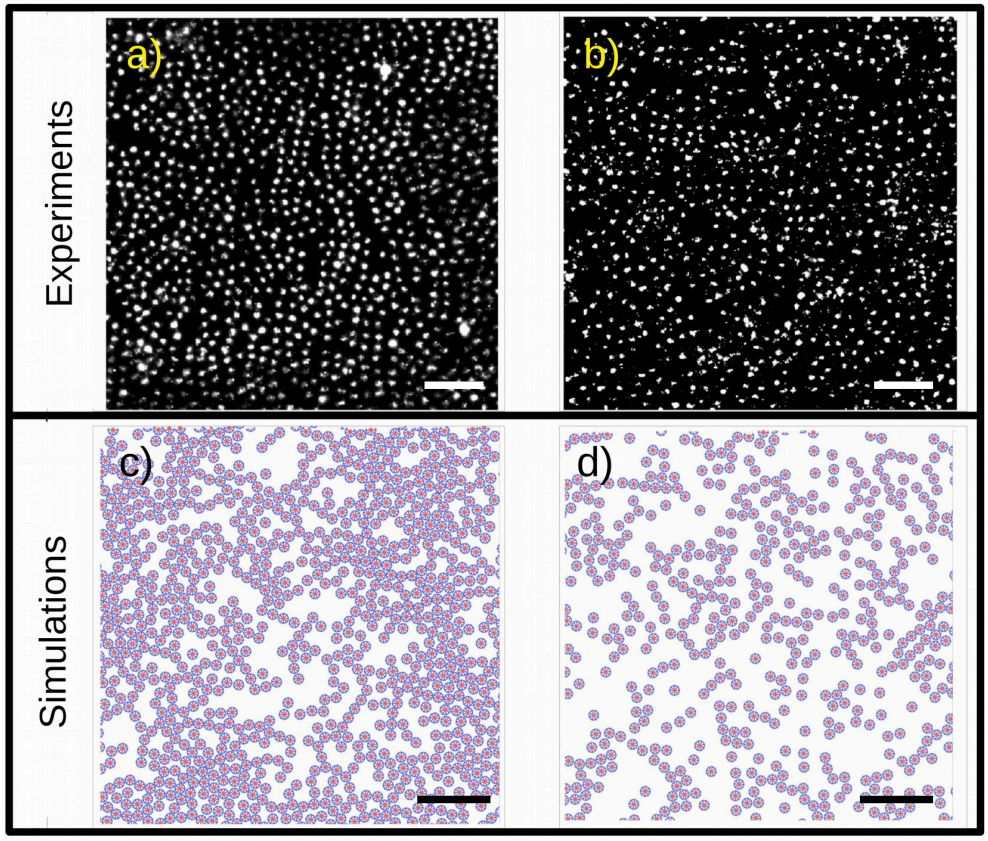

Figure 5.2: Visual comparison of real nuclear pores coming from experimental images and simulated nuclear pores (a) and (b) portions of experimental images of nuclear pores in *Xenopus laevis* oocyte at different developmental stages, Stage II (a) and Stage VI (c), respectively, obtained using super-resolution microscopy. Panel (a) and (b) are adaptations from Sellés et al. [93]; (c) and (d) two configurations of nuclear pores obtained from simulations, for comparison with experimental data. The density is 36 NPC/μm^2 for (c) and 20 NPC/μm^2 for (d). Scalebars are 1 μm.

5.2.3 Statistical Analysis of Nuclear Pores Structure

To provide a statistical comparison of simulations with reference experimental data we have applied three different post-processing techniques over the simulated pore assemblies and to their experimental counterparts. In this paragraph we will describe in detail those techniques, commonly used in matter physics and in the characterization of amorphous systems.

Radial Distribution Function

In Gibbs's formulation of statistical mechanics, the distribution of phase points of systems belonging to an ensemble is described by a phase-space probability density $f^{[N]}(\mathbf{r}^N, \mathbf{p}^N; t)$. This is the probability that, at time t, the physical system is in a microscopic state represented by a phase point lying in the infinitesimal, $6N-$dimensional phase-space element $d\mathbf{r}^N d\mathbf{p}^N$. Given a complete knowledge of the probability density, it would be possible to calculate the average value of any function of the coordinates and momenta, obtaining observable properties of the system of interest. In a system of fixed number of particles, volume and temperature (well described by the canonical ensemble), in which the Hamiltonian can be written as $H = K_N + V_N$, the reduced phase-space distribution functions ${f_0}^{(n)}$ can be written as the products of two terms ${f_0}^n(\mathbf{r}^n, \mathbf{p}^n) = {\rho_N}^n(\mathbf{r}^n){f_M}^n(\mathbf{p}^n)$. The second term ${f_M}^n(\mathbf{p}^n)$ is a product of n independent Maxwell distributions and depends on the kinetic terms K_N. The first term depends on the potential V_N. In particular the n-particle density is defined as:

$$ {\rho_N}^n(\mathbf{r}^n) = \frac{N!}{(N-n)!}\frac{1}{Z_N}\int exp(-\beta V_N) d\mathbf{r}^{N-n} \tag{5.2} $$

and yields the probability of finding n particles of the system with coordinates in the volume element $d\mathbf{r}^n$, irrespective of the positions of the remaining particles and irrespective of all momenta. The knowledge of the low-order particle distribution functions, in particular of the pair density ${\rho_N}^{(2)}(\mathbf{r}_1, \mathbf{r}_2)$, is often sufficient to calculate the equation of state and other thermodynamic properties of the system. The n$-$particle distribution function ${g_N}^{(n)}(\mathbf{r}^n)$ is defined in terms of the corresponding particle densities. For an homogeneous and isotropic system the pair distribution function ${g_N}^{(2)}(\mathbf{r}^1, \mathbf{r}^2)$ depends only of the separation $r_{12} = |\mathbf{r}_2 - \mathbf{r}_1|$. In this case the pair distribution function is usually called radial distribution function and written simply as $g(r)$ [40].
For those reasons, to characterize our systems and to gain insight on the local structure of the nuclear pore complex on the nuclear membrane, we made use of the Radial Distribution Function (RDF) in 2D [41]:

$$ g(r) = \frac{L^2}{2\pi r N^2}\sum_{i=1}^{N}\sum_{\substack{j=1 \\ j\neq i}}^{N}\langle\delta(r - r_{ij})\rangle \tag{5.3} $$

where N is the number of particles in the system, L is the system size and r_{ij} is the distance between particle i and j. The RDF has proven a key role in the theory of monatomic liquids. In fact, it has already been used to characterize amorphous colloidal solids [44] and to study glass transitions in Lennard-Jones systems [9]. In the context of Lennard-Jones systems, in particular, the structure of the g(r) allowed to investigate the characteristics of the interparticle potentials [9]. For this reason, we will keep in mind this

approach in performing our analysis of the nuclear pores spatial distribution. As an example for the reader, in Figure 5.3 (a) the RDFs of a perfect crystal and of an amorphous material are shown. One can appreciate how effective the function is in determining the shells of neighbours and how it can help in characterising the phase of a material.

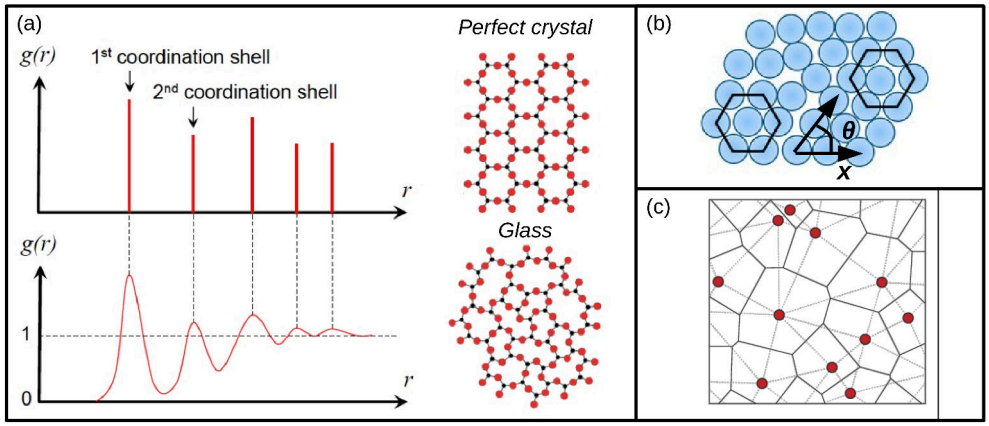

Figure 5.3: Schemes of the techniques used for the statistical analysis of nuclear pores distribution (a) Scheme of the radial distribution function g(r) of a solid (top panel) and of a glass (bottom panel). The g(r) peaks in the crystalline materials represent the positions of the shells of neighbours; in the amorphous case the function show broad peaks in correspondence of coordination shells. (b) Scheme illustrating the way in which local order parameters are computed, in order to detect ordered regions inside a material. (c) Scheme of the Voronoi tessellations; red dots represents the analysed particles.

Hexatic Order Parameter

To better characterize the geometrical properties of the structure formed by the nuclear pores, we computed for each particle the n-fold local orientational order parameter:

$$\psi_n(\mathbf{r}_i) = \frac{1}{nnn} \sum_{j=1}^{nnn} e^{in\theta(\mathbf{r}_{ij})} \tag{5.4}$$

where nnn is the number of nearest neighbours of particle i, $\theta(\mathbf{r}_{ij})$ is the angle formed by the x axis and the vector $\mathbf{r}_{ij}$ connecting particles i and j, as visualized in the scheme of Figure 5.3 (b). Some ordered regions marked by the presence of square lattice and triangular lattice have been observed in experimental nuclear pore complexes of *Xenopus laevis* at different developmental stages [93]. To account for this, we focus our analysis on the order parameters with $n = 6$, for which $|\psi_6| = 1$ for particles belonging to a perfect hexagonal structure, and with $n = 4$, for which $|\psi_4| = 1$, for particles belonging to a perfect square lattice. The determination of nearest neighbour particles is done using a cutoff distance $\sigma_{cut} = 0.15$ μm for the simulations and $\sigma_{cut} = 0.20$ μm for the experimental images. Those values have been chosen looking at typical inter-particle distances in different samples of experimental images and simulated configurations respectively. All the isolated particles ($nnn < 2$) have been marked by zeroing their ψ_n value.

Voronoi Tessellation

Around the center of each pore we have built a Voronoi cell: an area of space containing all points that are closer to one pore than to any other particle. A scheme of this geometrical tessellation can be appreciate in Figure 5.3 (c). For the experimental images, pore centres coordinates are obtained from the tracking procedure and used as 'seeds' for the Voronoi tessellation. For the simulations, instead, only the central particle of each octagon has been considered in the Voronoi analysis. By construction, each Voronoi cell has polygonal shape, with a number of sides that corresponds to the number of neighbours. To compute the Voronoi tesselation we used the Python library Freud [79], that allows to account for periodic boundary conditions. By this method, we managed to extract for each particle the number of neighbours (particles are considered neighbours if they share an edge in the Voronoi diagram) and the size of each associated Voronoi cell.

5.3 Results

5.3.1 Global structure of NPC

From the RDF of the experimental samples, we note that at high density (early stage of development of the oocyte) $g(r)$ shows a liquid-like shape, with two peaks clearly visible (see Fig. 5.4 (a)). In fact, in monoatomic liquids at short range, $g(r)$ shows a pattern of peaks representing the nearest neighbour distances and at large r it tends to unity due to total loss of order [41]. As the density decreases during oocyte development (Fig. 5.4 (b) and (c)), the second peak of the experimental $g(r)$ tends to disappear, while the first peak tends to flatten out, thus converging toward a gas-like phase in which the order is lost.

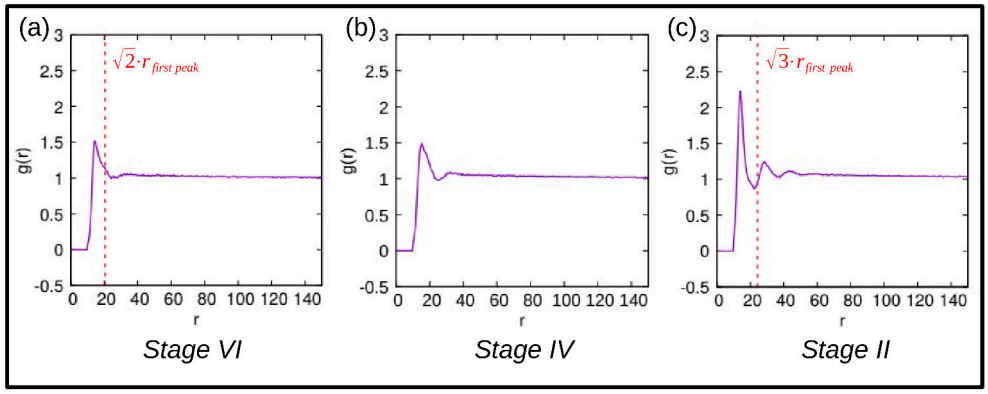

Figure 5.4: Radial distribution functions of the experimental distributions of nuclear pores The $g(r)$ of the nuclear pores is reported for three different developmental stages of *Xenopus laevis* oocytes. In particular the curves are obtained from the experimental images for Stage VI - (a), Stage IV - (b), Stage II - (c). The dashed red lines represent the theoretical expectation for second peaks positions in the assumption of regular square (a) or hexagonal (c) structures.

Previous analysis of the experimental images suggested a significant presence of square lattice domains of nuclear pores at low density (Stage II)[93]. For this reason, we have looked for a specific peak in the $g(r)$ function. In the case of a regular square lattice, a second peak should be present at $x_{sq} = \sqrt{2}\,x_1$ (where x_1 represent the spatial

coordinate of the first peak of the $g(r)$ function), however we notice that a peak in this position is not visible. Nevertheless, x_{sq} falls on the tail of the first peak (which is quite flat), suggesting that some sparse regions with square lattice could be present inside the amorphous liquid. Similar considerations have been done for hexagonal structures at high densities: if a regular hexagonal packing of pores is present, the $g(r)$ should display a peak at the position $x_{hex} = \sqrt{3}x_1$ and again, this is not the case, with x_{hex} falling only on the growing part of the second peak for the high density configurations. Some hexagonal structures at high density could be present but are not predominant, being the spatial distribution of NPCs mainly disordered.

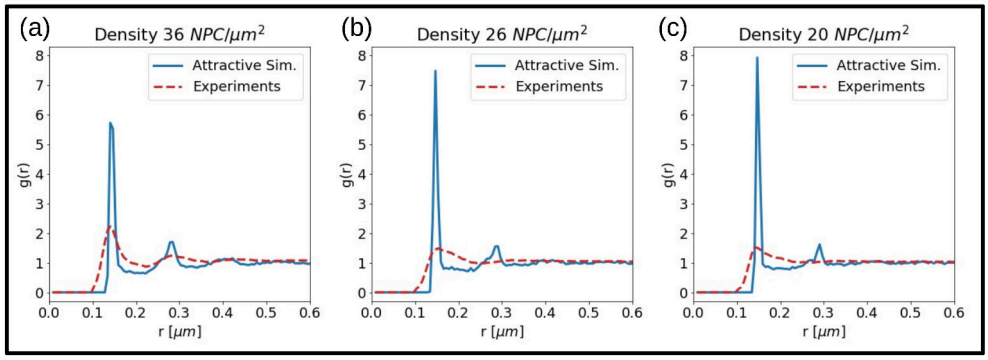

Figure 5.5: Radial distribution functions of simulated nuclear pores The $g(r)$ is reported for three different densities of the nuclear pores. Blue curves are from averages over ten simulations with attractive octagon potential. Dashed red curves are obtained from the experimental images for Stage II - (a), Stage IV - (b), Stage VI - (c).

Focusing on the $g(r)$ obtained from our simulations with octagonal attractive potential (Fig. 5.5), it reproduces the above described liquid-like profile, presenting just a few peaks emerging over an otherwise flat profile. Furthermore, the positions of the peaks in the simulated $g(r)$ match nicely with the experiments (especially for what concerns the first peak), suggesting that our model is able to capture the relevant features of the effective interaction among the nuclear pores on the nuclear membrane. This is a non-trivial result, as the position of the $g(r)$ peaks closely reflects the interactions held between the constituents, and are a signature of each material and its peculiar properties, as shown in previous studies of noble gases or water [109, 30, 95, 12]. Ultimately, from this analysis, we can rule out the significant presence of extensive crystalline regions. The differences in experimental and simulated peaks height that emerges from Fig. 5.5 could origin from the fact that the simulated particles have, by construction, exactly the same radius while the distribution of nuclear pore size is more broadly spread in experiments (which is even more accentuated by the fluorescence technique used to obtain the experimental configurations). When computing shells of neighbours with the $g(r)$ function this size variability could bring to more spread (and so flattened) peaks.

5.3.2 Orientational Order

In Fig. 5.6 and Fig. 5.7 we report the calculated local order parameter ψ_6 and ψ_4, as previously defined, for some experimental samples and for the configurations obtained from simulations, respectively. The cutoff to consider a pore as a neighbour was set to $\sigma_{cut} = 0.20\,\mu$m for the experiments and $\sigma_{cut} = 0.15\,\mu$m for the simulations. These values

were chosen considering the typical pore-pore distances.

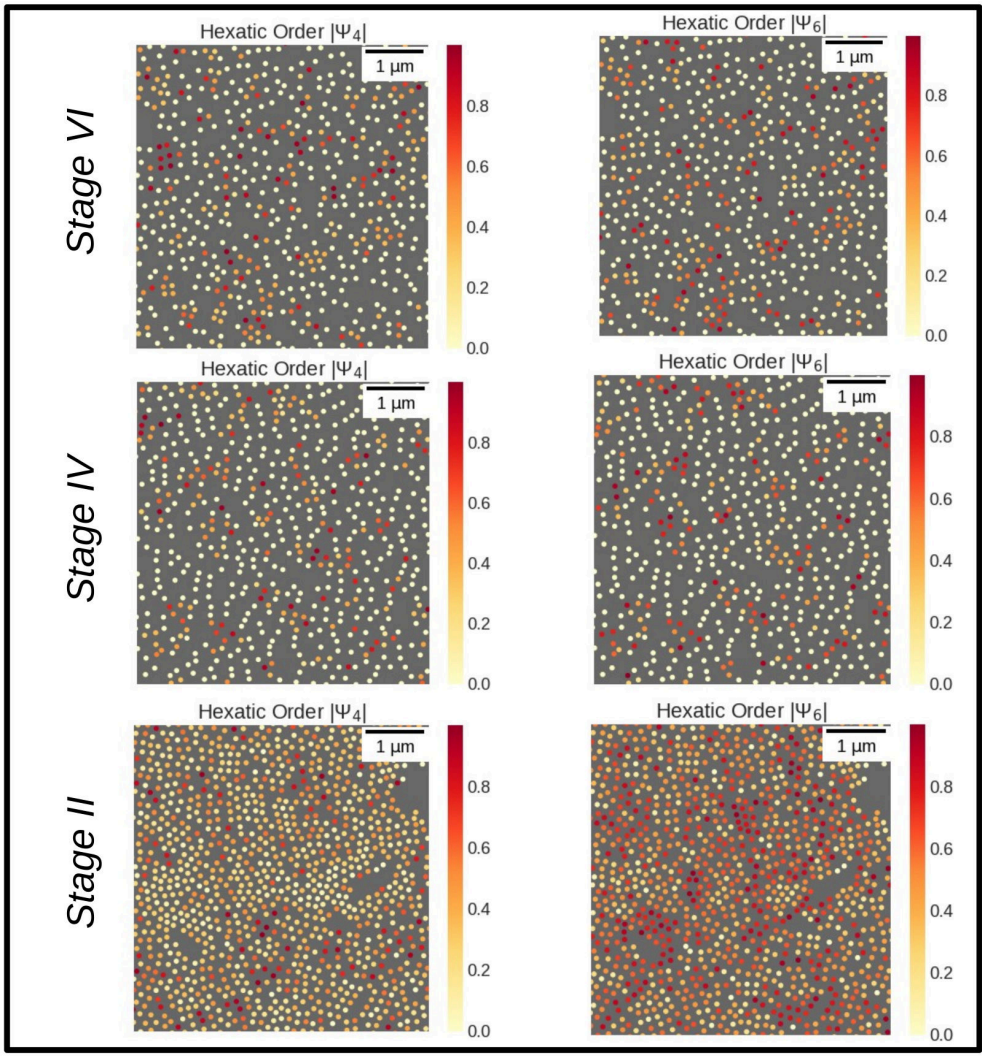

Figure 5.6: Local order parameters coloured maps for experimental pore configurations Snapshots of pores coloured as a function of the local order parameter. Each row of figures shows a different Stage of development of the *Xenopus laevis* oocytes; the two columns show the local order parameters ψ_4 and ψ_6 respectively.

From Fig. 5.6, looking at the later Stages of oocytes development (Stage IV and Stage VI), it can be observed that only few pores are associated with square symmetry ($\psi_4 \sim 1$). The same consideration holds also for the low density simulations analysed in Fig. 5.7. Instead, the figures obtained for earlier Stage II, as well as the simulation obtained with high pore densities (e.g.), show much broader regions associated with triangular lattice structures ($\psi_6 \sim 1$). In those samples, in presence of higher pore densities, more nuclear pores belong to a regular structure and some regions with clear hexagonal order appears.

To further investigate such behaviour, we computed the distribution of the local or-

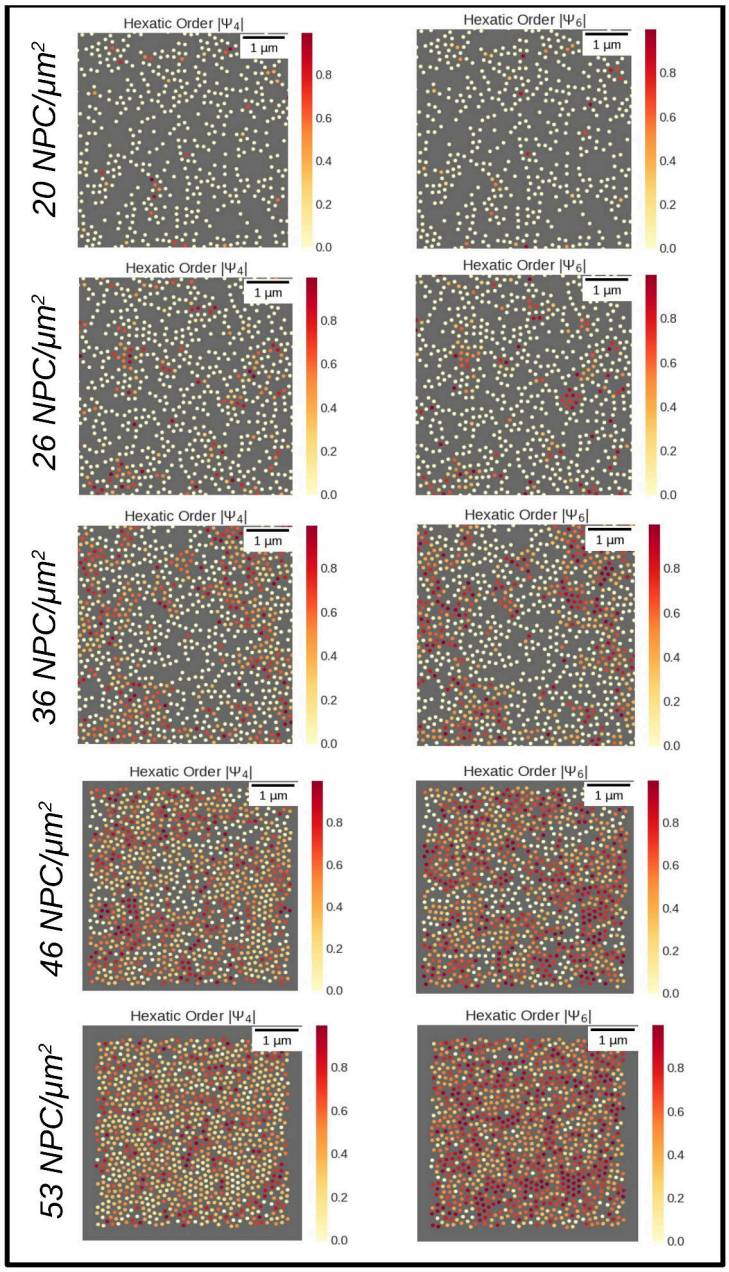

Figure 5.7: Local order parameters coloured maps for simulated pore configurations Snapshots of pores coloured as a function of the local order parameter. Each row of figures shows a different simulated density of nuclear pores; the two columns show the local order parameters ψ_4 and ψ_6 respectively.

der parameters $P(\psi_6)$ and $P(\psi_4)$ averaged over all the samples for each value of the density, as reported in Fig. 5.8. First, we can observe that the distributions of the experimental samples (Fig. 5.8a,b) are all unimodal, thus confuting the hypothesis of two

different coexisting phases, as suggested in previous analysis [93]. Secondly, we notice that for both ψ_6 and ψ_4 the distributions are peaked at a value which increases with the density. The largest mode value is obtained for ψ_6 at the highest density (Stage II), suggesting a preference for hexagonal structures in the dense limit. The above trends of the distributions with the density are well reproduced by the simulated NPCs, as reported in Fig. 5.8c and Fig. 5.8d. For a more straightforward comparison we have reported in Fig. 5.8e the average value of $|\psi_6|$ and $|\psi_4|$ as a function of the pores density, for both simulations and experiments. For the former, we observe that both $|\psi_6|$ and $|\psi_4|$ values slowly increase with the density, showing the same values until a density of $36\,\mathrm{NPC}/\mu\mathrm{m}^2$ where a bifurcation occurs. Beyond that density value, $|\psi_4|$ seems to saturate while $|\psi_6|$ keeps increasing, thus favouring the hexagonal order at high density. It is worth to note that, in the explored density range, the $|\psi_6|$ value is far from approaching unity, corresponding to a crystalline structure, indicating that much larger densities would be required for such an ordered phase. Finally, we note that in Fig. 5.8e the points associated to the experimental data do not fall exactly on the theoretical curves derived from the simulations. This can be partially explained with the uncertainties connected with the experimental observations of the nuclear pores, that affect the density evaluation. On the other side, this discrepancy could also be due to the fact that our eightfold interaction potential, while describing quite well some key aspects of nuclear pores spatial configurations, is not enough to exactly reproduce the experimental local order of nuclear pores on the nuclear surface. Despite that, the experimental points show a trend very close to that of the simulation, with an initial overlapping of $|\psi_6|$ and $|\psi_4|$ values, and a further bifurcation at higher density.

5.3.3 Properties of Voronoi cells

We performed a Voronoi tessellation on the nuclear pores centres extracted both from the experimental images and from the configurations obtained via simulations. Examples of Voronoi tessellation performed on NPC from the experimental images and from the simulated configurations are reported in Fig. 5.9 and Fig. 5.10, respectively.

The comparison of high density samples, in particular, shows similar tessellation patterns in experiments and simulations.

A statistical analysis on the number of sides N of the Voronoi cells at different densities (Fig. 5.11a and Fig. 5.11c), clearly shows that the $N = 6$ occurrence increases with the density, and viceversa for the the $N = 4$ occurrence. Therefore, the Voronoi analysis enforces the idea, already anticipated above by the local order parameter, that the hexagonal configuration is favoured at high densities, at the expense of other kind of local order arrangements. Correspondingly, in agreement with experimental observations, the presence of some square structures at low density is also supported. However, we note that at any density a significant number of cells with $N = 5$, about half between those with $N = 4$ and $N = 6$. We associate this with the particular sensitivity of the Voronoi tessellation method to "defect", i.e. deviations with respect to the ideal symmetric cases. To provide a further comparison, we report in Fig. 5.11b and Fig. 5.11d the distribution of the Voronoi cells area. Again, a good agreement between the experiments and our model is obtained, with much narrower distributions at higher densities, shifting toward higher area values and broadening out as density decreases.

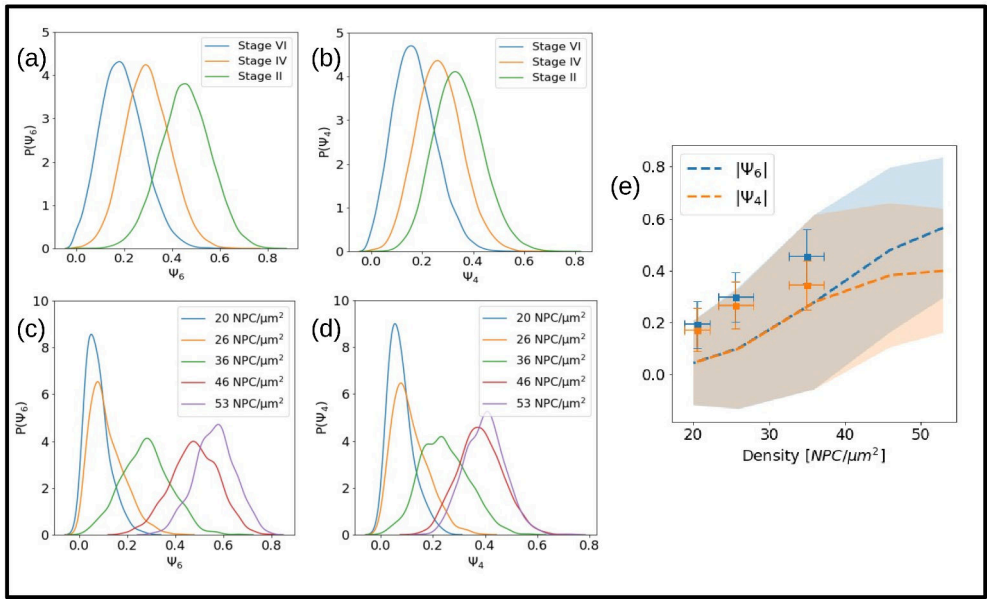

Figure 5.8: Distributions of local order parameters The distribution of the local order parameters at different pores densities is reported for (a),(b) experimental samples and (c),(d) for simulated configurations; (e) the average $|\psi_6|$ and $|\psi_4|$ values as a function of the density. The dashed lines report the values obtained from the simulations, with shadows highlighting the respective standard deviation. The points represent the values computed from the experimental samples, with vertical errorbars for the standard deviation, and horizontal errorbars reporting the error on the density, as described in the paragraph 'Tracking of Nuclear Pores'

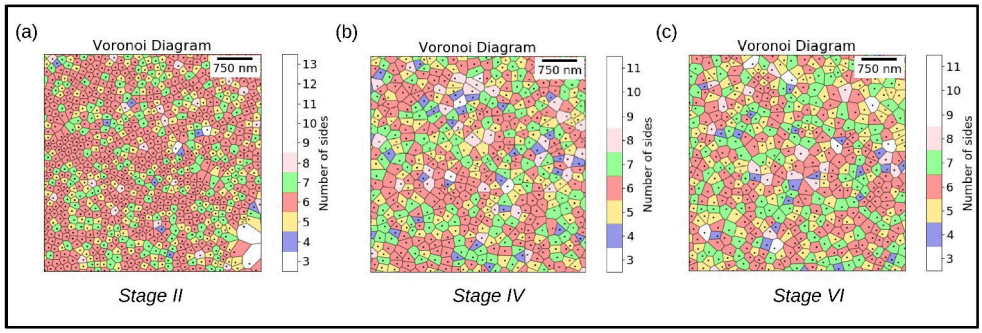

Figure 5.9: Voronoi tessellation applied to experimental nuclear pores In (a), (b) and (c) examples of Voronoi tessellation are given for experimental samples at Stage II, IV and VI respectively.

5.3.4 Alternative models for pore-pore interaction

In this paragraph, we show some results obtained using alternative potentials for pore-pore interactions. Those results have been compared with the eight-fold potential with attractive corners, that represents the standard model used to obtain all the results previously illustrated. More in detail, two alternative potentials for pore-pore interaction have been tested:

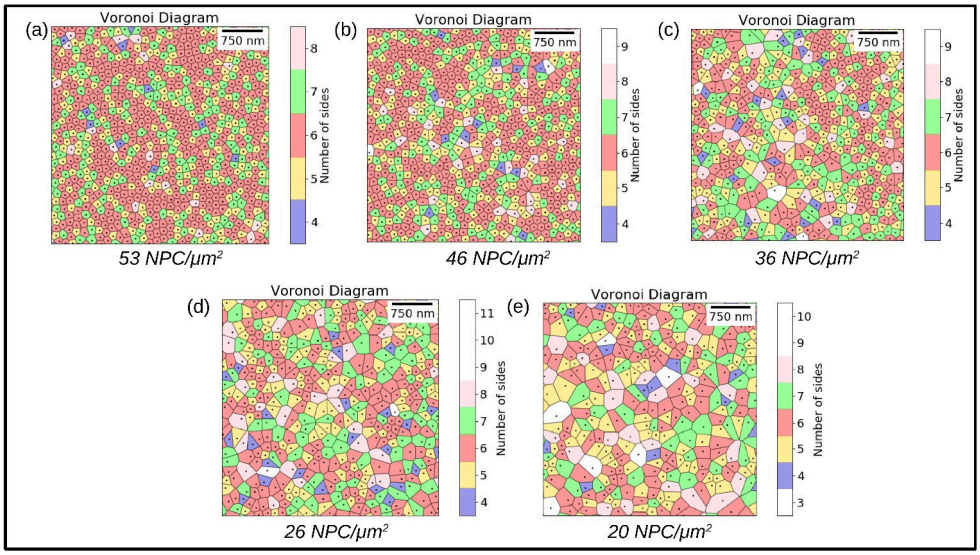

Figure 5.10: Voronoi tessellation applied to simulated nuclear pores Examples of Voronoi tessellation are given for simulated configurations of nuclear pores at different densities.

- eight-fold potential fully repulsive
- simple Lennard-Jones (spherical symmetry)

The repulsive octagonal potential is obtained using the same LJ parameters of the attractive potential previously described, except for the vertex-vertex interaction which is truncated to be fully repulsive: $r^{cut}_{vert-vert} = 2^{\frac{1}{6}}\sigma_{vert-vert}$. The simple spherical potential is obtained with the following LJ parameters: $\epsilon = 5 \cdot 10^{-4}\,\mathrm{pg}{\cdot}\mu\mathrm{m}^2/\mu\mathrm{s}^2$, $\sigma = 0.12\,\mu\mathrm{m}$, $r_{cut} = 2^{\frac{1}{6}}\sigma$.

The statistical analysis methods, described in Material and Methods, have been applied to characterize the distributions of nuclear pores obtained assuming those alternative pore-pore potentials. In Figure 5.12 the radial distribution function of the pores distributions obtained with different models are illustrated.

It emerges that both the repulsive and attractive eight-fold potentials seem to describe quite well the experimental peak location, in particular for what concerns the first peak of the $g(r)$ (see Figure 5.12 c). The potential with spherical symmetry, instead, does not match the experimental peaks. It has to been noticed that we have assumed a LJ potential acting among the pores with parameters compatible with experimental pore sizes ($\sigma = 0.12\mu m$). For this reason, the hypothesis of a pore-pore potential with spherical symmetry can not be completely excluded, perhaps considering an effective interaction size for the pore that does not coincide with its physical size. Despite that, our work seems to suggest that the octagonal shape of the pore and the associated eight-fold symmetry of its interaction potential, play a role in determining the correct spatial distribution of the pores, independently from the attractive or repulsive nature of the pore-pore interaction.

Furthermore, we computed also the local order parameters for the pores configurations, obtained with the alternative potentials. In Figure 5.13 the value of $|\Psi_4|$ and $|\Psi_6|$ averaged over particles and configurations have been plotted for different pore densi-

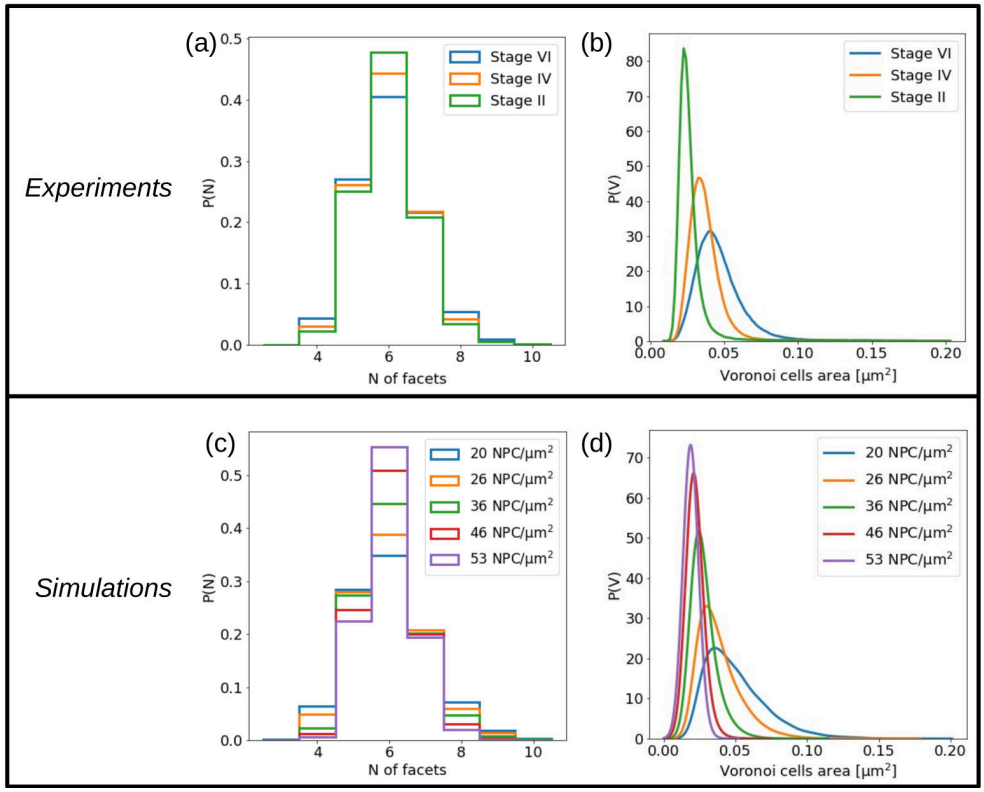

Figure 5.11: Number of neighbours and Voronoi cells size calculated for experimental and simulated nuclear pores In (a) and (c) the histogram of the number of nearest neighbours computed counting the facets of the Voronoi cells are represented. In (b) and (d) we plotted the distributions of the volume, expressed in μm^2, of the Voronoi cells at different densities.

ties. A substantially different behaviour is observed for the pore-pore interaction with spherical symmetry, compared to the values of the local order parameter obtained from the reference eight-fold attractive potential. The simple LJ potential gives a trend that is different from the one that the experimental data suggest: $|\Psi_6|$ is always bigger that $|\Psi_4|$, even at small densities, correctly revealing the preference of spheres for hexagonal packing. Again, also for what concerns the local order parameters, no significant differences have been reported for the eight-fold repulsive potential respect to the eight-fold attractive potential.

5.4 Discussion and Conclusions

A first attempt to investigate the spatial distribution of nuclear pores goes back to the '70s, when the positions of NPCs on the surface of rat kidney nuclei was observed and

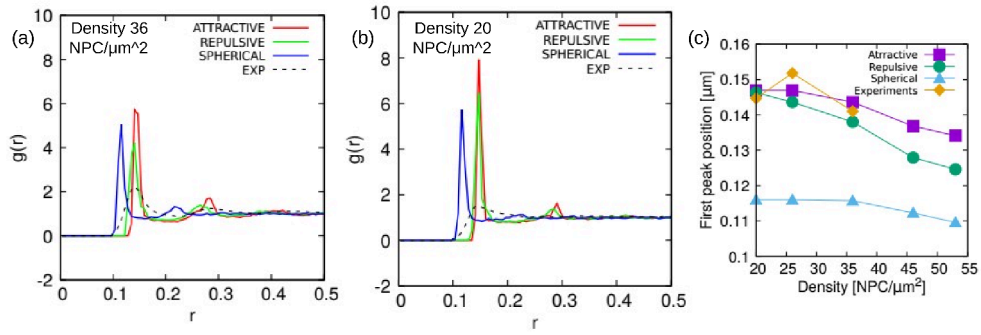

Figure 5.12: Radial distribution functions obtained with alternative models for pore-pore interaction. (a) The radial distribution function for different interaction potential: attractive octagonal potential (red curve), repulsive octagonal potential (green curve) and simply spherical repulsive potential (blue curve). Data are relative to simulations with a density of $36\,\mathrm{NPC}/\mu\mathrm{m}^2$, and compared with the $g(r)$ from experimental images of Stage II oocytes (black dashed line); (b) the same results are shown for simulated densities of $20\,\mathrm{NPC}/\mu\mathrm{m}^2$ and experimental samples on stage VI; (c) the position of the first $g(r)$ peak as a function of the density.

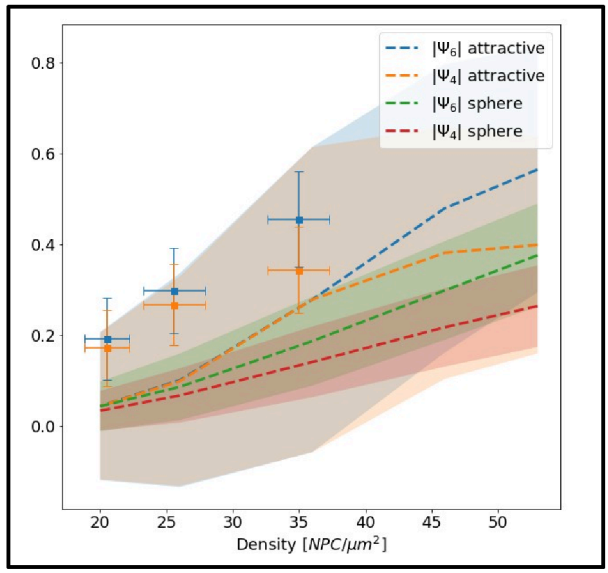

Figure 5.13: Local order parameters for alternative pore-pore interactions The average $|\psi_6|$ and $|\psi_4|$ values as a function of the density for different pore-pore interactions. The dashed lines report the values obtained from the simulations, with shadows highlighting the respective standard deviation. In blue and orange can be observed the local order parameters for the reference eightfold attractive potential, while the dashed red and green curves are referred to the LJ pore-pore interaction, with simple spherical symmetry. The points represent the values computed from the experimental samples, with vertical errorbars for the standard deviation, and horizontal errorbars reporting the error on the density.

distances among them measured [67]. Already at those times, some regularities were found in the distribution of pore-pore distances measured in the samples, suggesting a

non random spatial distribution and some peaks corresponding to hexagonal structures, even if the statistic was too poor to reach further conclusions. More recently, Sellés et al. investigated the angular distribution between first neighbors of nuclear pores, revealing no preferential angles for Stage II and IV *Xenopus laevis* oocytes (high density) and two distinct peaks at $90°$ and $180°$ for later Stage VI, suggesting the presence of square lattice regions at low density [93]. In our study, from the analysis of the radial distribution function $g(r)$ of the nuclear pores on the nuclear membrane of *Xenopus laevis* oocytes, we could not observe peaks in the correspondence of peculiar geometrical structures, meaning that also if some crystalline regions are present, they are quite rare and do not statistically influence the overall NPC spatial distribution. Interestingly, by analysing the $g(r)$ of the nuclear pores, we were able to identify an amorphous, liquid-like structure in which, in the early phase of oocyte development (when NPC density is high), long-range order is soon lost. On the other hand, as the oocyte develops, the nuclear pore density decreases and $g(r)$ shows a behaviour compatible with a more dilute, gas-like system. From a biological point of view, the early stages of oocyte development are associated with intense transcriptional activity, as the oocyte needs to build up a huge reserve of gene products such as mRNAs, tRNAs and proteins in order to correctly fulfil its future role after fertilisation. Once the necessary maternal mRNAs have been copied, transcriptional activity in the later stages of oocyte development becomes lower [91]. These changes in transcriptional activity could be linked to changes in the spatial distribution of NPCs during oocyte development, particularly changes in density. It would be extremely interesting to further explore this connection from a biophysical point of view. For example, by trying to quantify the flow of matter through the pores, as has already been done in some previous kinetic studies, which showed that a single NPC can allow a mass flow of nearly 100 MDa/s [84], at different stages of the cell's life-cycle. The positions of the peaks in the $g(r)$ we computed for nuclear pores, are another key point highlighted from our results. It is known, indeed, from the physics of matter, that the positions of the peaks of the radial distribution function, and their relative distances, give actual information about the geometrical arrangement of the particles within a material, and are a signature of the material itself [15]. In particular, the peak positions allow us to extrapolate, as indirect information, the kind of interaction holding among the constituents of a specific material. Here, we have shown that the eight-fold potential used to model the NPC in our simulations is able to nicely reproduce the experimental $g(r)$ peak locations. In particular, the position of the first peak obtained from the simulations is in excellent agreement with Sellés et al. [93] and with previous observations [67, 33]. Beside that, looking at the paragraph 'Alternative models for pore-pore interaction' we see how, assuming a simple LJ potential acting among the pores (spherical symmetry) with parameters compatible with experimental pore sizes, the prediction of the $g(r)$ peaks is not in agreement with experimental results. Even if the hypothesis of a pore-pore potential with spherical symmetry (perhaps with an effective interaction size for the pore that does not coincide with its physical size) can not be excluded, our work suggests that the octagonal shape of the pore and the associated eight-fold symmetry of its interaction potential plays a crucial role in determining the correct spatial distribution of the pores. These facts are worth noticing, since our simplified model, based on the assumption of an effective eight-fold pore-pore interaction, is able to catch a crucial signature of the spatial distributions of nuclear pores, the radial distribution function peaks positions, even if the interaction details (e.g. if the pore-pore potential is attractive or repulsive) are not known. Hopefully, this could help to deepen the investigation of the nature of the pore-pore interplay, allowing to study also *in silico* an interaction that in reality is not fully understood under a biological point of view. Pore-pore interac-

tion, indeed, is probably not direct, but mediated by the lamin scaffold through complex interactions that are hard to model explicitly. Since MD simulations of the lamina filaments forming a three-dimensional network beneath the nuclear envelope have already been performed [89], it would be interesting to try to go further in modelling the outer regions of the cell nucleus, linking the lamina network and the spatial distribution of the nuclear pores. Coming back to our analysis, the spatial distribution of NPCs, investigated through the local order parameters, shows that at high density the pores tend to arrange following the triangular lattice. Even though the $g(r)$ does not show explicit peaks in the correspondence of a triangular lattice, the Ψ_6 quantity (Fig. 5.6 and Fig. 5.7) and the Voronoi tessellation method (Fig. 5.9 and Fig. 5.10) prove that, at high density, islands of six-fold symmetry packed pores appear. Noticeably, such behavior has been already reported in previous experimental observations. During apoptosis, the distribution of nuclear pores on the cell nucleus strongly changes, bringing the NPCs to be highly concentrated in small regions of the nuclear envelope (on mouse cell nuclei) and leaving the rest of the surface pore-free. Those clusters of pores showed an hexagonal packing and were supposed to be correlated with diffuse chromatine areas [32]. Occasional areas of very regular hexagonal packing of nuclear pores have been also observed to emerge during the development of male germ cells, in rodent spermatocytes [33]. Those facts open interesting questions on how the geometrical disposition of the pores in some areas, or even simpler, their density, are influenced by the underlying nuclear activity and on what are the biological causes responsible for the effective interaction among NPCs. Considering the pores under a geometrical and topological point of view, underlying the importance of their octagonal shape, like our simple model does, could be extremely interesting also in the contest of membranes studies. In fact, in a recent paper by Torbati et al. [101], they studied the mechanical stability of the lipid bilayer membrane of the nuclear envelope, considered as two concentric membrane shells fused at numerous sites with toroid-shaped nuclear pores (here simply modeled as circular holes). Using mechanistic arguments based on elasticity, the authors showed that in- and out-of-plane stresses can give rise to the pore geometry and the geometric topology observed in cell nuclei, finding simulated interpore distances in good accord with the ones observed in mammalian cells nuclei. How octagons can contribute to stabilize the curvature of a spherical membrane [49] and how they tend to be spatially arranged on such a geometry, could be an issue to consider in the still unclear process of nuclear pore formation.

Conclusions

In this Thesis, we were driven by the aim of investigating, with the methods of soft matter physics, systems of biological interest. Inspired by the observation of algae, migrating cells and and protein complexes inside the single cell, we implemented simple mathematical models to simulate complex systems of biological interest and to deepen our understanding on their physical properties. The main results of this Thesis, together with open questions and future promising research insights coming from our findings, are summarized below.

The role of self-rotation in active matter systems at the jammed-unjammed transition Usually, theoretical studies of active matter rely mainly on the ability of the active particle to self-propel, driven by active forces. Active self-rotations are rarely studied in this context, although they can be relevant for active matter systems, as we illustrated by analysing the motion of *Chlamydomonas reinhardtii* algae under different experimental conditions. We built a simple model for active particles in 2D based on ABPs (Active Brownian Particles) model, adding an active torque to each particle to simulate the ability of self-rotating. Furthermore, we considered interactions among the active particles: the interaction potential is a sum of terms coming from the Hertzian model, that accounts for friction, and from DMT (Derjaguin-Muller-Toporov) adhesion. We studied this model system of active rotators in different conditions:

- at low packing fractions, where adhesion causes the formation of small rotating clusters;
- at higher densities, where our simulations show a jamming to unjamming transition promoted by active torques. In this regime, we also investigate the role of adhesion that acts in the opposite direction, bringing the system from an unjammed, flowing phase to a jammed, dynamically arrested one;
- in presence of both self-propulsion and self-rotation, studying the interplay between those quantities and deriving a phase diagram.

Our results yield a comprehensive picture of the dynamics of active rotators, highlighting the importance of the internal degrees of freedom of the active particles in determining the collective behaviour of the system. A recent theoretical study revealed how a very general condition of non reciprocal interactions can bring to a spontaneous chiral symmetry breaking, causing the particles composing a many-body system to self-rotate [36]. In this way, the emergence of self-rotation could

occur in a variety of out of equilibrium systems and of biological systems, where non reciprocity is very common. Our work on active rotators could provide useful guidance to interpret experimental results in systems where rotations play a role. As an immediate consequence, it would be interesting to test our model on experimental systems of active rotators easy to tune, such as chiral active fluids made of superparamagnetic particles in active fluids [2], programmable robots [36] [87] or artificial micro-swimmers.

Interacting active matter invading narrow channels We applied our model based on ABPs to the study of interacting active matter invading narrow channels. Our purpose was to investigate the role of single particles properties in determining invasion behaviour. We hypothesized an Hertzian interaction that includes friction among active particles and a specific adhesion term (described via the DMT model). Performing MD simulations and analysing the results, we reported different invasion modes, according to two considered parameters: adhesion strength and particle activity, quantified via the self-propulsion strength. In particular, both by direct inspection of invasion curves and by quantification via the invasion rate, we detected three different invasion behaviours:

- when particles activity is too low to unjam the system and particles are mainly driven by thermal fluctuations or when adhesion is very high and prevents particles to detach from the bulk, the invasion rate is almost zero, so no invasion occurs;
- when the self-propulsion is high and adhesion is low, the active particles rapidly fill the channel with a high invasion rate, behaving like a fluid;
- when particles have enough mobility to detach from the jammed bulk and the adhesion is quite high, groups of particles detach and invasion is dominated by clusters of active particles.

The fact that we could define different invasion modes by controlling just two parameters, the particles self-propulsion and the inter-particle adhesion, could be extremely interesting for comparison with experiments. It has been observed that cells performing epithelial–mesenchymal transition (EMT) can induce a jamming-unjamming phase transition thanks to the reduction of cell–cell adhesion [55]. This experimental observation suggests the key role of adhesion strength in determining the phase behaviour of an active matter system and its validity as a parameter to be considered. Another promising aspect to explore, starting from our results, is the role that channel size has on the invasion dynamics. A recent review on active matter describes how dense active nematic systems, confined in a narrow channel, do not develop active turbulence but more regular flows, such as spontaneous shear flows, unidirectional flows, and vortex lattices, according to channel size [38]. It will be interesting to systematically investigate the role of channel width d in our system, to see if more complex invasion patterns arise.

Spatial distribution of the nuclear pores on the nuclear envelope of eukaryotic cells So far, nuclear pores have been extensively studied to determine their structure and composition, yet their spatial organization and geometric arrangement on the nuclear surface are still poorly understood. We started our work analysing previous experimental data on super-resolution images of the surface of *Xenopus laevis* oocyte

nuclei during development. We characterized the arrangement of nuclear pores using tools commonly employed to study the atomic structural and topological features of soft matter, such as the calculation of the radial distribution function (RDF), local order parameters and Voronoi tessellation. To interpret the experimental results, we hypothesize an effective interaction among nuclear pores and implemented it in extensive numerical simulations of octagonal clusters, mimicking typical pore shapes. We build a pore-pore interaction potential as sum of Lennard-Jones terms, acting among the octagons vertexes and centres, to obtain an eightfold symmetry reminiscent of experimentally observed pore shapes. Thanks to our simple model, we find simulated spatial distributions of nuclear pores that are in good agreement with experiments. This fact suggests that an effective interaction among nuclear pores should exists and could explain their geometrical arrangement on the nuclear envelope surface. More in detail, from the analysis of the radial distribution function g(r) of the nuclear pores, we identify an amorphous, liquid-like structure of nuclear pores in the early phase of oocyte development (when NPC, Nuclear Pore Complex, density is high), where the long-range order is lost soon. Instead, as the oocyte develops, the nuclear pore density decreases and g(r) shows a behaviour compatible with a more dilute, gas-like system. No extended crystalline regions have been found in the spatial distribution of nuclear pores. Furthermore, our simplified model found values for the the location of the first peak of the radial distribution function that are in good agreement with previous experimental measures [67, 33, 93]. This fact is quite relevant since it is known, from the physics of matter, that the positions of the peaks of the radial distribution function and their relative distances give actual information about the geometrical arrangement of the particles within a material, and are a signature of the material itself. Besides those results, our model represents a first attempt to study *in silico* the spatial distribution of nuclear pores and to indirectly investigate the nature of the pore-pore interplay. These results pave the way to further studies needed to determine how the geometrical disposition of the pores in some areas, or even more simply, their density, are influenced by the underlying nuclear activity and to elucidate the biological nature of pore-pore interactions. The biological problem is, in facts, way more complex: pore-pore interaction is probably not direct, but mediated by the lamin scaffold through complex interactions. Furthermore, recent studies connected pores properties and distribution with mechanical properties of the nuclear envelope bilayer membrane in which they are inserted. It has been observed that the NPC scaffold is mechanosensitive and membrane tension regulates its diameter [111]. Besides that, membrane stresses can give rise to pore geometry and geometric topology observed in cell nuclei, finding simulated inter-pore distances in good accord with the ones observed in mammalian cells nuclei [101]. Trying to go further and model the lamina network and its link with the spatial distribution of nuclear pores, and to describe the above mentioned complex scenario, with a model with a reasonable number of parameters, will be a great challenge for further computational studies on NPCs.

Bibliography

[1] Dan Allan, Casper van der Wel, Nathan Keim, Thomas A Caswell, Devin Wieker, Ruben Verweij, Chaz Reid, Thierry, Lars Grueter, Kieran Ramos, apiszcz, zoeith, Rebecca W Perry, François Boulogne, Prashant Sinha, pfigliozzi, Nicolas Bruot, Leonardo Uieda, Jan Katins, Hadrien Mary, and Aron Ahmadia. soft-matter/trackpy: Trackpy v0.4.2, October 2019.

[2] Juan L Aragones, Joshua P Steimel, and Alfredo Alexander-Katz. Aggregation dynamics of active rotating particles in dense passive media. *Soft matter*, 15(19):3929–3937, 2019.

[3] Astropy Collaboration, A. M. Price-Whelan, B. M. Sipőcz, H. M. Günther, P. L. Lim, S. M. Crawford, S. Conseil, D. L. Shupe, M. W. Craig, N. Dencheva, A. Ginsburg, J. T. Vand erPlas, L. D. Bradley, D. Pérez-Suárez, M. de Val-Borro, T. L. Aldcroft, K. L. Cruz, T. P. Robitaille, E. J. Tollerud, C. Ardelean, T. Babej, Y. P. Bach, M. Bachetti, A. V. Bakanov, S. P. Bamford, G. Barentsen, P. Barmby, A. Baumbach, K. L. Berry, F. Biscani, M. Boquien, K. A. Bostroem, L. G. Bouma, G. B. Brammer, E. M. Bray, H. Breytenbach, H. Buddelmeijer, D. J. Burke, G. Calderone, J. L. Cano Rodríguez, M. Cara, J. V. M. Cardoso, S. Cheedella, Y. Copin, L. Corrales, D. Crichton, D. D'Avella, C. Deil, É. Depagne, J. P. Dietrich, A. Donath, M. Droettboom, N. Earl, T. Erben, S. Fabbro, L. A. Ferreira, T. Finethy, R. T. Fox, L. H. Garrison, S. L. J. Gibbons, D. A. Goldstein, R. Gommers, J. P. Greco, P. Greenfield, A. M. Groener, F. Grollier, A. Hagen, P. Hirst, D. Homeier, A. J. Horton, G. Hosseinzadeh, L. Hu, J. S. Hunkeler, Ž. Ivezić, A. Jain, T. Jenness, G. Kanarek, S. Kendrew, N. S. Kern, W. E. Kerzendorf, A. Khvalko, J. King, D. Kirkby, A. M. Kulkarni, A. Kumar, A. Lee, D. Lenz, S. P. Littlefair, Z. Ma, D. M. Macleod, M. Mastropietro, C. McCully, S. Montagnac, B. M. Morris, M. Mueller, S. J. Mumford, D. Muna, N. A. Murphy, S. Nelson, G. H. Nguyen, J. P. Ninan, M. Nöthe, S. Ogaz, S. Oh, J. K. Parejko, N. Parley, S. Pascual, R. Patil, A. A. Patil, A. L. Plunkett, J. X. Prochaska, T. Rastogi, V. Reddy Janga, J. Sabater, P. Sakurikar, M. Seifert, L. E. Sherbert, H. Sherwood-Taylor, A. Y. Shih, J. Sick, M. T. Silbiger, S. Singanamalla, L. P. Singer, P. H. Sladen, K. A. Sooley, S. Sornarajah, O. Streicher, P. Teuben, S. W. Thomas, G. R. Tremblay, J. E. H. Turner, V. Terrón, M. H. van Kerkwijk, A. de la Vega, L. L. Watkins, B. A. Weaver, J. B. Whitmore, J. Woillez, V. Zabalza, and Astropy Contributors. The Astropy Project: Building an Open-science Project and Status of the v2.0 Core Package. *Astron. J.*, 156(3):123, September 2018.

[4] Debarghya Banerjee, Anton Souslov, Alexander G Abanov, and Vincenzo Vitelli. Odd viscosity in chiral active fluids. *Nature communications*, 8(1):1–12, 2017.

[5] Etienne Barthel. Adhesive elastic contacts: Jkr and more. *Journal of Physics D: Applied Physics*, 41(16):163001, 2008.

[6] Clemens Bechinger, Roberto Di Leonardo, Hartmut Löwen, Charles Reichhardt, Giorgio Volpe, and Giovanni Volpe. Active particles in complex and crowded environments. *Reviews of Modern Physics*, 88(4):045006, 2016.

[7] Antoine Bricard, Jean-Baptiste Caussin, Debasish Das, Charles Savoie, Vijayakumar Chikkadi, Kyohei Shitara, Oleksandr Chepizhko, Fernando Peruani, David Saintillan, and Denis Bartolo. Emergent vortices in populations of colloidal rollers. *Nature communications*, 6(1):1–8, 2015.

[8] Nikolai V Brilliantov, Frank Spahn, Jan-Martin Hertzsch, and Thorsten Pöschel. Model for collisions in granular gases. *Physical review E*, 53(5):5382, 1996.

[9] Ralf Brüning, Denis A St-Onge, Steve Patterson, and Walter Kob. Glass transitions in one-, two-, three-, and four-dimensional binary lennard-jones systems. *Journal of Physics: Condensed Matter*, 21(3):035117, 2008.

[10] Abigail Buchwalter, Jeanae M Kaneshiro, and Martin W Hetzer. Coaching from the sidelines: the nuclear periphery in genome regulation. *Nature Reviews Genetics*, 20(1):39–50, 2019.

[11] Ivo Buttinoni, Julian Bialké, Felix Kümmel, Hartmut Löwen, Clemens Bechinger, and Thomas Speck. Dynamical clustering and phase separation in suspensions of self-propelled colloidal particles. *Physical review letters*, 110(23):238301, 2013.

[12] Gaia Camisasca, Harshad Pathak, Kjartan Thor Wikfeldt, and Lars GM Pettersson. Radial distribution functions of water: Models vs experiments. *The Journal of chemical physics*, 151(4):044502, 2019.

[13] ME Cates, JP Wittmer, J-P Bouchaud, and Ph Claudin. Jamming, force chains, and fragile matter. *Physical review letters*, 81(9):1841, 1998.

[14] Andrea Cavagna and Irene Giardina. Bird flocks as condensed matter. *Annu. Rev. Condens. Matter Phys.*, 5(1):183–207, 2014.

[15] David Chandler. Introduction to modern statistical. *Mechanics. Oxford University Press, Oxford, UK*, 40, 1987.

[16] Oleksandr Chepizhko, Costanza Giampietro, Eleonora Mastrapasqua, Mehdi Nourazar, Miriam Ascagni, Michela Sugni, Umberto Fascio, Livio Leggio, Chiara Malinverno, Giorgio Scita, et al. Bursts of activity in collective cell migration. *Proceedings of the National Academy of Sciences*, 113(41):11408–11413, 2016.

[17] Oleksandr Chepizhko, Maria Chiara Lionetti, Chiara Malinverno, Costanza Giampietro, Giorgio Scita, Stefano Zapperi, and Caterina AM La Porta. From jamming to collective cell migration through a boundary induced transition. *Soft matter*, 14(19):3774–3782, 2018.

[18] Sujeet Kumar Choudhary, Aparna Baskaran, and Prerna Sharma. Reentrant efficiency of phototaxis in chlamydomonas reinhardtii cells. *Biophysical journal*, 117(8):1508–1513, 2019.

[19] John C Crocker and David G Grier. Methods of digital video microscopy for colloidal studies. *Journal of colloid and interface science*, 179(1):298–310, 1996.

[20] Leticia F Cugliandolo, Pasquale Digregorio, Giuseppe Gonnella, and Antonio Suma. Phase coexistence in two-dimensional passive and active dumbbell systems. *Physical review letters*, 119(26):268002, 2017.

[21] Baohu Dai, Jizhuang Wang, Ze Xiong, Xiaojun Zhan, Wei Dai, Chien-Cheng Li, Shien-Ping Feng, and Jinyao Tang. Programmable artificial phototactic microswimmer. *Nature nanotechnology*, 11(12):1087–1092, 2016.

[22] Olivier Dauchot and Vincent Démery. Dynamics of a self-propelled particle in a harmonic trap. *Physical review letters*, 122(6):068002, 2019.

[23] Boris V Derjaguin, Vladimir M Muller, and Yu P Toporov. Effect of contact deformations on the adhesion of particles. *Journal of Colloid and interface science*, 53(2):314–326, 1975.

[24] Julien Deseigne, Sébastien Léonard, Olivier Dauchot, and Hugues Chaté. Vibrated polar disks: spontaneous motion, binary collisions, and collective dynamics. *Soft Matter*, 8(20):5629–5639, 2012.

[25] Pasquale Digregorio, Demian Levis, Antonio Suma, Leticia F Cugliandolo, Giuseppe Gonnella, and Ignacio Pagonabarraga. Full phase diagram of active brownian disks: From melting to motility-induced phase separation. *Physical review letters*, 121(9):098003, 2018.

[26] Dirk Drasdo and Stefan Höhme. A single-cell-based model of tumor growth in vitro: monolayers and spheroids. *Physical biology*, 2(3):133, 2005.

[27] James N Dumont. Oogenesis in xenopus laevis (daudin). i. stages of oocyte development in laboratory maintained animals. *Journal of morphology*, 136(2):153–179, 1972.

[28] Matthias Eibauer, Mauro Pellanda, Yagmur Turgay, Anna Dubrovsky, Annik Wild, and Ohad Medalia. Structure and gating of the nuclear pore complex. *Nature communications*, 6(1):1–9, 2015.

[29] Heiko Enderling, Lynn Hlatky, and Philip Hahnfeldt. Migration rules: tumours are conglomerates of self-metastases. *British journal of cancer*, 100(12):1917–1925, 2009.

[30] Elena Ermakova, Jan Solca, Hanspeter Huber, and Dominik Marx. Many-body and quantum effects in the radial distribution function of liquid neon and argon. *Chemical physics letters*, 246(3):204–208, 1995.

[31] Birthe Fahrenkrog and Ueli Aebi. The nuclear pore complex: nucleocytoplasmic transport and beyond. *Nature Reviews Molecular Cell Biology*, 4(10):757–766, 2003.

[32] Elisabetta Falcieri, Pietro Gobbi, Amelia Cataldi, Loris Zamai, Irene Faenza, and Marco Vitale. Nuclear pores in the apoptotic cell. *The Histochemical Journal*, 26(9):754–763, 1994.

[33] Don W Fawcett and Hector E Chemes. Changes in distribution of nuclear pores during differentiation of the male germ cells. *Tissue and Cell*, 11(1):147–162, 1979.

[34] Yaouen Fily and M Cristina Marchetti. Athermal phase separation of self-propelled particles with no alignment. *Physical review letters*, 108(23):235702, 2012.

[35] Aurelie G Floch, Benoit Palancade, and Valerie Doye. Fifty years of nuclear pores and nucleocytoplasmic transport studies: multiple tools revealing complex rules. *Methods in cell biology*, 122:1–40, 2014.

[36] Michel Fruchart, Ryo Hanai, Peter B Littlewood, and Vincenzo Vitelli. Non-reciprocal phase transitions. *Nature*, 592(7854):363–369, 2021.

[37] Ramya Gamini, Wei Han, John E Stone, and Klaus Schulten. Assembly of nsp1 nucleoporins provides insight into nuclear pore complex gating. *PLoS computational biology*, 10(3):e1003488, 2014.

[38] Gerhard Gompper, Roland G Winkler, Thomas Speck, Alexandre Solon, Cesare Nardini, Fernando Peruani, Hartmut Löwen, Ramin Golestanian, U Benjamin Kaupp, Luis Alvarez, et al. The 2020 motile active matter roadmap. *Journal of Physics: Condensed Matter*, 32(19):193001, 2020.

[39] William H Guilford, Laura E Aust, and Karen K Bernd. Whole-cell flagellum-based

motility studied using back focal plane interferometry in a laser trap transducer. In *2006 Fortieth Asilomar Conference on Signals, Systems and Computers*, pages 178–182. IEEE, 2006.

[40] Jean-Pierre Hansen and Ian R McDonald. *Theory of simple liquids*. Elsevier, 1990.

[41] Jean-Pierre Hansen and Ian Ranald McDonald. *Theory of simple liquids: with applications to soft matter*. Academic Press, 2013.

[42] Silke Henkes, Yaouen Fily, and M Cristina Marchetti. Active jamming: Self-propelled soft particles at high density. *Physical Review E*, 84(4):040301, 2011.

[43] Olga Ilina, Pavlo G Gritsenko, Simon Syga, Jürgen Lippoldt, Caterina AM La Porta, Oleksandr Chepizhko, Steffen Grosser, Manon Vullings, Gert-Jan Bakker, Jörn Starruß, et al. Cell–cell adhesion and 3d matrix confinement determine jamming transitions in breast cancer invasion. *Nature cell biology*, 22(9):1103–1115, 2020.

[44] Pritam Kumar Jana, Mikko J Alava, and Stefano Zapperi. Irreversible transition of amorphous and polycrystalline colloidal solids under cyclic deformation. *Physical Review E*, 98(6):062607, 2018.

[45] Hong-Ren Jiang, Natsuhiko Yoshinaga, and Masaki Sano. Active motion of a janus particle by self-thermophoresis in a defocused laser beam. *Physical review letters*, 105(26):268302, 2010.

[46] Sebastian C Kapfer and Werner Krauth. Two-dimensional melting: From liquid-hexatic coexistence to continuous transitions. *Physical review letters*, 114(3):035702, 2015.

[47] Felix Kempf, Andriy Goychuk, and Erwin Frey. Tissue flow through pores: a computational study. *bioRxiv*, 2021.

[48] Felix Kempf, Romain Mueller, Erwin Frey, Julia M Yeomans, and Amin Doostmohammadi. Active matter invasion. *Soft matter*, 15(38):7538–7546, 2019.

[49] Kevin E Knockenhauer and Thomas U Schwartz. The nuclear pore complex as a flexible and dynamic gate. *Cell*, 164(6):1162–1171, 2016.

[50] Gašper Kokot, Shibananda Das, Roland G Winkler, Gerhard Gompper, Igor S Aranson, and Alexey Snezhko. Active turbulence in a gas of self-assembled spinners. *Proceedings of the National Academy of Sciences*, 114(49):12870–12875, 2017.

[51] Aditya Kumar, Jesse K. Placone, and Adam J. Engler. Understanding the extracellular forces that determine cell fate and maintenance. *Development*, 144(23):4261–4270, 12 2017.

[52] Nishant Kumar and Stefan Luding. Memory of jamming–multiscale models for soft and granular matter. *Granular Matter*, 18(3):58, 2016.

[53] Caterina AM La Porta and Stefano Zapperi. *The physics of cancer*. Cambridge University Press, 2017.

[54] Caterina AM La Porta and Stefano Zapperi. *Cell Migrations: Causes and Functions*, volume 1146. Springer, 2019.

[55] Caterina AM La Porta and Stefano Zapperi. Phase transitions in cell migration. *Nature Reviews Physics*, 2(10):516–517, 2020.

[56] Eric Lauga, Willow R DiLuzio, George M Whitesides, and Howard A Stone. Swimming in circles: motion of bacteria near solid boundaries. *Biophysical journal*, 90(2):400–412, 2006.

[57] Herbert Levine, Wouter-Jan Rappel, and Inon Cohen. Self-organization in systems of self-propelled particles. *Physical Review E*, 63(1):017101, 2000.

[58] Demian Levis and Ludovic Berthier. Clustering and heterogeneous dynamics

in a kinetic monte carlo model of self-propelled hard disks. *Physical Review E*, 89(6):062301, 2014.

[59] Liang Li, Simon F Nørrelykke, and Edward C Cox. Persistent cell motion in the absence of external signals: a search strategy for eukaryotic cells. *PLoS one*, 3(5):e2093, 2008.

[60] Roderick YH Lim, Ueli Aebi, and Daniel Stoffler. From the trap to the basket: getting to the bottom of the nuclear pore complex. *Chromosoma*, 115(1):15–26, 2006.

[61] Daniel H Lin and André Hoelz. The structure of the nuclear pore complex (an update). *Annual review of biochemistry*, 88:725–783, 2019.

[62] Andrea J Liu and Sidney R Nagel. Jamming is not just cool any more. *Nature*, 396(6706):21–22, 1998.

[63] Andrea J Liu and Sidney R Nagel. The jamming transition and the marginally jammed solid. *Annu. Rev. Condens. Matter Phys.*, 1(1):347–369, 2010.

[64] Alan R Lowe, Jeffrey H Tang, Jaime Yassif, Michael Graf, William YC Huang, Jay T Groves, Karsten Weis, and Jan T Liphardt. Importin-β modulates the permeability of the nuclear pore complex in a ran-dependent manner. *Elife*, 4:e04052, 2015.

[65] Kazuhiro Maeshima, Kazuhide Yahata, Yoko Sasaki, Reiko Nakatomi, Taro Tachibana, Tsutomu Hashikawa, Fumio Imamoto, and Naoko Imamoto. Cell-cycle-dependent dynamics of nuclear pores: pore-free islands and lamins. *Journal of cell science*, 119(21):4442–4451, 2006.

[66] M Cristina Marchetti, Jean-François Joanny, Sriram Ramaswamy, Tanniemola B Liverpool, Jacques Prost, Madan Rao, and R Aditi Simha. Hydrodynamics of soft active matter. *Reviews of Modern Physics*, 85(3):1143, 2013.

[67] Gerd G Maul, Joseph W Price, and Michael W Lieberman. Formation and distribution of nuclear pore complexes in interphase. *The Journal of cell biology*, 51(2):405–418, 1971.

[68] GG Maul, LL Deaven, JJ Freed, Le M Campbell, and W Becak. Investigation of the determinants of nuclear pore number. *Cytogenetic and Genome Research*, 26(2-4):175–190, 1980.

[69] Lingling Miao and Klaus Schulten. Probing a structural model of the nuclear pore complex channel through molecular dynamics. *Biophysical journal*, 98(8):1658–1667, 2010.

[70] Daniel Needleman and Zvonimir Dogic. Active matter at the interface between materials science and cell biology. *Nature reviews materials*, 2(9):1–14, 2017.

[71] Corey S O'Hern, Stephen A Langer, Andrea J Liu, and Sidney R Nagel. Random packings of frictionless particles. *Physical Review Letters*, 88(7):075507, 2002.

[72] Alessandro Ori, Niccolò Banterle, Murat Iskar, Amparo Andrés-Pons, Claudia Escher, Huy Khanh Bui, Lenore Sparks, Victor Solis-Mezarino, Oliver Rinner, Peer Bork, et al. Cell type-specific nuclear pores: a case in point for context-dependent stoichiometry of molecular machines. *Molecular systems biology*, 9(1):648, 2013.

[73] Linda Oswald, Steffen Grosser, David M Smith, and Josef A Käs. Jamming transitions in cancer. *Journal of physics D: Applied physics*, 50(48):483001, 2017.

[74] Corey S O'hern, Leonardo E Silbert, Andrea J Liu, and Sidney R Nagel. Jamming at zero temperature and zero applied stress: The epitome of disorder. *Physical Review E*, 68(1):011306, 2003.

[75] N Panté. Contribution of electron microscopy to the study of the nuclear pore complex structure, composition, and function. *Modern Research and Educational Topics in Microscopy*, pages 144–153, 2007.

[76] Jin-Ah Park, Jae Hun Kim, Dapeng Bi, Jennifer A Mitchel, Nader Taheri Qazvini, Kelan Tantisira, Chan Young Park, Maureen McGill, Sae-Hoon Kim, Bomi Gweon, et al. Unjamming and cell shape in the asthmatic airway epithelium. *Nature materials*, 14(10):1040–1048, 2015.

[77] Juan R Perilla, Boon Chong Goh, C Keith Cassidy, Bo Liu, Rafael C Bernardi, Till Rudack, Hang Yu, Zhe Wu, and Klaus Schulten. Molecular dynamics simulations of large macromolecular complexes. *Current opinion in structural biology*, 31:64–74, 2015.

[78] Steve Plimpton. Fast parallel algorithms for short-range molecular dynamics. *Journal of computational physics*, 117(1):1–19, 1995.

[79] Vyas Ramasubramani, Bradley D. Dice, Eric S. Harper, Matthew P. Spellings, Joshua A. Anderson, and Sharon C. Glotzer. freud: A software suite for high throughput analysis of particle simulation data. *Computer Physics Communications*, 254:107275, 2020.

[80] Sriram Ramaswamy. The mechanics and statistics of active matter. *Annu. Rev. Condens. Matter Phys.*, 1(1):323–345, 2010.

[81] Linda Ravazzano, Silvia Bonfanti, Roberto Guerra, Fabien Montel, Caterina A. M. La Porta, and Stefano Zapperi. Spatial organization of nuclear pores in xenopus laevis oocytes. *bioRxiv*, 2021.

[82] Linda Ravazzano, Silvia Bonfanti, Maria Chiara Lionetti, Maria Rita Fumagalli, Roberto Guerra, Oleksandr Chepizhko, Caterina AM La Porta, and Stefano Zapperi. Unjamming of active rotators. *Soft Matter*, 16(23):5478–5486, 2020.

[83] R Reichelt, A Holzenburg, EL Buhle, M Jarnik, A Engel, and U Aebi. Correlation between structure and mass distribution of the nuclear pore complex and of distinct pore complex components. *Journal of Cell Biology*, 110(4):883–894, 1990.

[84] Katharina Ribbeck and Dirk Görlich. Kinetic analysis of translocation through nuclear pore complexes. *The EMBO journal*, 20(6):1320–1330, 2001.

[85] Hans Ris. High-resolution field-emission scanning electron microscopy of nuclear pore complex. *Scanning*, 19(5):368–375, 1997.

[86] Marzia Rovere, Dieter W Heermann, and Kurt Binder. The gas-liquid transition of the two-dimensional lennard-jones fluid. *Journal of Physics: Condensed Matter*, 2(33):7009, 1990.

[87] AD Rozenblit, VA Porvatov, DA Petrova, IS Khakhalin, KP Kotlyar, G Yu Gritsenko, AA Evreiskaya, MF Lebedeva, EI Kretov, DS Filonov, et al. Diffusive dynamics and jamming in ensembles of robots with variable friction. In *Journal of Physics: Conference Series*, volume 1695, page 012201. IOP Publishing, 2020.

[88] Monirosadat Sadati, Nader Taheri Qazvini, Ramaswamy Krishnan, Chan Young Park, and Jeffrey J Fredberg. Collective migration and cell jamming. *Differentiation*, 86(3):121–125, 2013.

[89] K Tanuj Sapra, Zhao Qin, Anna Dubrovsky-Gaupp, Ueli Aebi, Daniel J Müller, Markus J Buehler, and Ohad Medalia. Nonlinear mechanics of lamin filaments and the meshwork topology build an emergent nuclear lamina. *Nature communications*, 11(1):1–14, 2020.

[90] Debarati Sarkar, Gerhard Gompper, and Jens Elgeti. A minimal model for structure, dynamics, and tension of monolayered cell colonies. *Communications Physics*, 4(1):1–8, 2021.

[91] Andrea Schlune, Victor Shahin, Karoline Enss, Herman Schillers, and Hans Oberleithner. Plugs in nuclear pores: Transcripts in early oocyte development identified

with nanotechniques. *Journal of cellular biochemistry*, 98(3):567–576, 2006.

[92] Felix J Segerer, Florian Thüroff, Alicia Piera Alberola, Erwin Frey, and Joachim O Rädler. Emergence and persistence of collective cell migration on small circular micropatterns. *Physical Review Letters*, 114(22):228102, 2015.

[93] Julien Sellés, May Penrad-Mobayed, Cyndélia Guillaume, Alica Fuger, Loïc Auvray, Orestis Faklaris, and Fabien Montel. Nuclear pore complex plasticity during developmental process as revealed by super-resolution microscopy. *Scientific reports*, 7(1):1–8, 2017.

[94] Leonardo E Silbert, Deniz Ertaş, Gary S Grest, Thomas C Halsey, Dov Levine, and Steven J Plimpton. Granular flow down an inclined plane: Bagnold scaling and rheology. *Physical Review E*, 64(5):051302, 2001.

[95] Lawrie B Skinner, CJ Benmore, Joerg C Neuefeind, and John B Parise. The structure of water around the compressibility minimum. *The Journal of chemical physics*, 141(21):214507, 2014.

[96] Joakim Stenhammar, Davide Marenduzzo, Rosalind J Allen, and Michael E Cates. Phase behaviour of active brownian particles: the role of dimensionality. *Soft matter*, 10(10):1489–1499, 2014.

[97] Alexander Stukowski. Visualization and analysis of atomistic simulation data with OVITO-the Open Visualization Tool. *MODELLING AND SIMULATION IN MATERIALS SCIENCE AND ENGINEERING*, 18(1), JAN 2010.

[98] Kandice Tanner, Hidetoshi Mori, Rana Mroue, Alexandre Bruni-Cardoso, and Mina J Bissell. Coherent angular motion in the establishment of multicellular architecture of glandular tissues. *Proceedings of the National Academy of Sciences*, 109(6):1973–1978, 2012.

[99] William Thielicke and Eize Stamhuis. Pivlab–towards user-friendly, affordable and accurate digital particle image velocimetry in matlab. *Journal of open research software*, 2(1), 2014.

[100] A. P. Thompson, H. M. Aktulga, R. Berger, D. S. Bolintineanu, W. M. Brown, P. S. Crozier, P. J. in 't Veld, A. Kohlmeyer, S. G. Moore, T. D. Nguyen, R. Shan, M. J. Stevens, J. Tranchida, C. Trott, and S. J. Plimpton. LAMMPS - a flexible simulation tool for particle-based materials modeling at the atomic, meso, and continuum scales. *Comp. Phys. Comm.*, 271:108171, 2022.

[101] Mehdi Torbati, Tanmay P Lele, and Ashutosh Agrawal. Ultradonut topology of the nuclear envelope. *Proceedings of the National Academy of Sciences*, 113(40):11094–11099, 2016.

[102] PN Unwin and RA Milligan. A large particle associated with the perimeter of the nuclear pore complex. *The Journal of cell biology*, 93(1):63–75, 1982.

[103] Sri Ram Krishna Vedula, Man Chun Leong, Tan Lei Lai, Pascal Hersen, Alexandre J Kabla, Chwee Teck Lim, and Benoît Ladoux. Emerging modes of collective cell migration induced by geometrical constraints. *Proceedings of the National Academy of Sciences*, 109(32):12974–12979, 2012.

[104] Tamás Vicsek, András Czirók, Eshel Ben-Jacob, Inon Cohen, and Ofer Shochet. Novel type of phase transition in a system of self-driven particles. *Physical review letters*, 75(6):1226, 1995.

[105] Xiaolu Wang, Martin In, Christophe Blanc, Alois Würger, Maurizio Nobili, and Antonio Stocco. Janus colloids actively rotating on the surface of water. *Langmuir*, 33(48):13766–13773, 2017.

[106] DM Woolley. Motility of spermatozoa at surfaces. *REPRODUCTION-*

CAMBRIDGE-, 126(2):259–270, 2003.

[107] Marcel Workamp, Gustavo Ramirez, Karen E Daniels, and Joshua A Dijksman. Symmetry-reversals in chiral active matter. *Soft Matter*, 14(27):5572–5580, 2018.

[108] Adam Wysocki and Heiko Rieger. Capillary action in scalar active matter. *Physical review letters*, 124(4):048001, 2020.

[109] JL Yarnell, MJ Katz, Ro Go Wenzel, and SH Koenig. Structure factor and radial distribution function for liquid argon at 85 k. *Physical Review A*, 7(6):2130, 1973.

[110] Maria Zeitz, Katrin Wolff, and Holger Stark. Active brownian particles moving in a random lorentz gas. *The European Physical Journal E*, 40(2):1–10, 2017.

[111] Christian E Zimmerli, Matteo Allegretti, Vasileios Rantos, Sara K Goetz, Agnieszka Obarska-Kosinska, Ievgeniia Zagoriy, Aliaksandr Halavatyi, Gerhard Hummer, Julia Mahamid, Jan Kosinski, et al. Nuclear pores dilate and constrict in cellulo. *Science*, 374(6573):eabd9776, 2021.

[112] Andreas Zöttl and Holger Stark. Emergent behavior in active colloids. *Journal of Physics: Condensed Matter*, 28(25):253001, 2016.

List of Publications

Refereed publications

Schakenraad, K., Ravazzano, L., Sarkar, N., Wondergem, J. A., Merks, R. M., & Giomi, L. (2020). Topotaxis of active Brownian particles. Physical Review E, 101(3), 032602.

Ravazzano, L., Bonfanti, S., Lionetti, M. C., Fumagalli, M. R., Guerra, R., Chepizhko, O., La Porta, C. A. M., & Zapperi, S. (2020). Unjamming of active rotators. Soft Matter, 16(23), 5478-5486.

Publications under review

Ravazzano, L., Bonfanti, S., Guerra, R., Montel, F., La Porta, C. A. M., & Zapperi, S. (2021). Spatial organization of nuclear pores in Xenopus laevis oocytes. bioRxiv 2021.09.01.458492; doi: `https://doi.org/10.1101/2021.09.01.458492`

Publications in preparation

Ravazzano, L., Guerra, R., Bonfanti, S., & Zapperi, S. Active matter invasion in narrow channels.